A High-Performance Three-Phase Grid-Connected PV System Based On Multilevel Current Source Inverter

by

Prajna Paramita Dash

A thesis
presented to the University of Waterloo
in fulfillment of the
thesis requirement for the degree of
Doctor of Philosophy
in
Electrical and Computer Engineering

Waterloo, Ontario, Canada, 2013

I hereby declare that I am the sole author of this thesis. This is a true copy of the thesis, including any required final revisions, as accepted by my examiners.

I understand that my thesis may be made electronically available to the public.

Abstract

Current Source Inverter (CSI) topology is gaining acceptance as a competitive alternative for grid interface of renewable energy systems due to its unique and advantageous features. Merits of CSI over the more popular Voltage Source Inverter (VSI) topology have been elaborated on by a number of researchers. However, there is a dearth of quality work in modeling and control of CSI topology interfacing renewable energy resources to the grid. To enrich the study focussing on application of CSI for renewable energy interface, this thesis develops a multilevel structure based on CSI for three-phase grid-connected Photovoltaic (PV) application. In the first part of research, a single-stage CSI interfacing to PV array is developed. The CSI-based PV system is equipped with Maximum Power Point Tracker (MPPT), DC-link current controller, and AC-side current controller. To eliminate the nonlinearity introduced by the PV array, a feed-forward control is introduced in the DC-link current controller. The AC-side current controller is responsible for maintaining unity power factor at the Point of Common Coupling (PCC). To verify the performance of the developed CSI-based PV system, a number of simulation studies are carried out in PSCAD/EMTDC environment. To illustrate the performance of the CSI-based PV system during transients on the grid side, simulation studies are carried out for four kinds of faults. Results obtained from fault studies are highly in favor of CSI topology and provide illustrative evidence for short-circuit current protection capability of the CSI. On the other hand, the VSI-based PV system performs poorly when subjected to similar grid transients.

To extend the research on CSI-based PV system further, a multilevel structure based on CSI is developed. The multilevel structure is a parallel combination of n CSI units and capable of producing $2n+1$ levels of current at the terminal of the inverter. Each unit in the multilevel structure has its own MPPT, DC-link current controller. However, on the AC-side a combined current controller is proposed. The design results in a high power rating

with reduced number of filters, sensors and controllers. The developed multilevel structure can operate with PV arrays exposed to equal and unequal insolation level. However, when the PV arrays are operating under unequal insolation level, low order harmonics are generated in the sinusoidal current that is injected into the grid. Elimination of these harmonics is performed by implementing a modified control strategy in stationary reference frame that corresponds to the harmonic component that needs to be minimized. The modified control strategy operates in coordination with the existing DC-side and AC-side current controllers, and MPPTs. Therefore, real-time suppression of current harmonics can be ensured. Performance of the multilevel structure is verified by different transient studies.

Acknowledgements

This thesis would not have been possible without the guidance and the help of several individuals who in one way or another contributed and extended their valuable assistance in the preparation and completion of this work.

First and foremost, my utmost gratitude to Dr. Mehrdad Kazerani, my supervisor whose sincerity and encouragement I will never forget. This work would not have been possible without his support and valuable suggestions.

I sincerely wish to thank my committee members, Professors Claudio A. Canizares, Daniel E. Davison, and Amir Khajepour for their valuable feedbacks during my comprehensive examination. I am thankful to them for taking time to read carefully my thesis. I would like to thank Professor Bin Wu for agreeing to serve as my external examiner.

I am forever grateful to my husband, Dr. Akshaya Mishra, for all his love, support, and patience. Without his support and encouragement this work would not have been accomplished.

Last but not the least, my family and the one above all of us, the omnipresent God, for answering my prayers, for giving me the strength when I need them.

Dedication

To my Son,

Priyansh,

the sunshine of our life

Contents

List of Tables

List of Figures

List of Abbreviations

CSI	Current Source Inverter
VSI	Voltage Source Inverter
DG	Distributed Generation
PV	Photovoltaic
PCC	Point of Common Coupling
DC	Direct Current
AC	Alternate Current
SLG	Single-Line-to-Ground
DLG	Double-Line-to-Ground
TPG	Three-Phase-to-Ground
LL	Line-to-Line
PLL	Phase-Locked-Loop
MPPT	Maximum Power Point Tracker
NDZ	Non-Detection-Zone

Nomenclature

v_s	AC-side terminal voltage
v	Voltage at the PCC, voltage at the secondary side of transformer, T_r
v_g	Substation bus (Grid) voltage
v_{dc}	DC-side voltage of the CSI
v_{pv}	Voltage of the PV array
i_{pv}	PV array current
i_{dc}	DC-link current of the CSI
i_t	CSI AC-side terminal current
i_s	Current sent to the grid
P_{pv}	PV array power
P_s	Real power exchanged at the PCC
Q_s	Reactive power exchanged at the PCC
N	Interface transformer turns ratio
C_f	filter capacitor
R_g	Grid resistance
L_g	Grid inductance
ω	dq-frame angular speed
ω_0	Nominal frequency of grid (e.g. 377 rad/s)

ρ	dq-frame reference angle
S	Insolation level
$Re\{\}$	Real part of
$Im\{\}$	Imaginary part of
d	Subscript denoting d-axis component
q	Subscript denoting q-axis component
$\vec{}$	Superscript denoting space-phasor quantity
"T"	Superscript denoting matrix transposition
$\mathbf{s}$	Complex frequency, $\sigma + j\omega$

Chapter 1

Introduction

1.1 Motivation

Demand for clean, economical, and renewable energy has increased consistently over the past few decades. Among a variety of renewable energy resources available, solar energy appears to be a major contender due to its abundance and pollution-free conversion to electricity through photovoltaic (PV) process. Increasing interest in PV systems, demands growth in research and development activities in various aspects such as Maximum Power Point Tracking (MPPT), PV arrays, anti-islanding protection, stability and reliability, power quality and power electronic interface. With increase in penetration level of PV systems in the existing power systems, these issues are expected to become more critical in time since they can have noticeable impact on the overall system performance. More efficient and cost-effective PV modules are being developed and manufactured, in response to the concerns raised by the PV system developers, utilities and customers. Numerous standards have been designed to address power quality and grid-integration issues. Extensive research in the field of MPPT has resulted in fast and optimized method to track the maximum power point. Regarding power electronic converter to interface PV arrays

to the grid, Voltage Source Inverter (VSI) is a widely used topology to date. However, this topology has some limitation when it comes to PV application. The VSI topology has buck (step-down) characteristics; therefore to step-up the low voltage output from the PV array, an extra power electronic interface may be required. Moreover, the VSI-based PV system demonstrates a poor performance during transients such as faults on the grid-side. These drawbacks of VSI can be overcome by a current-base inverter known as Current Source Inverter (CSI). CSI is a preferred topology in high power motor drives. CSI has inherent boosting (stepping-up) capability, namely it can operate with a low-voltage DC source on the DC side. Moreover, presence of an inductor on the DC-side of the CSI ensures a low-ripple current at the interfaces of both PV panels and the inverter. Furthermore, DC-side current regulation offers an inherent current limiting and overcurrent protection feature during AC-side faults. Despite CSI's many favorable features for PV application, its wide-spread use has been hindered due to the following drawbacks:

1. The on-state losses in the switching elements, where the semiconductor switches used are not capable of withstanding negative voltage and thus have to be connected in series with a diode, are higher than those in voltage-source inverter.

2. The AC-side filter capacitors can resonate with the distribution line inductance.

3. The losses in the DC inductor of CSI are known to be higher than those in the DC capacitor of the VSI.

   With new advances in the power semiconductor technology, switching losses have been reduced to great extent. If the AC-side filter capacitor is designed properly, resonance can be avoided. The DC-side inductor is still a troublemaker. However, with recent developments in Superconducting Magnetic Energy Storage (SMES) technology, there is hope that concerns regarding inductor can be removed in the future, allowing CSI to prove itself a fierce competitor to VSI. Turning this possibility into

reality, extensive research in the field of CSI applications for PV systems is necessary. Though researchers have studied CSI for PV application before, there is a lot of room for quality research and investigation in CSI's control structure and transient performance when it is interfaced to a PV array and grid. Motivated by the huge demand for solar energy and immediate need for improvements in PV systems, the research reported in this thesis intends to add to the existing knowledge on PV system applications of CSI and make quality contributions to the field.

1.2 Objectives

The goal of the research work is to design an efficient three-phase grid-connected, single-stage CSI-based PV system. To achieve this, the control system is designed by deriving a detailed mathematical model of the system including PV arrays, a CSI, and a distribution system. Performance of control structure is verified by simulating the complete system in the PSCAD/EMTDC environment. The main objectives of the research can be summarized as follows:

- To develop a single-stage power electronic interface based on CSI for three-phase grid-connected PV application, capable of extracting maximum power from the PV arrays at all insolation levels. Moreover, the developed system should be capable of injecting a clean sinusoidal current into the power grid in phase with the voltage at the Point of Common Coupling (PCC).
- To study the viability of the developed system in different transient conditions. For this study, different kinds of faults are considered on the grid side.
- To perform a comparative study of two PV systems, one based on VSI and the other based on CSI under different transient conditions.

- To develop a multilevel CSI-based PV system, capable of operating under equal and unequal irradiation levels, at switching frequencies lower than those for the single-unit CSI-based PV system and capable of injecting clean sinusoidal currents into the grid at all conditions.
- To study the islanding behavior of multilevel structure when PV array are operating under equal and unequal solar irradiation conditions.
- To develop a linearized model of the CSI-based PV system and analyze the impact of variation of different parameters on the behaviors of different state variables.

1.3 Thesis Organization

To achieve the aforementioned objectives and facilitate the presentation of results derived in the course of this research, the thesis is organized as follows:

1. Chapter 2 provides a literature survey on grid-connected PV systems. In the first part of the chapter, the general structure of a grid-connected PV system is discussed. This is followed by a discussion on different standards developed for safe operation of PV systems used as Distributed Generations (DGs). Survey on different topologies for PV application constitutes a vital part of this chapter. In the later part of the chapter, a survey on multilevel topologies is presented.
2. Based on the literature survey presented in Chapter 2, Chapter 3 attempts to address the gap in the research on CSI-based grid-connected PV systems. To accomplish this, a detailed mathematical modeling of PV arrays interfaced to the grid through a CSI is presented. Controller design is discussed in detail. Evaluation of the controller is performed under different transient conditions towards the end of Chapter 3.

3. Chapter 4 develops a multilevel structure based on CSI. The multilevel structure is capable of accommodating PV arrays exposed to equal and unequal insolation levels. However, operation of PV arrays in unequal insolation levels leads to generation of low-order harmonics on the AC side. To minimize these low-order harmonics, a modified control strategy is presented and discussed in Chapter 4.

4. Chapter 5 discusses islanding behavior of multilevel structure that was developed in Chapter 4. A mathematical analysis is presented to establish a relationship between variation of voltage at the Point of Common Coupling (PCC) and power level of the multilevel structure. Through analysis, it is demonstrated that when units of multilevel structure are operating at unequal power levels, voltage variation is higher than in the case where all units are operating at equal power levels; this, in turn, triggers islanding detection logic faster. To support this analysis simulation results are presented at the end of Chapter 5.

5. Chapter 6 presents a linearized model of the system presented in Chapter 3. The linearization is performed by considering small perturbation around a steady-state operating point. Sensitivity study is performed for different state variables in response to variations in different parameters.

6. Summary, Conclusion and Contributions of this research to the field of power electronic grid interface for PV arrays are included in Chapter 7.

Chapter 2

Three-phase Grid-Connected Photovoltaic (PV) System

2.1 Introduction

In recent years, there has been an appreciable interest in the utilization of Photovoltaic (PV) systems due to concerns about environmental issues associated with use of fossil fuels, rising fuel cost and energy security. Despite this high interest, not a significant number of grid-connected PV systems are visible at present as compared to traditional energy sources such as oil, gas, coal, nuclear, hydro, and wind [1]. So far, PV systems of single- or double- digit megawatt (MW) capacities have been connected to the grid mainly at sub-transmission voltage levels. At the distribution level, the PV systems mainly consist of roof-top installations with capacities of few kilowatts which are unlikely to have any significant impact on the existing power system. With the growing interest in solar energy and national policies designed in favor of green energy, it is expected that there will be significant increase in large-size PV plants, which can have significant impact on the existing power grid. For successful operation of large-scale grid-connected PV systems, a robust

and cost-effective PV inverter solution is required. Extensive research in the field of power conditioning unit has spawned a range of design solutions for the PV inverter. So far, voltage source inverter (VSI) has been widely employed for interfacing with PV modules with the grid. Though VSI comes with many advantageous features, the topology has some major drawbacks which add extra cost and complexity in the structure of a PV system. To make the proliferation of grid-connected PV systems a successful business option, the cost, performance, and life expectancy of the power electronic interface need to be improved. To meet these expectations, the researcher chose a topology which is a current-based, has better transient performance, longer lifetime compared to the voltage-based inverter, and can work efficiently in a single-stage structure.

The literature review presented in this chapter starts with the structure of a 3-phase grid-connected PV system to give readers an idea about the functionality of a typical PV inverter. Since the PV inverter is interfaced to a utility grid, it is very important that the interconnection is in accordance with the utility codes and standards. Therefore, section 2.3 presents a discussion on the existing standards. This is followed by a survey of inverter topologies for interfacing PV modules to the grid. The survey on inverter topology is presented to show differences between the PV inverter topologies that were used in the past, are used today and are proposed for future applications. This is followed by a survey of the research conducted on CSI for grid-connected PV applications and a survey on multilevel topologies in PV application. Finally, a summary of the grid-connected PV inverters conclude the chapter.

2.2 Structure of a Typical Photovoltaic (PV) System

The main building blocks of a PV system, shown in Figure 2.1 are described below.

2.2.1 PV array

A PV array consists of a number of PV modules or panels. A PV module is an assembly of a large number of interconnected PV cells [2].

2.2.2 Inverter

The inverter in a PV system is employed to transform the DC-voltage generated from a PV module to a three-phase AC voltage. A three-phase inverter has three legs with two switches in each leg. The switching is performed by carrier-based or space-vector- based Pulse-Width Modulation (PWM) [3]. A detailed discussion on different inverter topologies is provided later in this chapter. The inverter is usually interfaced to the utility grid through a transformer. However, transformer-less PV inverter topologies have also been proposed and implemented for single-phase grid-connected PV inverter.

2.2.3 Filter

The output quantity of an inverter (voltage in VSI and current in CSI) is pulsed and contains switching harmonics along with a 60 Hz fundamental. In order to separate the 60

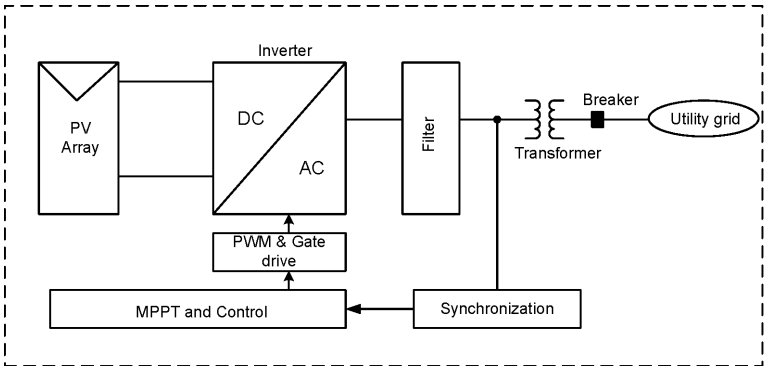

Figure 2.1 Structure of a typical single-stage PV system.

Hz component, a filter is essential at the AC terminal of the inverter, where it is interfaced to the grid. Since the performance of the filter depends on the grid impedance, special care must be practiced in the filter design [4].

2.3 Specification and Standards

The inverters interfacing the PV array to the grid perform two major tasks: (i) to ensure that the PV array is operated at its maximum power point and (ii) to inject sinusoidal current to the grid at the desired power factor. Since the inverter is connected to the grid, the standards set by the utility companies must be obeyed. The standards set by the utility companies deal with issues such as power quality and detection of islanding operation. A summary of these standards are listed in [5, 6, 7, 8, 9]. From the protection point of view, the inverters must be able to detect an islanding situation when voltage and frequency are beyond threshold limit set by the standards and take appropriate measures in order to protect equipment and personnel [10]. Islanding is a situation where a Distributed Generator (DG) continues to supply power to the load though the connection from the grid is lost. This situation is not allowed from safety point of view. In present practice, two islanding detection methods are widely used, namely passive methods and active methods. Passive methods monitor deviation in grid parameters when the grid connection is lost. Hence, they do not have any influence on the power quality. On the other hand, active methods introduce a disturbance to the grid and monitor the effect. Therefore, they may have some impact on power quality. Preventing the DG from going to islanding mode is an active research area. Extensive research in this field has generated many islanding detection methods [11, 12, 13, 14, 15, 16]. However, there is not a single one that is accepted from the viewpoints of performance, cost, and speed of response. There is also limitation on the allowable amount of DC current injected into the grid [5]. The purpose of limiting the DC-current injection into the grid is to avoid saturation of the distribution transformer which

acts as a connecting medium between the PV system and the utility grid [7]. However, the restriction put on the DC current is very mild, i.e., 0.5% to 1 % of the rated output current. In order to mitigate this effect, some inverters employ a transformer-less configuration. The inverters interfacing the PV modules to grid must guarantee that the PV array is operating at its Maximum Power Point (MPP). This is achieved by implementing a Maximum Power Point Tracker (MPPT). A fair number of MPPT techniques have been introduced and investigated in the past. Reference [17] discusses 19 different methods of MPPT introduced since 1968. The most widely used MPPT technique is Perturb & Observe (P&O) method, even though it has some shortcomings in performance.

2.4 Past, Present, and Future of PV Technology

A detailed survey on the evolution of PV system configuration has been given in [8]. In this section a summary of the literature available is presented.

2.4.1 Past Technology: Centralized Structure

The past technology, shown in Figure 2.2(a), was based on a centralized concept. One inverter interfaced a large number of PV modules to the grid. Main features of this structure are described below.

- The PV modules were arranged in the form of a number of strings. Each string had sufficient voltage to avoid further amplification.
- The strings were then connected in parallel through string diodes to realize high power levels.
- The grid connection was usually performed by line commutated thyristors which led to current harmonics and thus poor power quality.

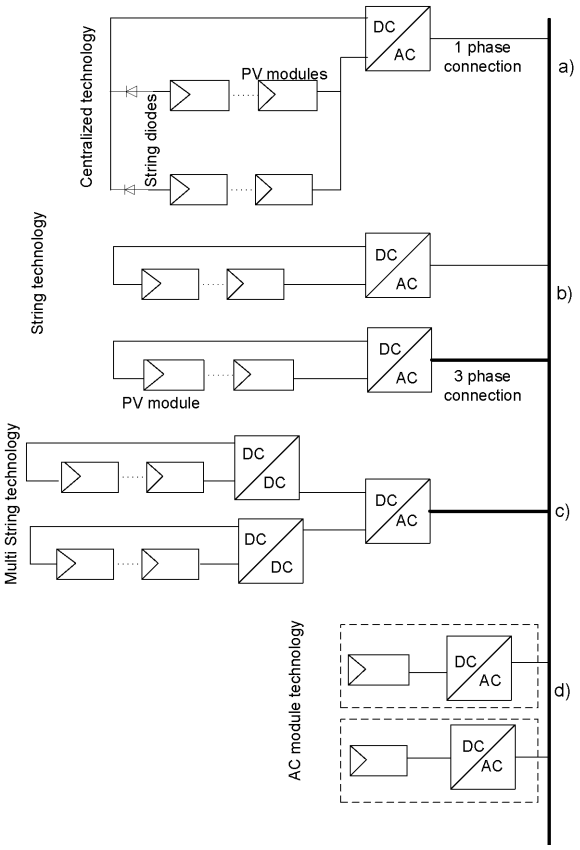

Figure 2.2 Classification of PV power conversion topology (a) Past centralized technology, (b) Present string technology, (c) Present and future multi-string technology. (d) Present and future AC module technology.

The main shortcoming of the centralized inverter was the high DC voltage resulting from series connection of PV modules requiring a high voltage DC cable between the PV module and the inverter. In addition, there were power losses due to partial shading and disability of centralized MPPT to deal with this situation, losses due to mismatch between the PV modules and losses in the string diodes. High harmonic content and low power quality resulted from the centralized inverter which were based on line commutated thyristors.

2.4.2 Present Technology: Single-String Structure and AC modules

To overcome the power mismatch and inefficient MPPT technology, the present inverter technology has been introduced, which is based on processing the power produced by individual strings (single-string technology) or individual modules (AC module). The present technology offers improved performance compared to the past technology in the following ways:

- Distributed MPP tracking leads to increase in the overall efficiency compared to the centralized inverter. Moreover, the cost of manufacturing and thus the sale price is reduced due to mass production.
- It provides the possibility of up-scaling the system due to the modular structure.
- It is more user friendly because of its straight forward structure with "Plug-and-Play" feature.
- It is based on forced-commutated DC-AC converters employing IGBTS, resulting in low harmonic content and thus high power quality.

2.4.3 Future Technology: Multi-String Structure, AC Modules and AC Cells

The future technology is a combination of the past and present technologies. Several strings are interfaced with their own DC-DC converter through a common DC-AC converter (multi-string) or through their own DC-AC converter (AC module) [18]. This certainly offers an advantage over the past technology, since each string can be controlled individually and independently of one another. Compared to the present technology, the future technology provides flexibility of introducing new technologies into the existing systems.

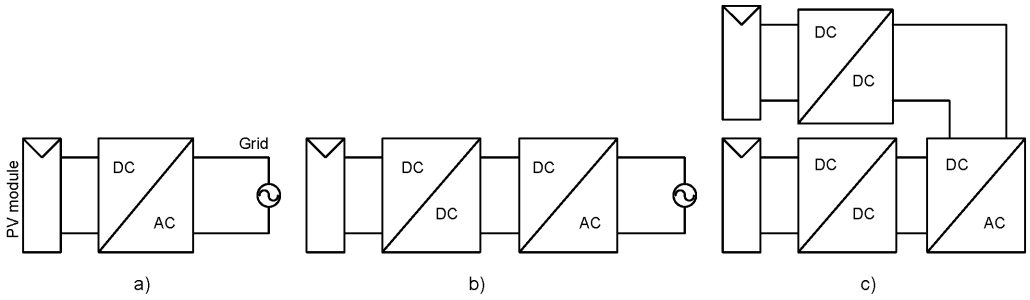

Figure 2.3 Classification of PV inverter topology. (a) Single power processing stage, (b)Dual power processing stage, (c) Dual power processing stage with a common DC-AC inverter.

2.5 Classification of Inverter Topologies

Inverter topology is classified on the basis of number of power processing stages, whether or not they employ a transformer, and type of grid interface.

2.5.1 Classification of Power Conversion Topologies

Figure 2.3(a)) shows a single-stage topology. The inverter handles all tasks by itself (i.e., MPPT, grid current control and voltage amplification in some cases). The inverter employed in single-stage conversion must be designed to handle a peak power of twice the nominal power [8].

A dual-stage topology is illustrated in Figure 2.3(b). In this topology, the tasks are divided between the DC-DC converter and DC-AC converter. Maximum power point tracking is performed by the DC-DC converter and current control task is performed by the DC-AC converter.

Finally, Figure 2.3(c) is the solution for multi-string technology. The DC-DC converters

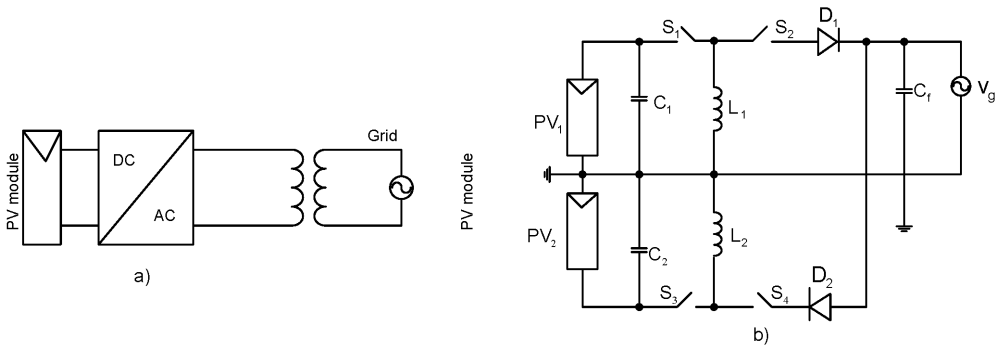

Figure 2.4 Evolution of PV inverters. (a) Transformer included inverter, (b)Transformer-less inverter.

take care of MPPT and are connected to the DC-link of a common DC-AC inverter which takes care of the grid interfacing.

2.5.2 Transformer and Transformer-less configurations

Generally, grid-interfaced inverters use a line-frequency transformer for voltage amplification when the input voltage is low as shown in Figure 2.4(a). In addition, the transformer provides galvanic isolation and grounding of the PV module. Furthermore, double grounding for single-phase PV inverter topology can be easily realized by interfacing a transformer. However, transformer is considered as an "extra" component when the input voltage is sufficiently high. Therefore, transformer-less inverters have been introduced recently to avoid increased size, weight, and price due to addition of the transformer. Researchers have proposed transformer-less configuration for single-phase PV inverter with double grounding feature by splitting PV modules into two halves or by modifying the inverter topology [19]. For single-phase transformer-less PV inverter, double grounding feature is easily realized by splitting the PV modules into two parts. A schematic diagram of such PV inverter is presented in 2.4(b). Reference [19] proposes a single-stage single-phase transformer-less

grid-connected topology which is capable of double grounding feature. The topology proposed in [19] uses only one PV source instead of splitting the PV module into two parts, a single buck-boost converter, and a decoupling capacitor. The argument the authors have made for not splitting the PV source is that there will be a high total harmonic Distortion (THD) if there is a mismatch of power between the two parts. Moreover, there is less utilization of PV source when it is divided.

2.5.3 Types of Power Conditioning Unit

So far, the discussion was about the overall structure, configuration, and power processing stages for the PV inverter. This part studies the structure and topology of the power conditioning unit employed in the grid-connected PV systems. Power electronic inverter, sometimes known as power conditioning unit, connects the utility grid with the PV source. Moreover, selection of a proper power electronic interface topology can contribute towards reducing the number of stages, which in turn, reduces the cost of the whole unit. Since 1984, researchers have proposed a range of topologies for the power conditioning system. References [20] and [21] provide a survey on the structure of power electronic interface used in three-phase grid-connected PV systems. The topology that has been thoroughly investigated and adopted for grid-connected PV inverter is Voltage Source Inverter (VSI). This topology enjoys a simple and effective control scheme and well-established Pulse Width Modulation switching techniques [21]. A schematic diagram of VSI topology connected to 3-phase grid is presented in Figure 2.5(a). Literature is rich in information on the VSI topology, as well as the established and proposed control and switching schemes and application in grid-connected systems [22] [23]. One major drawback of VSI is that, as a buck topology, it requires sufficiently high input voltage for proper functioning. Therefore, when the input voltage is low, another converter stage, usually a boost converter is employed between the DC source and VSI [8]. A schematic diagram of a VSI cascaded with a boost

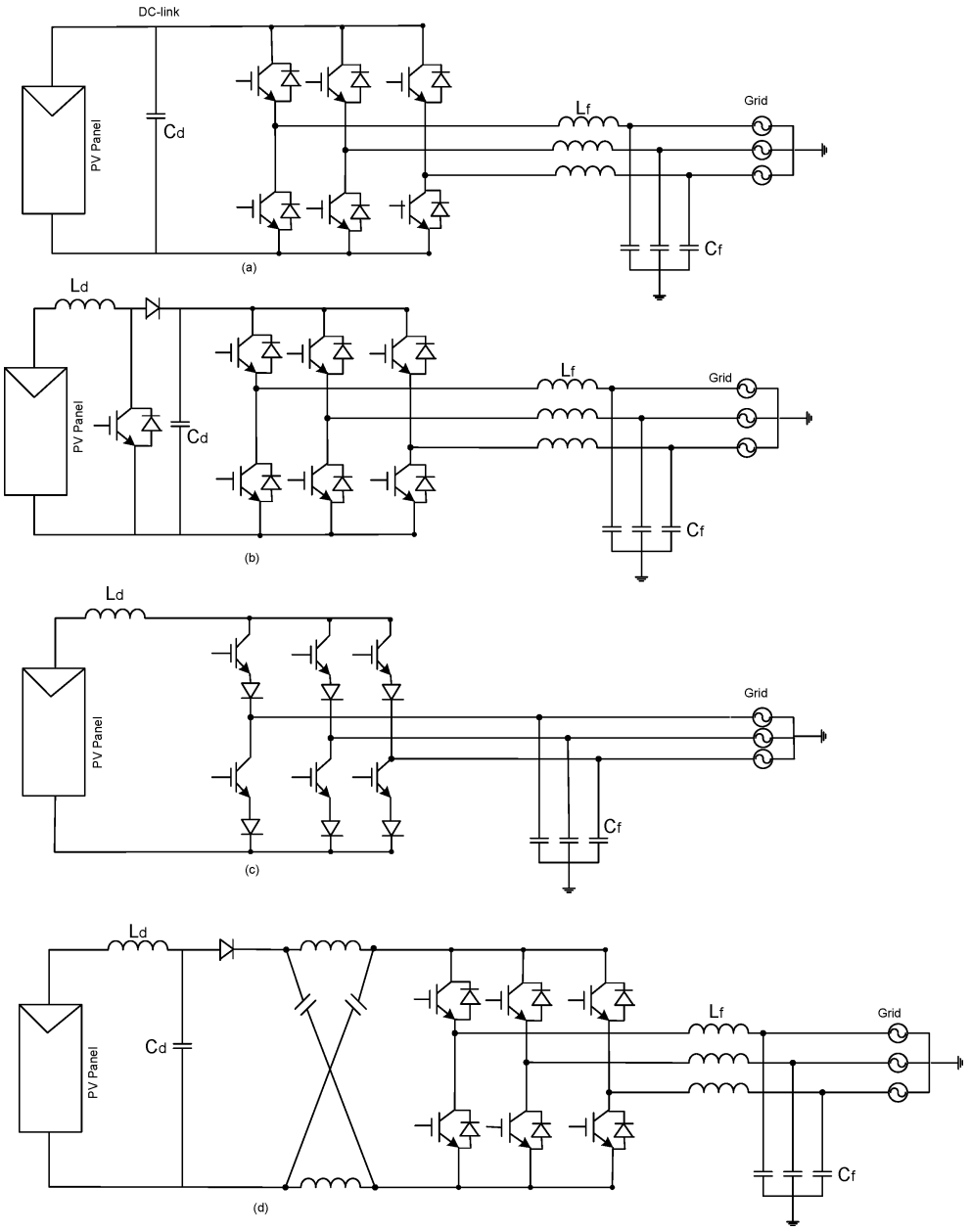

Figure 2.5 PV grid interface topologies. (a) Voltage Source Inverter (VSI), (b) Voltage Source Inverter cascaded with a boost converter, (c) Current Source Inverter (CSI), (d) Z-source Inverter.

converter is shown in Figure 2.5(b). On the other hand, the topology that has been less investigated and adopted when compared with VSI for grid-interface applications is Current Source Inverter (CSI) topology, shown in Figure 2.5(c). Recently, a new topology named "Impedance-Inverter" or Z-source inverter which employs a unique impedance network to couple the converter to the DC source has been adopted for interfacing DG. A schematic diagram of Z-source inverter proposed by Peng in [24] is presented in Figure 2.5(d). The special feature of Z-source inverter is that it overcomes the conceptual and theoretical barriers and limitations of the traditional VSI and CSI topologies and is capable of operating in both buck and boost modes and can also eliminate the requirement of a bulky transformer. Application of Z-source inverter in the field of grid-connected PV system is at a very early stage. However, efforts have been made by [25] and [26] to interface PV module through Z-source inverter to single-phase and three-phase grid, respectively. Since the Z-source is capable of operating in both buck and boost mode, a comparative study between buck-boost inverter and Z-source inverter for PV applications is carried out in [27]. In [27], the experimental results show that the efficiency of Z-source inverter drops more rapidly for high loads compared to that of buck-boost inverter. Though the Z-source inverter can operate both in step-down and step-up modes, it offers more structural complexity than a single-stage grid-connected PV system based on VSI or CSI. Considering that for PV and fuel cell applications the boosting feature is desired, a CSI qualifies as a better candidate than Z-source inverter as it lifts the requirement for the additional impedance requirement used in a Z-source inverter.

Research on CSI topology lags behind that on VSI in DG applications due to its potentially lower efficiency, high energy loss in the DC-link inductor, and less investigated appropriate PWM switching strategies. However, recent developments in RB-IGBT (Reverse blocking Insulated Gate Bipolar Junction Transistors) have contributed towards reduced conduction losses in CSI. RB-IGBT is a special type of IGBT whose structure is similar to conventional IGBT except for the fact that it has a collector isolation area that allows the

IGBT to block reverse voltage. The RB-IGBT has a symmetrical blocking capability [28]. This implies that it can block both forward and reverse voltage in its off-state. As a result, it eliminates the requirement of series connected diodes in the CSI topology. More information regarding its characteristics can be found in [29]. There are other advantageous features that make CSI a more apt topology than the widely used VSI. A literature survey aimed at comparative evaluation of performances of CSI-based and VSI based DG is presented in the subsequent section.

2.6 Performance of CSI-based Topology Compared to VSI-based Topology for Photovoltaic (PV) Application

The CSI topology offers numerous advantages over the VSI topology from the viewpoints of short-circuit current limiting, harmonics, and losses. A CSI doesn't need an AC-side filter inductor when used for grid-interactive application as shown in Figure 2.5(b), and offers direct controllability of the output current. Moreover, CSI has high reliability due to inherent short-circuit current protection capability. The DC-link reactor of the CSI, which acts as a link between the DG and inverter, has a longer lifetime than the DC-link electrolytic capacitor of the VSI [30]. As mentioned earlier in 2.5.3, because of buck characteristic of VSI, a high input voltage is required for stable operation of VSI. Therefore, for grid-connected applications VSI may require an additional DC-DC boost converter if a transformer is not used. However, VSI offers some advantages over CSI topology in terms of efficiency, and ease of control [31]. The control scheme and pulse width modulation techniques for VSI topology are more established and more thoroughly investigated when compared to those for CSI. Comparative study of VSI and CSI for different application has always been of interest to researchers. For FACTS (Flexible AC Transmission System)

application, [32] presents a systematic comparison of the two very competitive topologies, Voltage Source Converter (VSC) and Current Source Converter (CSC). The authors of [32] have made conclusions that can be applied to VSI and CSI topologies in general. They have concluded that voltage ratings of switches for VSI topology are higher than those for a CSI topology. Moreover, the voltage harmonics generated by a VSC are high irrespective of the current injected, whereas the harmonics produced by CSC can be reduced at low current injection levels by reducing the DC side current. Furthermore, when both converters are operating at low switching frequency, waveforms from CSI have better quality compared to those from VSI, which is a desirable feature for high power DG application. Operation of power electronic device at low switching frequency results in lower switching losses. However, reference [32] doesn't talk about conduction losses; therefore, it is difficult to predict which converter topology has more semiconductor losses. In view of this, an analytical derivation of semi-conductor losses for voltage source converter and current source converter is presented in [33]. Reference [33] has concluded based on analytical and experimental results that when both converters are operating in inverting mode, e.g., when they are supplying power to the grid, the conduction losses for voltage source converter topology are lower than those for current source converter topology. However, the analysis in [33] was carried out for inverters made of normal IGBT switches; results are expected to be different for RB-IGBT switches. The work in [33] is further extended to evaluate conduction losses analytically for fuel cell generation system in [34]. In reference [34], the authors have compared a VSI-BC (Boost Converter) topology with a single-stage CSI topology with IGBT switches. The analysis gives the same result as in [33], that for fuel cell applications IGBT-based voltage source inverter in combination with boost converter topology is more advantageous compared to current source inverter in terms of losses. For low-power PV application, a comparison between a VSI-BC combination and CSI is presented in [35]. The inverters employed in [35] are based on MOSFETs. The conclusion drawn in [35] varies from those of [33]. In this case, VSI in combination with boost con-

verter was proven to be more lossy than CSI. For high power PV applications, a systematic comparison and experimental analysis for switching losses, conduction losses and installed power for VSI and CSI topologies are carried out in [36]. In [36] the author has introduced a novel topology for CSI based on RB-IGBT. A schematic diagram for the topology adopted in [36] is shown in Figure 2.6. The justification behind the author's mixed-switch design is that in CSI most of the switching stress is handled by the positive or upper switch group. Though RB-IGBT has reverse blocking capability, the IGBT in series with diode has better switching behavior than the RB-IGBT; therefore, RB-IGBT switches can be used in the negative switch group or lower group. This has resulted in lower number of semiconductor devices, which in turn, results in lower switching losses as compared to the commonly used CSI topology. One major advantage of using RB-IGBT in CSI is that it eliminates the requirement of series diodes, which are normally employed to reduce voltage stress in conventional IGBTs in a current source inverter, and their associated conduction losses.

The upper and lower devices of each leg in a VSI cannot be gated simultaneously as shoot-through can destroy the devices. In a CSI, shoot-through is a valid state and is used for magnitude control of fundamental component of AC-side current.

Combining RB-IGBTs, IGBTs, and diodes the author in [36] has proposed a multi- converter topology that connects multiple independently controlled renewable energy sources to the same grid. The analysis is further extended to evaluate the installed power. It was found that CSI based on RB-IGBT has lower installed power compared to VSI and CSI based on conventional IGBTs and diodes. However, the author has not presented any experimental or simulation analysis for transient performance of the CSI based on RB-IGBT.

The survey documented above shows that CSI possesses a number of favorite features for interfacing DGs, when compared with a VSI topology. Furthermore, development of

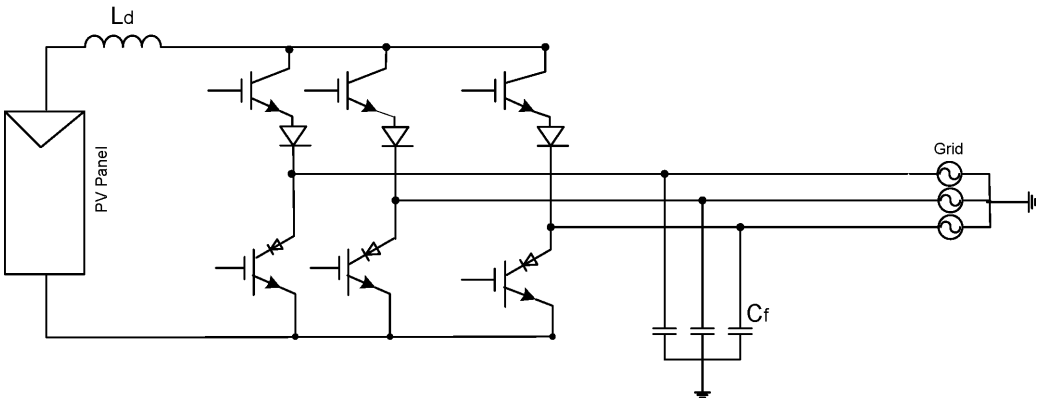

Figure 2.6 Topology of a single-stage grid interface for PV based on a CSI using 3 RB-IGBTs, 3 normal IGBTs, and 3 diodes [36].

RB-IGBT has resulted in a less lossy structure which used to be a major concern for opting to use current source converter topology. Still, there are some disadvantages which make CSI not considered so "favorite" by PV system manufacturers.

A CSI is a preferred topology to interface renewable energy source such as PV to the AC power grid because it can provide smooth current in the DC-side which is suitable for a PV source. It also steps up the voltage from DC-side to AC-side. However, CSI has the problem that it cannot operate when the AC-voltage is low, i.e., during fault [37]. An evaluation of performance of the CSI interfaced with PV source with reduced AC voltage is carried out in [37]. Reference [37] has focused on low voltage fault ride through (LVFRT) capability, which has the ability to remain transiently stable and connected to the power grid without tripping during the grid fault disturbances in specified time, support the power grid during the fault with reactive power, and be able to supply power to the system after the fault clearance. However, reference [37] does not discuss how the CSI interfaced with PV source behaves when the grid is disconnected, i.e., islanding behavior of the PV system based on CSI. It also lacks a comparative study of behaviors of a CSI made of RB-IGBT and a CSI made of conventional IGBT and diodes.

The output current of a CSI has large harmonic contents when the DC-link reactor is not large. On the other hand, a large DC-link reactor is not acceptable from design point of view. Therefore, a new control strategy to reduce the harmonic contents of a single-phase utility-interactive PWM CSI based PV system is proposed in [38]. The control proposed in [39] is without feedback control and is able to eliminate low order harmonics completely. However, the results presented are obtained for a very low-power PV system. No evidence has been presented to prove that the proposed scheme will also work successfully for high-power applications.

The CSI topology has an inherent stability problem caused by the resonance between the AC-side filter capacitance and grid inductance. In [40], these oscillations are damped actively by generating a damping current from the filter capacitor voltage. Reference [40] proposes a closed-loop charge control algorithm in a synchronously-rotating reference frame to suppress the natural frequency of oscillation produced by the filter. The CSI topology adopted in [40] is based on line-commutated thyristors. A simple method to suppress the resonance oscillations in a PWM current-source converter is discussed in [41]. The method is based on pulse control and suppresses the resonance current caused by the CSI's AC-side low-pass filter. The advantage of this method is in that it does not need any extra feedback loop to suppress the oscillations. However, the system employed in [41] has not been integrated with any renewable energy source.

The performance of a single-phase, grid-connected current-source inverter is investigated in [42]. In [42], a CSI is combined with a boost converter which acts as the wave-shaper. However, neither the dynamic performance of the PV inverter in response to the variations in solar insolation level nor the behavior of the PV system during fault conditions is addressed in reference [42]. Reference [43] evaluates the performance of a 3-phase transformer-less grid-connected PV system based on CSI with a new Maximum Power Point Tracking system and PWM control scheme. The MPPT proposed in [43] tracks the

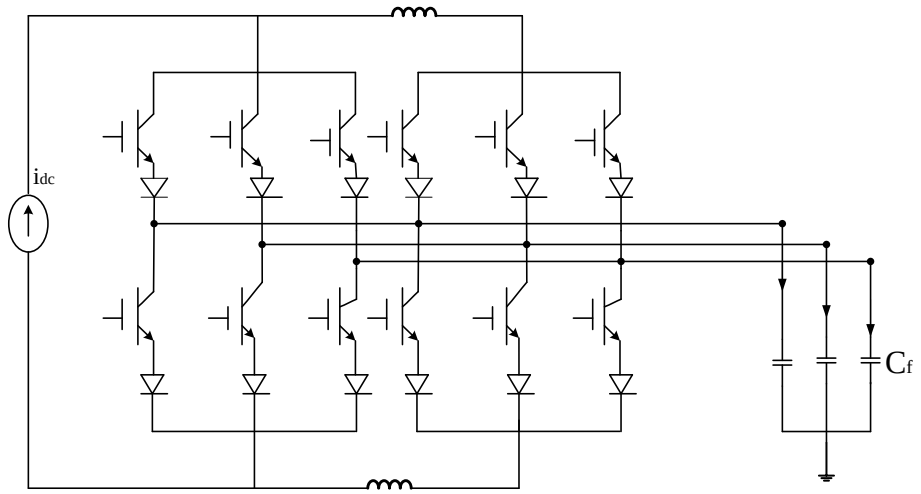

Figure 2.7 Three-phase five-level topology for Current Source Inverter.

maximum power by adjusting the modulation factor. One major drawback of the control method proposed in [43] is that it does not allow the PV inverter to operate in stand-alone mode. In some scenarios, where intentional islanding is desired, stand-alone mode of operation of a PV inverter is a requirement.

Discussions presented so far indicate that CSI topology proves to be a viable option for a PV inverter in the future for its inherent boosting capability and smooth DC-input current. In addition, with the evolution of RB-IGBT switches, use of series diodes and the corresponding losses can be eliminated. However, producing a strong inverter solution may not ensure successful operation of a PV system. Along with the inverter, other issues such as harmonics in the current injected into the grid, high power rating of PV system, low switching frequency, reduced sensor requirements need to be addressed. To address such concerns, a multilevel structure for CSI-based PV system is proposed in this research work. A literature survey on multilevel topologies is presented in the following Section.

2.7 Multilevel Inverter Topologies

Multilevel inverters have drawn tremendous attention in recent years and have been studied for high-voltage and high-power applications. By increasing the number of levels in a given topology, the output voltages in the case of VSI, and output currents in the case of CSI, assume stair-case waveforms with increased number of steps. This results in closer-to-sinusoidal AC quantity waveforms with reduced Total Harmonic Distortion (THD) at reduced switching frequency. The operation of a multilevel inverter at a low switching frequency results in lower switching losses and a higher power transfer capability. For their advantageous features, multilevel inverters have been adopted in Distributed Generation (DG) application area. The most commonly-used multilevel inverter structures are based on Voltage-Source Inverter (VSI) topology. The thoroughly researched VSI-based multilevel inverters can be categorized under Neutral Point Clamped (NPC), Flying Capacitor (FC), Cascade full bridge and the recently-introduced Hybrid and Hexagram Inverters [44]. The research for multilevel VSI is rich as compared to multilevel CSI. To date, most of the multilevel CSIs reported in the literature are based on a single-phase cell, basically variations of the generalized multicell structure proposed in [45], shown in Figure 2.7. The generalized structure proposed in [45] has been extended to a three-phase topology in [46]. The topology proposed in [46] is a three-phase 5-level CSI that uses only two intermediate DC-link inductors and a single DC current source. A multi-modular structure based on CSI for superconducting magnetic energy storage system is proposed in [47]. A modified three-phase multicell CSI topology is proposed in [48] which is different from the topologies proposed earlier in terms of the number of current levels. The number of current levels produced by multicell CSI in [48] is $2n$ compared to $2n + 1$ produced by others, where n is the number of CSI modules employed. Some advanced structures for multilevel CSI are discussed in [49] and [50]. The work presented in [45]- [50] mainly revolves around modulation strategy and switching. Moreover, the analysis carried out in the aforemen-

tioned literatures is based on the assumption that there is an ideal current source on the DC side. In addition, an even distribution of DC-side current is demanded in the majority of the CSI-based multilevel topologies introduced so far, asking for a robust DC-side controller. Control techniques for a multi modular current source inverter are discussed in [51,52,53,54]. Control algorithms for multilevel CSI structures are not fully investigated as opposed to the case of VSI-based multilevel topologies.

2.8 A Summary of Research on 3-phase Grid-connected PV System

Discussions on three-phase inverters presented in this chapter show that though CSI offers numerous advantages, it is not a widely-used topology for interfacing renewable energy sources as compared to VSI. CSI qualifies as a candidate for DG application for its smooth DC-input current and inherent boosting capacity; however, the lossy DC-link inductor and oscillations resulting from output filter overshadows its merits and VSI topology is opted and frequently used in place of CSI. To make CSI as competitive as VSI, a fair amount of research has been carried out in the field of current control, switching strategy, suppression of harmonics, damping of oscillations, and efficient energy storage. However, a few research work has been focused on modeling, design, analysis, and multilevel structure of CSI-based PV systems. With numerous advantageous features of CSI, the research can be extended to design a multi-module, multilevel converter system that will contribute towards injecting clean sinusoidal current with lower switching loss and accommodating high power. With the development of revolutionary switches and efficient energy storage system, it is very likely that CSI will win the competition against VSI in PV system application in the near future.

Chapter 3

Three-phase grid-connected Photovoltaic System based on Current Source Inverter

3.1 Introduction

This chapter presents a mathematical modeling for the three-phase grid-connected Photovoltaic (PV) system based on Current Source Inverter (CSI). The chapter also discusses designs of controllers for DC-side and AC-side currents. The DC-side current controller is responsible for making the current on the DC side of the inverter track a reference value that corresponds to the maximum power point at a particular insolation level. The AC-side current controller works in coordination with the DC-side current controller and injects a sinusoidal current into the grid that is in phase with the voltage at the Point of Common Coupling (PCC).

In this chapter, to design current controllers, the phasor quantities are transformed

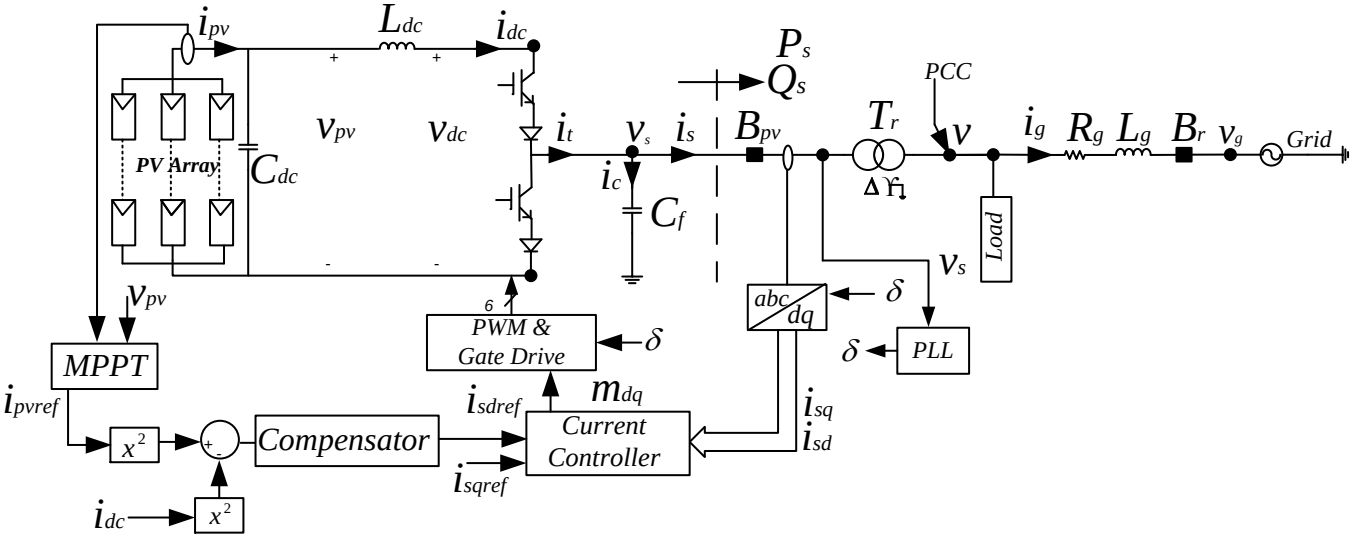

Figure 3.1 Single-line schematic diagram of a three-phase, single-stage, grid-connected PV system based on CSI.

from stationary frame of reference to a rotating frame of reference. Rotating frame of reference reduces number of phasor quantities, thus simplifying the controller design task. A detailed method for transforming the phasor quantities from stationary frame to rotating frame is provided. Model of the CSI developed in this chapter is a detailed switched-model simulated in PSCAD/EMTDC (Power System Computer Aided Design/Electro Magnetic Transient Direct Current) simulation package. This chapter introduces a simple, yet reliable method to tune the parameters of the controller for independent control of active and reactive components of the current on the AC-side.

3.2 Structure of the PV System

Figure 3.1 illustrates the single-line diagram of the three-phase, single-stage, grid-connected PV system with a CSI as the power-conditioning unit. The PV array is a parallel combi-

nation of n_p PV modules, while each PV module is a series combination of n_s number of PV cells. The DC-side inductor L_{dc} filters out ripples in the DC-side current and allows its control. The AC-side of the inverter is interfaced with the primary side of the transformer T_r through a capacitive filter composed of three Y-connected capacitors, C_f. Function of the capacitive filter, C_f, is to absorb switching harmonics and produce clean sinusoidal current at the grid interface. Breaker B_{pv} is an integral part of the PV system and is provided to protect the PV system by isolating it when there is a fault on the secondary side of the transformer, T_r. Primary side of the transformer is delta-connected whereas its secondary side is star-connected, with a solidly grounded neutral point. Resistance and inductance of the distribution line are represented by R_g and L_g, respectively. P_s and Q_s, respectively, represent active and reactive powers supplied by the PV system to the distribution system. Breaker B_r is part of the protection system installed by the utility.

The control structure proposed for the CSI-based PV system is composed of an outer current control loop designed to control the DC-side current and an inner current control loop responsible for controlling the current that is injected into the grid. A Maximum Power Point Tracker (MPPT) based on Perturb & Observe (P&O) method is employed to ensure that the PV array is operating at its maximum power [55].

3.2.1 Switching of CSI

Figure 3.2 presents the schematic diagram of a CSI. At any instant of time, one and only one of the top switches, T_A^+, T_B^+, or T_C^+, and one and only one of the bottom switches, T_A^-, T_B^- or T_C^-, are conducting [56] [57]. It is acceptable if two switches in the same leg conduct at the same time. Table 3.1 displays switching arrangements for the CSI of Figure 3.2. Figure 3.3 illustrates the simulated tri-level terminal current, i_{ta} of the CSI. The capacitive filter, C_f, suppresses the switching harmonic contents of the terminal current, resulting in the sinusoidal current i_{sa}, shown in Figure 3.3.

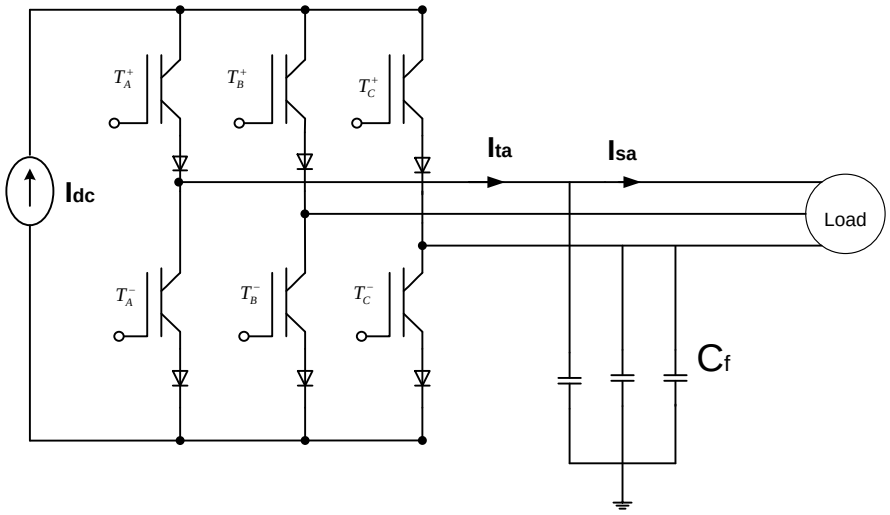

Figure 3.2 Schematic diagram of a Current Source Inverter.

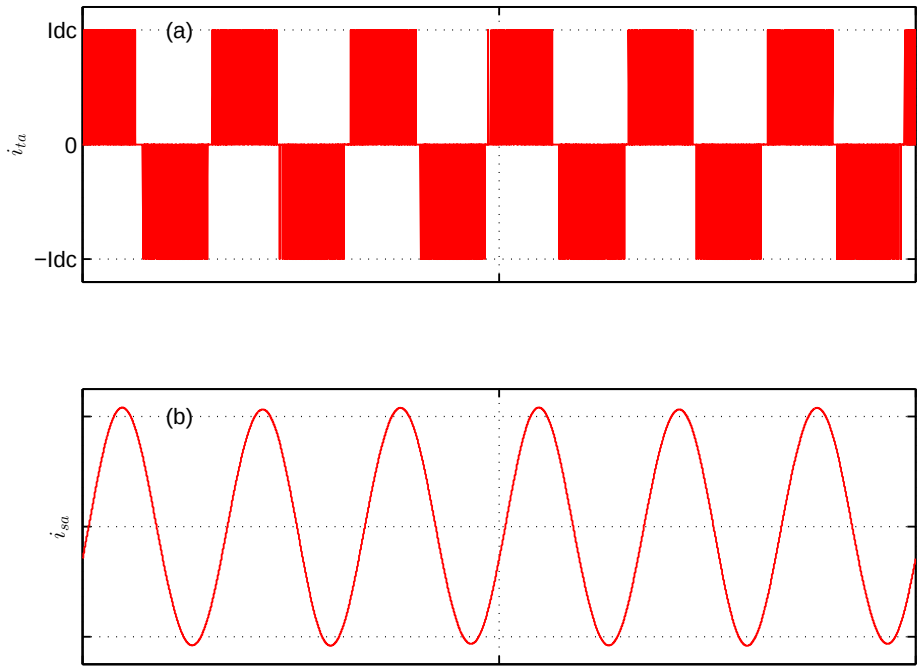

Figure 3.3 Simulated switching behavior of the CSI (a) Terminal current of CSI (b) Filtered AC-side current.

Table 3.1: Switching Function of CSI

switching function	Switching logic	T_A^+	T_A^-	T_B^+	T_B^-	T_C^+	T_C^-
T_A	1 -1 0	ON OFF ON or OFF	OFF ON ON or OFF				
T_B	1 -1 0			ON OFF ON or OFF	OFF ON ON or OFF		
T_C	1 -1 0					ON OFF ON or OFF	OFF ON ON or OFF

3.3 Characteristics of PV Array

PV array is an integral part of the PV system. The $i - v$ characteristic of the array is described by equation (3.1) [58].

$$i_{pv} = n_p i_{ph} - n_p i_{rs} \left[\exp\left(\frac{q}{kT_c A} \frac{v_{pv}}{n_s} \right) - 1 \right] \tag{3.1}$$

In (3.1), q is the unit charge, k the Boltzman's constant, A the p-n junction ideality factor, and T_c the cell temperature. Current i_{rs} is the cell reverse saturation current, which varies

with temperature according to equation (3.2):

$$i_{rs} = i_{rr} \left[\frac{T_c}{T_r}\right]^3 \exp\left(\frac{qE_G}{kA}\left[\frac{1}{T_r} - \frac{1}{T_c}\right]\right) \tag{3.2}$$

In (3.2), T_r is the cell reference temperature, i_{rr} the reverse saturation current at T_r, and E_G the band-gap energy of the cell. The photovoltaic current i_{ph} in (3.1) depends on the insolation level and cell temperature according to equation (3.3):

$$i_{ph} = \left[i_{scr} + K_\vartheta \left(T_c - T_r\right)\right] \frac{S}{S_{STC}} \tag{3.3}$$

In (3.3), i_{scr} is the cell short-circuit current in Amperes at the reference temperature and irradiation, K_ϑ a temperature coefficient, S the insolation in kW/m^2 and S_{STC} the insolation level at standard temperature condition (STC) which is equal to 1 kW/m^2. Power delivered by the PV array is calculated by multiplying both sides of (3.1) by v_{pv}.

$$P_{pv} = n_p i_{ph} v_{pv} - n_p i_{rs} v_{pv} \left[\exp\left(\frac{q}{kT_cA}\frac{v_{pv}}{n_s}\right) - 1\right] \tag{3.4}$$

Substituting current i_{ph} from (3.3) in (3.4), power P_{pv} becomes

$$\begin{aligned} P_{pv} = n_p \left[i_{scr} + K_\vartheta \left(T_c - T_r\right)\right] \frac{S}{S_{STC}} v_{pv} \\ -n_p i_{rs} v_{pv} \left[\exp\left(\frac{q}{kT_cA}\frac{v_{pv}}{n_s}\right) - 1\right] \end{aligned} \tag{3.5}$$

Based on (3.5), it is evident that the power delivered by the PV array is a function of insolation level, S, at any given temperature. Since the inverter employed in the PV system of this work is of current-source type. The power-versus-current characteristic of the PV array has to be examined (rather than the power-versus-voltage characteristic). Figure 3.4 illustrates the power-versus-current characteristic of the PV array based on the parameters listed in the Appendix A for insolation levels of 0.1, 0.5 and 1 kW/m^2. Figure 3.4 shows that P_{pv} can be maximized by control of current i_{pv}, based on a Maximum Power Point Tracking (MPPT) strategy [59].

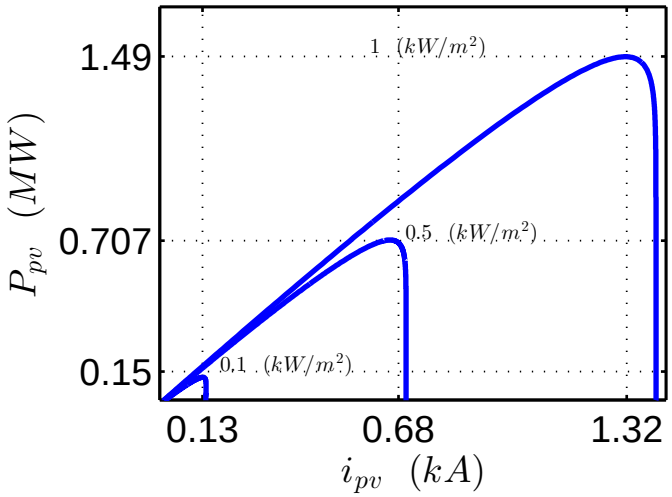

Figure 3.4 $P - I$ characteristic of a PV array for $S = 0.1$, 0.5 and 1 kW/m^2.

3.4 Dynamics of CSI-based PV System

A mathematical model is essential for both system analysis and controller design. In this section, the system of Figure 3.1 is modeled in both space-phasor and dq-frame forms.

3.4.1 Space-Phasor Representation of the CSI

The CSI of Figure 3.1 is a 6-pulse converter employing IGBT switches, operated under Sinusoidal Pulse Width Modulation (SPWM) strategy [60]. The output current of the CSI, $\vec{i}_t$, is related to the DC-side current i_{dc} as follows:

$$\vec{i}_t = \vec{m} i_{dc} \tag{3.6}$$

where $\vec{i}_t$ and $\vec{m}$ are the space phasors corresponding to the CSI terminal currents and the PWM modulating signals. Similarly, the DC-side voltage, v_{dc}, is related to the CSI AC-side voltage space phasor as

$$v_{dc} = \vec{m} v_s \tag{3.7}$$

Voltage and current at the PCC can be expressed in space-phasor form as [61]:

$$\overrightarrow{v_s} = \frac{2}{3}(v_{sa} + e^{-j\frac{2\pi}{3}} v_{sb} + e^{j\frac{2\pi}{3}} v_{sc}) \tag{3.8}$$

$$\overrightarrow{i_s} = \frac{2}{3}(i_{sa} + e^{-j\frac{2\pi}{3}} i_{sb} + e^{j\frac{2\pi}{3}} i_{sc}) \tag{3.9}$$

and

$$\overrightarrow{i_s^*} = \frac{2}{3}(i_{sa} + e^{j\frac{2\pi}{3}} i_{sb} + e^{-j\frac{2\pi}{3}} i_{sc}) \tag{3.10}$$

Multiplying (3.8) and (3.10), and considering real parts of both sides one gets

$$\begin{aligned} Re\left\{\overrightarrow{v_s}\,\overrightarrow{i_s^*}\right\} = \frac{4}{9}\,(&v_{sa}i_{sa} + v_{sb}i_{sb} + v_{sc}i_{sc} \\ &-\frac{v_{sa}i_{sb}}{2} - \frac{v_{sa}i_{sc}}{2} - \frac{v_{sb}i_{sa}}{2} - \frac{v_{sb}i_{sc}}{2} - \frac{v_{sc}i_{sa}}{2} - \frac{v_{sc}i_{sc}}{2}) \end{aligned} \tag{3.11}$$

Equation (3.11) can be further simplified to

$$Re\left\{\overrightarrow{v_s}\,\overrightarrow{i_s^*}\right\} = \frac{4}{9}\left[\frac{3}{2}\left(v_{sa}i_{sa} + v_{sb}i_{sb} + v_{sc}i_{sc}\right) - \frac{1}{2}\left(v_{sa} + v_{sb} + v_{sc}\right)\left(i_{sa} + i_{sb} + i_{sc}\right)\right] \tag{3.12}$$

For a balanced three-phase system currents, i_{sa}, i_{sb}, i_{sc} are related as:

$$i_{sa} + i_{sb} + i_{sa} = 0 \tag{3.13}$$

Substituting (3.13) in (3.12) one gets

$$Re\left\{\overrightarrow{v_s}\,\overrightarrow{i_s^*}\right\} = \frac{2}{3}\left(v_{sa}i_{sa} + v_{sb}i_{sb} + v_{sc}i_{sc}\right) \tag{3.14}$$

For a three-phase systems the real power, P_s in time domain is expressed as [61]:

$$P_s = (v_{sa}i_{sa} + v_{sb}i_{sb} + v_{sc}i_{sc}) \tag{3.15}$$

Substituting expression for P_s from (3.15) in (3.14) one gets

$$Re\left\{\overrightarrow{v_s}\,\overrightarrow{i_s^*}\right\} = \frac{2}{3}P_s \tag{3.16}$$

Equation (3.16) can be rewritten as:

$$P_s = \frac{3}{2}Re\left\{\overrightarrow{v_s}\,\overrightarrow{i_s^*}\right\} \tag{3.17}$$

Assuming the switching losses of the inverter negligible, the DC-side power of the inverter, P_{dc}, is equal to the power delivered on the AC-side. Therefore,

$$P_{dc} \approx P_s = \frac{3}{2}Re\left\{\overrightarrow{v_s}\,\overrightarrow{i_s^*}\right\} \tag{3.18}$$

3.4.2 *DQ*-Frame Representation of the PV System

To simplify the analysis and controller design, the space-phasor variables of the system model are projected on a synchronously rotating *dq*-frame, where the variables at steady-state assume time-invariant values. The relationship between the space-phasor and *dq*-frame variables is expressed by:

$$\overrightarrow{f} = (f_d + jf_q)e^{j\delta} \tag{3.19}$$

where $\overrightarrow{f}$ represents a space-phasor variable, f_d and f_q are the equivalent *dq*-frame components and δ is the reference angle of the *dq*-frame. Another useful relationship is defined between the derivatives of the space phasor and *dq*-frame variables as follows.

$$\frac{d\vec{f}}{dt} = \frac{d}{dt}\left[(f_d + jf_q)\,e^{j\delta}\right]$$

$$= \left(\frac{df_d}{dt} + j\frac{df_q}{dt}\right) e^{j\delta} + j\frac{d\delta}{dt}\left(f_d + jf_q\right) e^{j\delta}$$

$$= \left(\frac{df_d}{dt} + j\frac{df_q}{dt}\right) e^{j\delta} + j\omega\left(f_d + jf_q\right) e^{j\delta} \tag{3.20}$$

where ω is the dq-frame angular speed that is related to δ according to (3.21).

$$\omega = \frac{d\delta}{dt} \tag{3.21}$$

Based on (3.19), P_s in (3.18) can be expressed as:

$$P_s = \frac{3}{2}\mathrm{Re}\left\{\underbrace{\left[\left(v_{sd} + jv_{sq}\right) e^{j\delta}\right]}_{\vec{v}_s}\underbrace{\left[\left(i_{sd} + ji_{sq}\right) e^{j\delta}\right]^*}_{\vec{i}_s^*}\right\} \tag{3.22}$$

which can be further simplified to

$$P_s = \frac{3}{2}\left(v_{sd}i_{sd} + v_{sq}i_{sq}\right) \tag{3.23}$$

The DC-side dynamics can be described by

$$L_{dc}\frac{di_{dc}}{dt} = v_{pv} - v_{dc} \tag{3.24}$$

Multiplying both sides of equation (3.24) by the current i_{dc} results in the following power relation:

$$L_{dc}i_{dc}\frac{di_{dc}}{dt} = v_{pv}i_{pv} - v_{dc}i_{dc} \tag{3.25}$$

The two terms on the right hand side of (3.25) represent the power delivered by the PV array, P_{pv}, and the power received by the DC-side of the inverter, P_{dc}, respectively. Thus, one can obtain the power balance equation as:

$$\frac{1}{2}L_{dc}\frac{di_{dc}^2}{dt} = P_{pv} - P_{dc}\left(\approx P_s\right). \tag{3.26}$$

Substituting the expression for P_s from (3.23) in (3.26), one gets

$$\frac{1}{2}L_{dc}\frac{di_{dc}^2}{dt} = P_{pv} - \frac{3}{2}\left(v_{sd}i_{sd} + v_{sq}i_{sq}\right) \tag{3.27}$$

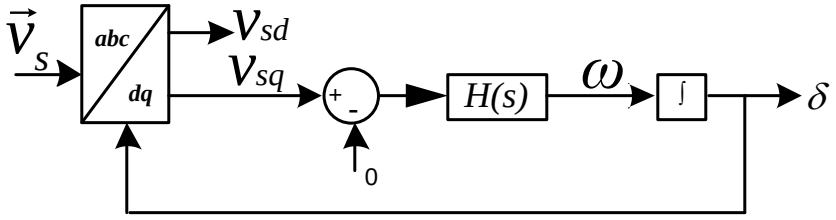

Figure 3.5 Block diagram of the Phase-Locked Loop (PLL).

3.5 Controller for CSI-based PV System

The controller of a grid-connected CSI-based PV system is expected to control the DC- and AC-side currents to ensure that: (i) a high-quality sinusoidal current is injected into the grid, (ii) the real power injected into the grid is equal to the maximum power that can be extracted from the PV panel under all conditions, and (iii) the reactive power at the interface with the grid assumes the desired value. As illustrated by Figure 3.1, the Pulse Width Modulation (PWM) and control of the CSI need to be synchronized to the grid voltage through a Phase-Locked Loop (PLL) [62]. Figure 3.1 also shows that the errors between the reference commands, i_{sdref} (obtained from MPPT through DC-side current controller) and i_{sqref}, and the d-axis and q-axis components of the AC-side current are processed by two PI controllers to generate the modulating signals, m_d and m_q. Even though the PI controller is simple in structure and easy to implement, proper tuning of its parameters requires adequate insight. An intuitive method for tuning of the PI controller parameters is proposed in this section.

3.5.1 Phase-Locked-Loop (PLL)

As discussed earlier, the AC variables of the system are projected on a dq-frame which is rotating at angular speed ω. In steady state, the AC variables are sinusoidal functions of

the grid frequency, ω_0. If the dq-frame angular speed is adjusted to the grid frequency, the transformed quantities become time-invariant in steady-state, simplifying the controller design. This is achieved by means of a Phase Locked Loop (PLL) [62] whose block diagram is given in Figure 3.5. As shown in Figure 3.5, the input to the PLL block is the sinusoidally-varying voltage and the output is the angle for abc-to-dq and dq-to-abc transformations, δ. The voltage $\vec{v}_s$ is resolved into its d- and q-axis components based on (3.19). In Figure 3.5, the voltage v_{sq} is regulated to zero using a PI controller, $H(s)$. Regulating q-axis component of the voltage to zero makes the active and reactive powers, P_s and Q_s, independent of the voltage v_{sq}. From (3.23),

$$P_s = \frac{3}{2} v_{sd} i_{sd}. \tag{3.28}$$

Hence, P_s is proportional to, and can be controlled by, i_{sd}. Similarly, the dq-frame expression for the reactive power assumes the form:

$$\begin{aligned} Q_s &= \frac{3}{2}\mathrm{Im}\left\{\overrightarrow{v_s}\,\overrightarrow{i_s^*}\right\} \\ &= \frac{3}{2}\mathrm{Im}\left\{\underbrace{\left[(v_{sd}+jv_{sq})\,e^{j\delta}\right]}_{\vec{v}_s}\underbrace{\left[(i_{sd}+ji_{sq})\,e^{j\delta}\right]^*}_{\vec{i}_s^*}\right\} \\ &= -\frac{3}{2} v_{sd} i_{sq}. \end{aligned} \tag{3.29}$$

Equation (3.29) indicates that Q_s can be controlled by i_{sq}.

3.5.2 Design of Inner Current Control Loop

Equations (3.28) and (3.29), respectively, show that active and reactive powers delivered by the CSI can be adjusted by controlling i_{sd} and i_{sq}, respectively. Figure 3.6 shows the

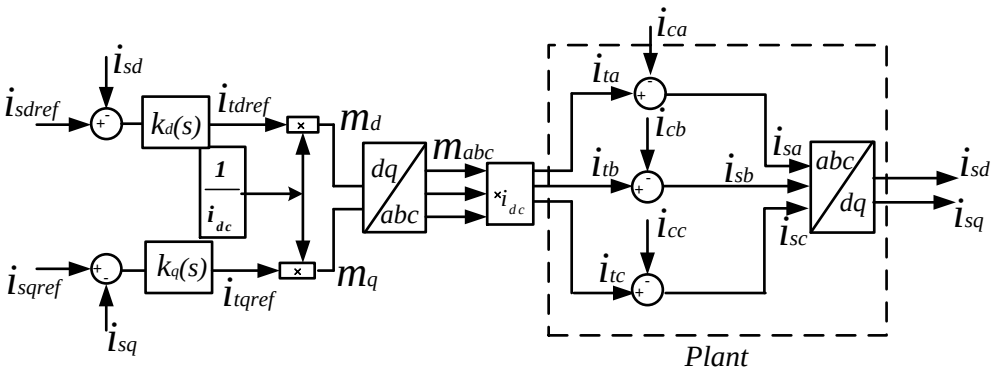

Figure 3.6 Block diagram of the CSI AC-side current control system.

block diagram of the CSI AC-side current controller. Controller structures $k_d(s)$ and $k_q(s)$ in Figure 3.6 are expressed as:

$$k_d(s) = k_q(s) = k_p + \frac{k_i}{s} \tag{3.30}$$

where k_p nd k_i are the proportional and integral gains, respectively. Control signals m_d and m_q are obtained as

$$m_d = \frac{i_{tdref}}{i_{dc}} \text{ and } m_q = \frac{i_{tqref}}{i_{dc}} \tag{3.31}$$

where i_{tdref} and i_{tqref} are current references derived from the outputs of the compensators $k_d(s)$ and $k_q(s)$, respectively. The d-axis component of the inverter output current, i_{td}, is related to the current i_{sd} as:

$$i_{td} = i_{cd} + i_{sd} \tag{3.32}$$

where i_{cd} is d-axis component of the filter capacitor current. It should be noted that with a proper filter design, the fundamental-frequency component of the capacitor current will be very small, i.e., i_{cd} is negligible as compared to i_{sd}. The same discussion can be made for the q-axis components. Therefore, one can write

$$i_{td} \approx i_{sd} \approx m_d i_{dc} \text{ and } \; i_{tq} \approx i_{sq} \approx m_q i_{dc} \tag{3.33}$$

Under the assumption that i_{cd} =0, the following transfer function can be written for the closed-loop control system of i_{sd} illustrated in Figure 3.6.

$$T(s) = \frac{i_{sd}}{i_{sdref}} = \frac{k_p + \frac{K_i}{s}}{k_p + \frac{k_i}{s} + 1} = \frac{s\frac{k_p}{k_p+1} + \frac{k_i}{k_p+1}}{s + \frac{k_i}{k_p+1}} \tag{3.34}$$

As the value of k_p increases the pole of the transfer function $T(s)$ in (3.34) approaches the origin of s-plane, which is not desirable. Therefore, to imitate the transient behavior of a first-order system, k_p should be chosen to be small. k_i, as the inverse of time-constant. Thus, k_p and k_i can be written as:

$$k_p \approx 0 \; and \; k_i = \frac{1}{\tau_i} \tag{3.35}$$

and

Substituting the values of k_p and k_i in (3.34) the transfer function $T(s)$ becomes

$$T(s) = \frac{i_{sd}}{i_{sdref}} = \frac{\frac{1}{\tau_i}}{s + \frac{1}{\tau_i}} = \frac{1}{\tau_i s + 1} \tag{3.36}$$

In the first order system represented by (3.36), τ_i determines the controller response time. For fast response, the range of τ_i varies between 0.5 ms to 5 ms.

3.5.3 Design of Outer Current Control Loop

Equation (3.27), after substituting $v_{sq} = 0$, represents a system with i_{sd} as the input, i_{dc}^2 the output and v_{sd} the disturbance input. If time constant τ_i in the PI compensator of the inner current control loop is properly selected, i_{sd} can be approximated to i_{sdref}. Therefore, (3.27) can be rewritten as:

$$\frac{1}{2}L_{dc}\frac{di_{dc}^2}{dt} \approx P_{pv} - \frac{3}{2}v_{sd}i_{sdref} \tag{3.37}$$

The DC-link current controller designed on the basis of (3.37) is illustrated in Figure 3.7. The fact that P_{pv} is product of v_{pv} and i_{pv} makes the system nonlinear. To mitigate the impact of nonlinearity, i_{sdref} can be derived in the following way:

$$i_{sdref} = u_i + \eta \underbrace{\left(\frac{P_{pv}}{\frac{3}{2} v_{sd}} \right)} \tag{3.38}$$

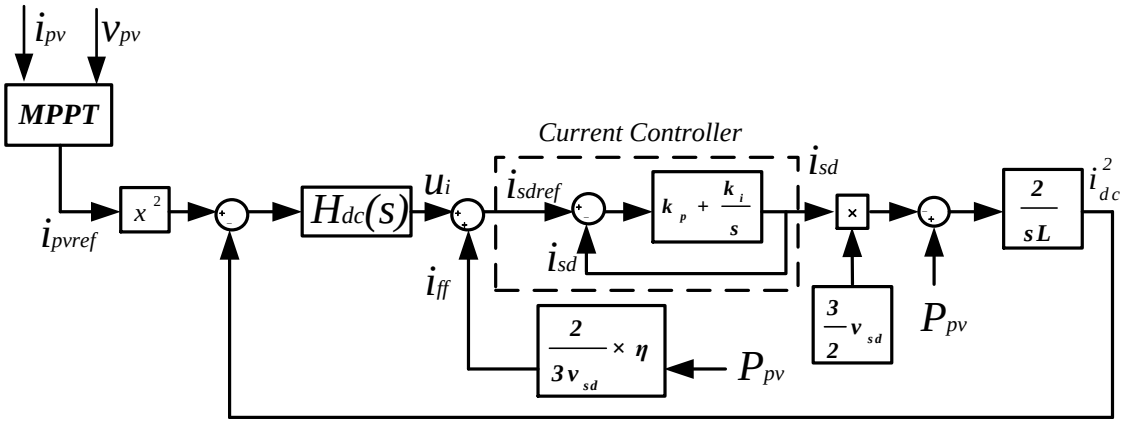

Figure 3.7 Closed-loop control structure of the DC-side current.

where u_i is a new control input, shown in Figure 3.7. Note that i_{ff} is a feed-forward signal that can be enabled or disabled when the binary multiplier η assumes the value unity or zero. Substituting for i_{sdref} from (3.38) in (3.37), one gets

$$\frac{L_{dc}}{2} \frac{di_{dc}^2}{dt} \approx (1 - \eta) P_{pv} - \frac{3}{2} v_{sd} u_i. \tag{3.39}$$

Equation (3.39) indicates that if $\eta = 1$, the impact of the PV array nonlinearity on the DC-side current control is eliminated, and the effective control unit becomes an integrator.

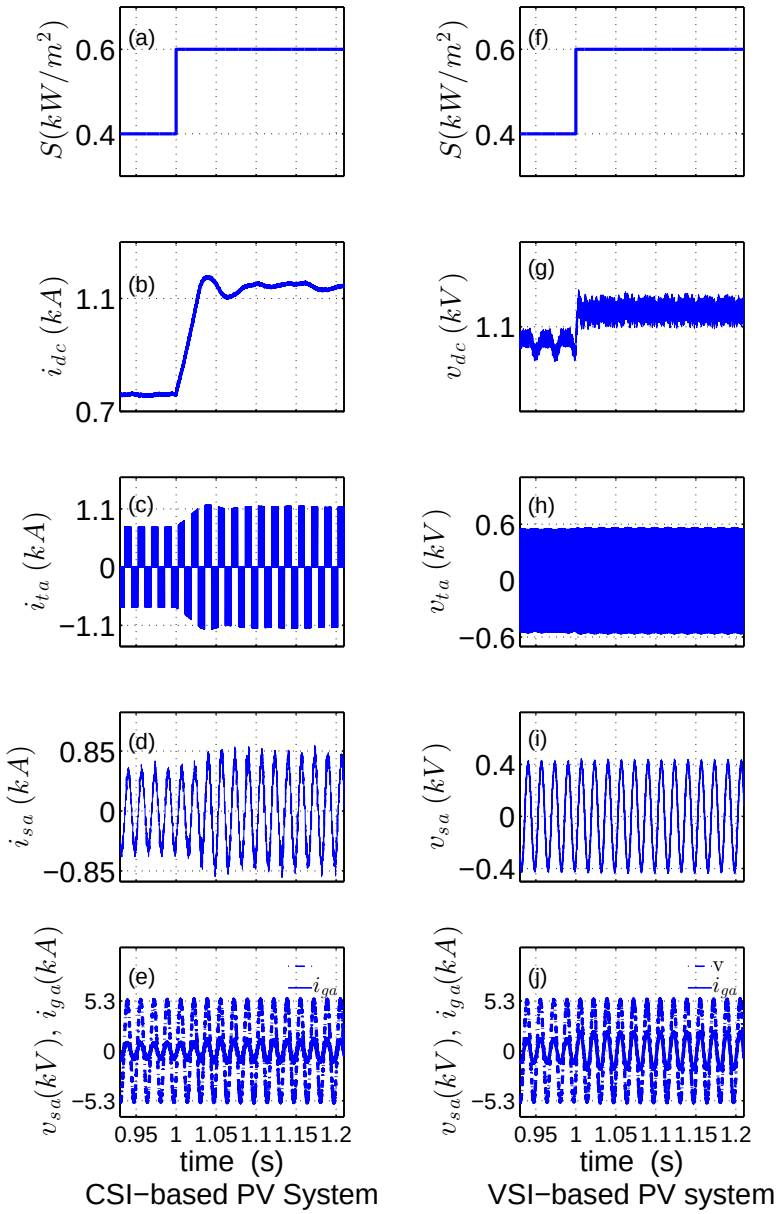

Figure 3.8 PV system behaviors in response to a step-change in insolation level for CSI- and VSI-based PV systems. (S =Insolation level; i_{dc} = DC-side current of CSI; v_{dc} = DC-side voltage of VSI; i_{ta} = Phase-a AC terminal current of CSI; v_{ta} = Phase-a AC terminal voltage of VSI; i_{sa} CSI phase-a filtered current injected into the grid; v_{sa} = VSI phase-a filtered voltage at the grid interface; v_a = Phase-a voltage at the PCC; i_{ga} = Phase-a current at the PCC).

3.6 Comparative performance evaluation of the CSI-based PV system with the VSI-based PV system

The objective of this section is to evaluate the performance of the CSI-based PV system in comparison with that of a VSI-based PV system. The results for VSI-based PV system are produced by simulating the system presented in [63]. A schematic diagram of the VSI-based PV system is provided in the Appendix B.

3.6.1 Case study 1: Change in Insolation Level

In this case study, the behaviors of the VSI- and CSI-based PV systems in response to a change in insolation level are illustrated. Since VSI and CSI are dual topologies, the characteristic of voltage in CSI is analogous to that of current in VSI, and vice versa. Initially, the insolation level is set to 0.4 kW/m^2. At $t = 1$ s, the insolation level is step-changed to 0.6 kW/m^2, as shown in Figure 3.8(a). With the change in insolation level, the CSI DC-side current reference changes from 0.7 kA to 1 kA by the maximum power point tracker. The new reference is tracked by the outer current control loop or the DC-side current controller, as shown in Figure 3.8(b). Since the terminal current of the CSI, i_t, is linearly related to the DC-side current, i_{dc}, it is also changed as shown in Figure 3.8(c). The AC-side current reference is derived from the DC-side current control loop. Since there is an increase in the DC-side current, the d-axis current reference, i_{sdref}, increases, and so does the current i_{sa}, as shown in Figure 3.8(d). With the increase in i_{sa}, the current on the secondary side of the transformer, i_{ga}, also increases. Presently, the utility mandates that the current injected by the inverter, i_{ga}, be in-phase with the voltage at the PCC. This is shown in Figure 3.8(e). Figures 3.8(g)-(j) show the performance of a VSI-based PV system in response to the same step change in insolation level. One can observe in Figure 3.8(g) a step change in the DC-side voltage level, v_{dc}, of the VSI as a result of a

change in insolation level, similar to that in DC-side current of CSI. The AC-side terminal voltage of VSI, shown in Figure 3.8(h), is a two-level quantity whereas the AC-side terminal current of CSI is a three-level quantity. Figure 3.8(i) illustrates the filtered output voltage of the VSI. The unity power factor maintained by the VSI-based PV system at the PCC is illustrated in Figure 3.8(j). From this case study, it can be inferred that the performance of the CSI-based PV system is quite satisfactory and even superior to that of VSI-based PV system due to three-level output current (as compared to two-level output voltage of VSI), simpler AC-side filter design and direct control of injected current (as compared to indirect output current control in VSI).

3.6.2 Case study 2: Fault Conditions

Fault on the grid-side of the inverter results in oscillations of current and voltage on the DC-side of the inverter [64] [65] Oscillations in the DC-side current are not desirable as the inverter requires a smooth input DC-current. In case of VSI-based PV system, the controller regulates the DC-side voltage; therefore, there is no direct control on the DC-side current. On the contrary, in CSI-based PV system, the DC-side current is regulated and limited. As a result, the current on the AC-side of the inverter may not show a sharp rise under fault. This case study is designed to present a comparative analysis of behaviors during fault for CSI- and VSI-based PV systems. For this study, the insolation level is maintained at 1 kW/m^2. In real life, when the fault occurs on the grid-side, and the breaker B_r opens, the anti-islanding scheme must act to protect the inverter and personnel. Since the objective of this case study is to show the impact of a change in the AC-side voltage level on the performance of the PV system, the anti-islanding protection is disabled. Four fault types, i.e., Single Line-to-Ground (SLG), Double Line-to-Ground (DLG), Line-to-Line (LL), and Three-Phase-to-Ground (TPG) are studied.

At time $t = 1.5\ s$, a SLG fault is applied on phase-a of secondary side of the transformer

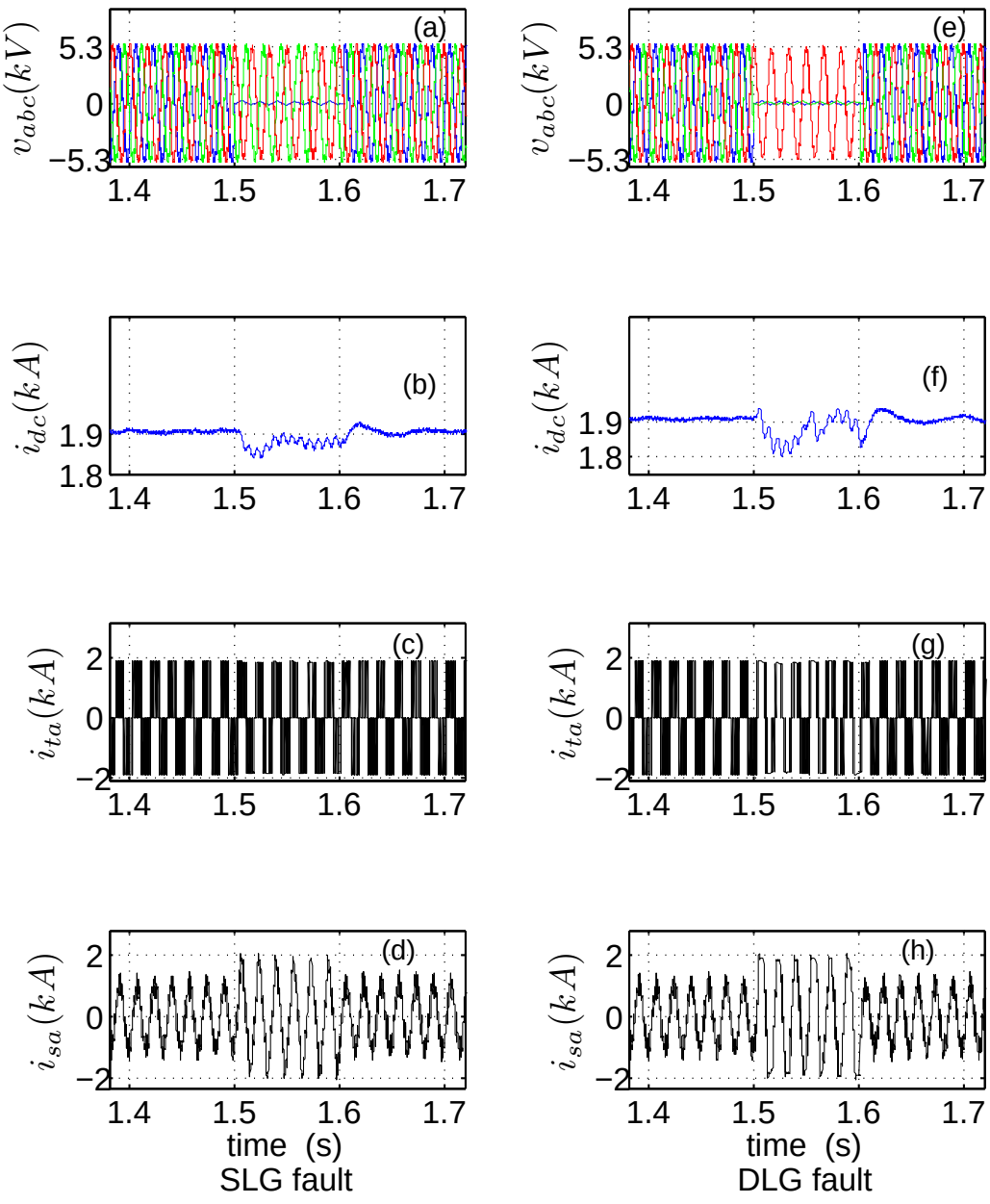

Figure 3.9 CSI-based PV system performance during SLG and DLG faults (v_{abc} = three-phase voltage on the secondary-side of T_r; i_{dc} = DC-side current of the CSI; i_{ta} = phase-a terminal current of CSI; i_{sa} = phase-a current injected to the grid).

T_r. Due to the fault, the voltage v_a drops to zero, as shown in Figure 3.9(a). Application of fault on the AC-side has resulted in oscillations in the DC-side current of the CSI, as shown in Fig. 3.9(b). However, oscillations are damped as soon as the fault is cleared, and the DC-side current controller tracks the reference current in less than 20 ms. Due to this disturbance, the AC terminal current of the CSI, i_{ta}, undergoes over modulation, as shown in Figure 3.9(c). The over modulation results in low order harmonics, and the current i_{sa} injected into the grid is no longer sinusoidal, as shown in Figure 3.9(d). This case study clearly shows the inherent over-current protection built in CSI that limits the currents on both DC and AC sides. Similar responses are observed for DLG, LL, and TPG faults, as illustrated in Figures 3.9(e)-(h), 3.10(a)-(d), and 3.10(e)-(h), respectively. In all types of faults, the magnitude of the sinusoidal current injected into the grid is limited. The reason for penetration of low-order harmonics in the grid during the fault in the presence of filter C_f is that capacitor is designed to filter out the switching harmonics, not low-order harmonics. Harmonic spectrums of the terminal current, i_{ta}, and the current injected into the grid, i_{sa}, before and during a SLG fault are shown in Fig. 3.11. Figures 3.11(a) and (b), respectively, illustrate the harmonic spectrums of i_{ta} and i_{sa} before the fault. It is clear that before the fault there are no major low-order harmonics and the switching harmonics are filtered out in the current i_{sa}. Figure 3.11(c) illustrates the harmonic spectrum of the current i_{ta} during the fault, and the presence of low-order harmonics in this current. The harmonic spectrum of the current i_{sa} during the fault given by Figure 3.11(d) shows that the capacitor has not been able to filter out the low-order harmonics.

Figure 3.12 illustrates the performances of CSI- and VSI-based PV systems during a SLG fault. As mentioned earlier, in VSI-based PV system, the controller on the DC-side is employed to control the DC-side voltage (with AC-side currents limited during faults by limiters implemented in the control system), whereas in CSI-based PV system, the controller's task is to control the DC-side current. One can observe from Figure 3.12(a) that the range of variation in the DC-side current of CSI during fault is tightly limited due

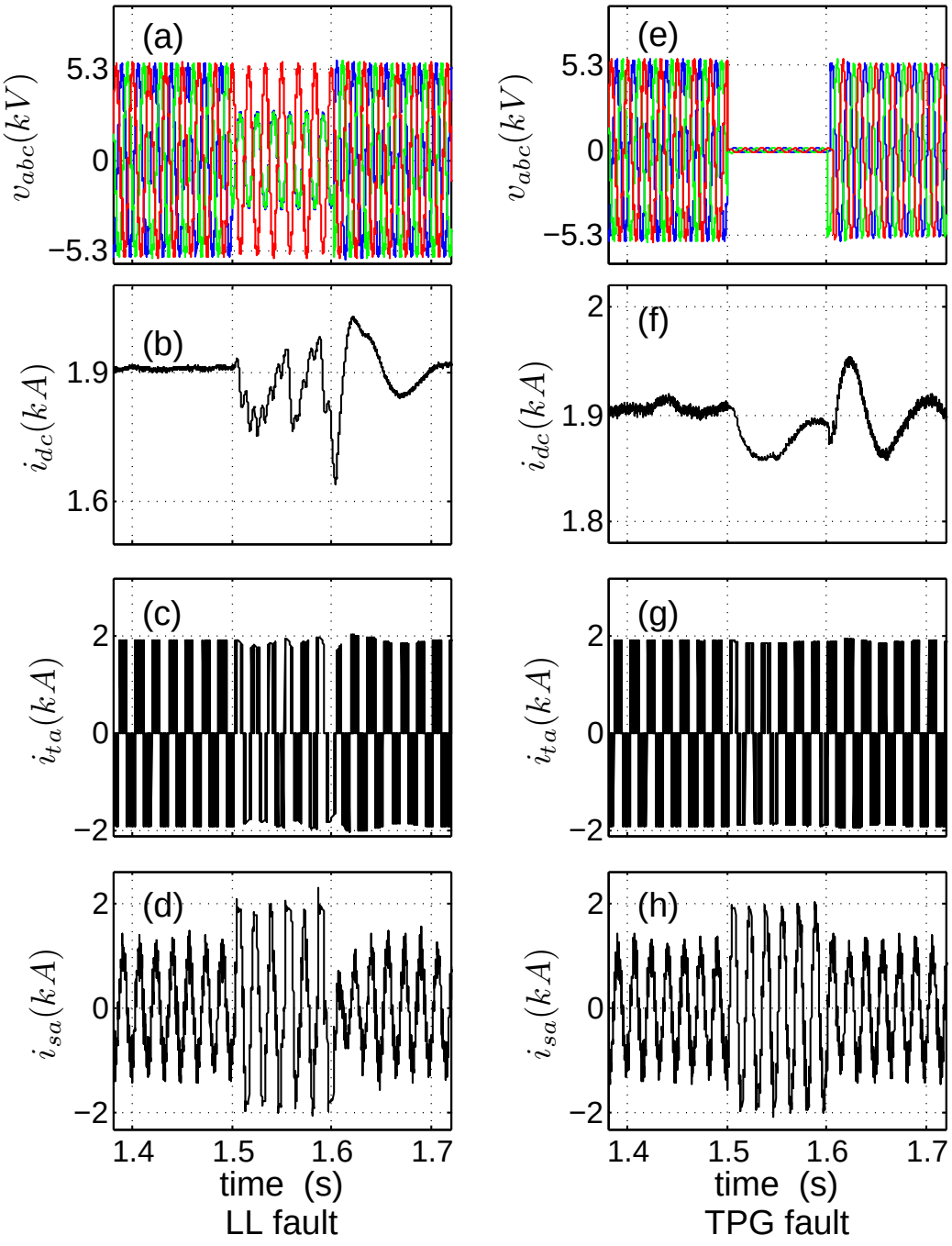

Figure 3.10 CSI-based PV system performance during LL and TPG faults (v_{abc} = three-phase voltage on the secondary-side of T_r; i_{dc} = DC-side current of the CSI; i_{ta} = phase-a terminal current of CSI; i_{sa} = phase-a current injected to the grid).

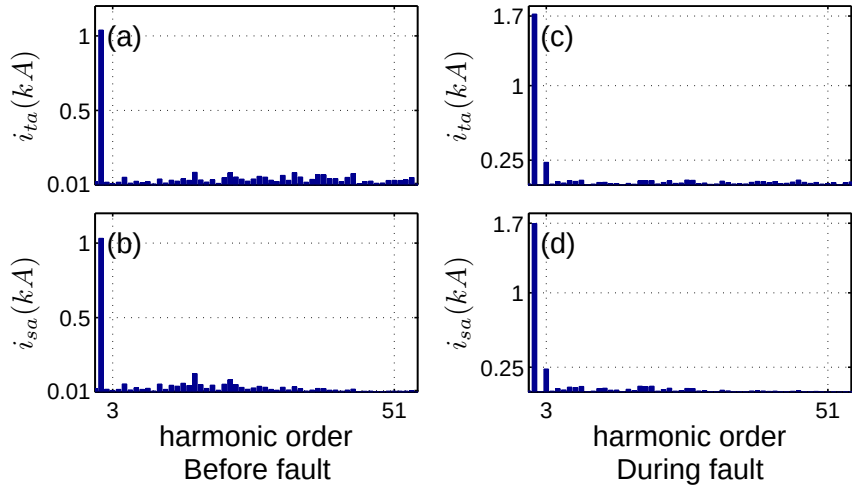

Figure 3.11 Harmonic spectrum of CSI's AC terminal and filtered currents before and during fault.

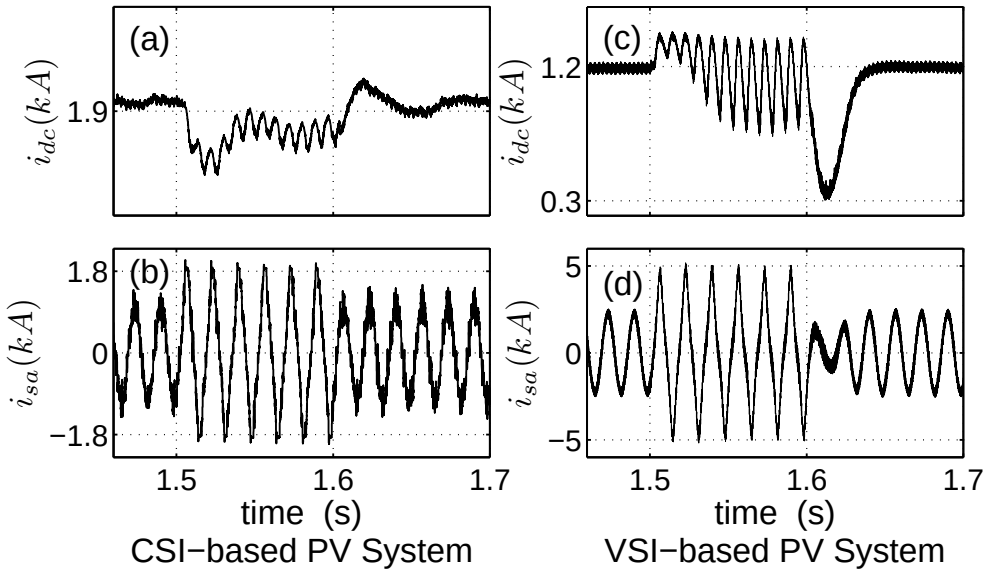

Figure 3.12 CSI- and VSI-based PV systems' performances during a SLG fault.

to the regulatory role of the DC-side current controller. On the contrary, Figure 3.12(c) shows that the DC-side current of VSI is allowed to vary in a wide range. Also, Figure

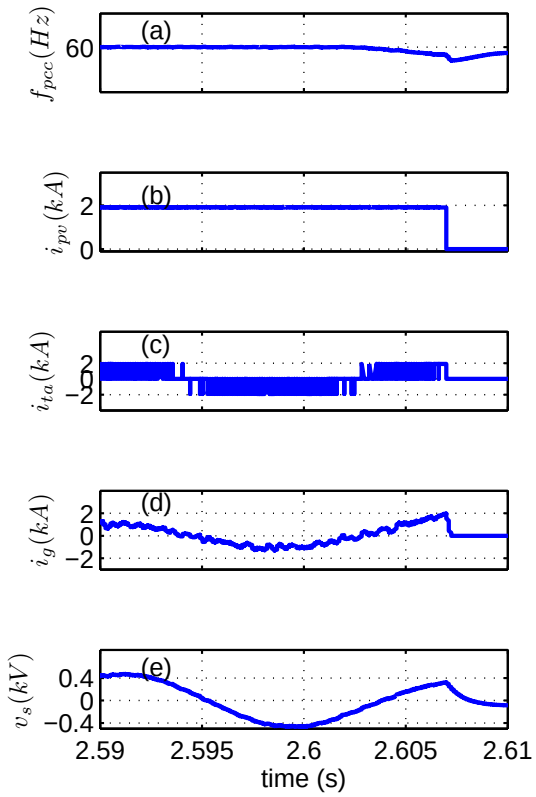

Figure 3.13 Islanding behavior of the CSI-based PV system, (a) Frequency at the PCC; (b) Current of the PV panel; (c) Terminal current of the CSI ; (d) Current injected into the grid; (e) voltage at the PCC.

3.12(b) shows that the amplitude of CSI's AC-side current is limited during fault, whereas the AC-side current of VSI shows a sharp rise in the presence of a current limiter, as illustrated by Figure 3.12(d).

3.6.3 Case study 3: Islanding Behavior of CSI-based PV System

In this part, the operation of the passive OVP/UVP (88 %-112 % and OFP/UFP (59.3 Hz-60.5 Hz) anti-islanding scheme is tested with the CSI-based PV system illustrated in Figure 3.1. At time $t = 2.6\ s$, the breaker on the grid-side, B_r, opens. As a result,

the frequency at the PCC drops below the limit set for OFP/UFP anti-islanding scheme, as shown in Figure 3.13(a), which triggers the anti-islanding logic. The anti-islanding algorithm sends the opening signal to the breaker B_{pv}. As soon as the breaker B_{pv} opens, the inverter unit is instructed to withdraw its operation, which results in the PV panel current, i_{pv}, falling to zero, as shown by Figure 3.13(b); this, in turn, forces the current at the terminal of the inverter unit, i.e., i_{ta}, to fall to zero. A successful anti-islanding operation is confirmed by observing the current and voltage cut-off in Figures **??**(d) and (e).

3.7 Summary

This chapter presented a dynamic model and a control structure for a single-stage, three-phase grid-connected PV system based on current-source inverter. The control structure consists of two current control loops. A Maximum Power Point Tracker (MPPT) provides the reference for the outer DC-side current control loop. The inner current control loop is designed to control the current that is injected into the grid. Using two case studies, i.e., a step change in insolation level and a grid-side fault, a comparative performance evaluation of CSI- and VSI-based PV systems was performed. The fault studies included single-phase-to-ground, two-phase-to-ground, line-to-line, and three-phase-to-ground faults. Through simulation studies, it was shown that the CSI-based PV system, with the designed controller, was able to fulfill all the requirements of a PV system grid interface beside limiting the DC-side and AC-side currents, irrespective of the severity of the fault, unlike a VSI-based PV system.

Chapter 4

A multilevel inverter based on Current Source Inverter (CSI) for three-phase grid-connected Photovoltaic (PV) application

4.1 Introduction

Multilevel CSI is not a new concept. This has been highly investigated in prior research work. However, the majority of prior work focusses on modeling and controller design aspects. Along with the structure and modeling, analysis on operational characteristics is also required. One aspect of operational evaluation is investigation of performance of multilevel inverter when the DC inputs are not equal. This concern has been well addressed for multilevel VSI and solutions have been proposed to avoid unwanted harmonics generated due to dissimilar inputs. However, for multilevel CSI, this has not been reported so far. Issues related to operation under unequal conditions on the DC side and measures to

address them are discussed in this chapter. Along with modeling, operation of a multilevel inverter based on CSI under different weather condition is presented in this chapter. The multilevel inverter developed in this work consists of n units of CSIs and is capable of producing $2n + 1$ levels in the output current. Structure and modeling of an individual CSI unit was thoroughly discussed in Chapter 3. This chapter develops a combined control scheme in stationary frame of reference for controlling the AC-side currents resulting from filtering the multilevel current. The control strategy in combination with the Maximum Power Point Tracking (MPPT) unit enables the multilevel structure to accommodate and successfully operate PV units exposed to equal and unequal insolation levels. It is observed that when PV arrays are exposed to unequal insolation level, low order unwanted harmonics are generated in the sinusoidal current that is injected into the grid. These low order harmonics can have some adverse impact on the loads connected on the AC-side of the inverter. Therefore, the task is to minimize these harmonics and inject a current with low Total Harmonic Distortion (THD) into the grid. Minimization of these harmonics is performed by implementing a modified control strategy in stationary reference frame that corresponds to the harmonic component that needs to be minimized. The modified control strategy operates in coordination with the existing DC-side and AC-side current controllers, and MPPTs. Therefore, real-time suppression of current harmonics can be ensured.

4.2 Structure of the Proposed Three-phase Grid-connected PV system Based on CSI Developed in This Work

Figure 4.1 illustrates the single-line schematic diagram of the proposed three-phase, CSI-based multilevel grid-connected PV system. The multilevel structure consists of n units of

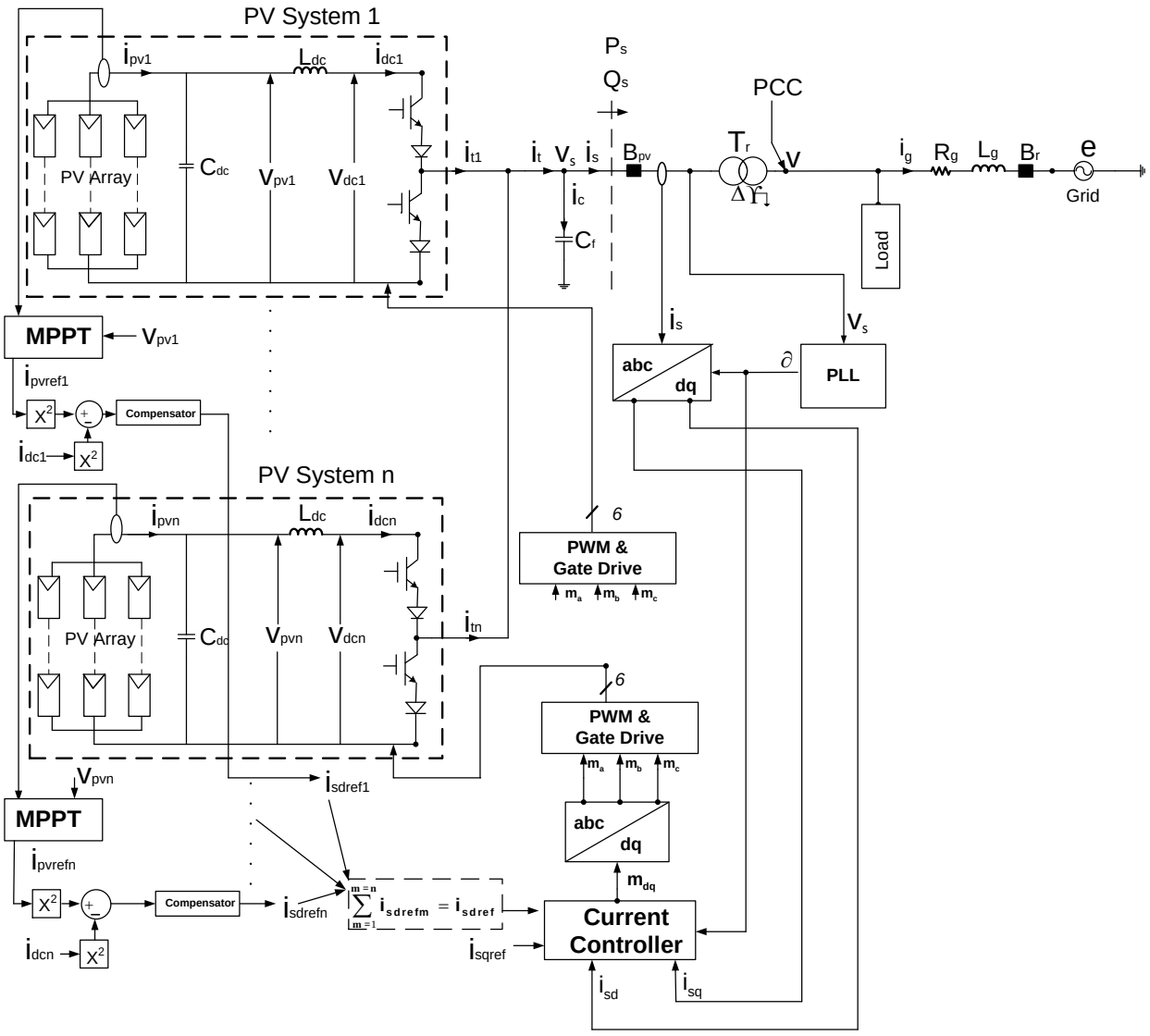

Figure 4.1 Single-line diagram of the proposed three-phase multilevel grid-connected PV system based on CSI.

PV systems. Each PV system has its own power conditioning unit, PV array, Maximum Power Point Tracker (MPPT), and DC-link current controller. On the AC-side, the inverters are connected in parallel, which results in multilevel current, i_t, at the output terminals of the multilevel unit. The multilevel current is filtered by a capacitive filter, C_f. Other

constructional features such as: breakers B_{pv}, B_r, Transformer T_r, and grid parameters were covered in Chapter 3. Dynamics describing the behavior of multilevel inverter are presented in Appendix C

4.3 Controller for Multilevel Inverter Based on CSI

Figure 4.2 presents the closed loop control structure for multilevel CSI presented in Figure 4.1. Current reference corresponding to d-axis of current, i_{sd}, for the AC-side current controller is derived by summing the references produced by individual DC-side current controllers, as represented by equations (4.1) and (4.2). This summation results in reduction in number of controllers, sensors and capacitive filters. References for DC-side current controllers are derived from MPPTs corresponding to the unit. Controllers for DC-side and AC-side have been thoroughly discussed in Chapter 3.

$$i_{sdref} = \sum_{m=1}^{n} i_{sdrefm} \tag{4.1}$$

$$i_{sdrefm} = u_{in} + \eta \left(\frac{P_{pvm}}{\frac{3}{2} v_{sd}} \right) \tag{4.2}$$

4.4 Operation of PV Modules at Maximum Power under Unequal Insolation Level Conditions

One can observe from Figures 4.1 and 4.2 that the same modulating signals, m_a, m_b, and m_c, generated by the combined dq-current controller, are used for all inverter units

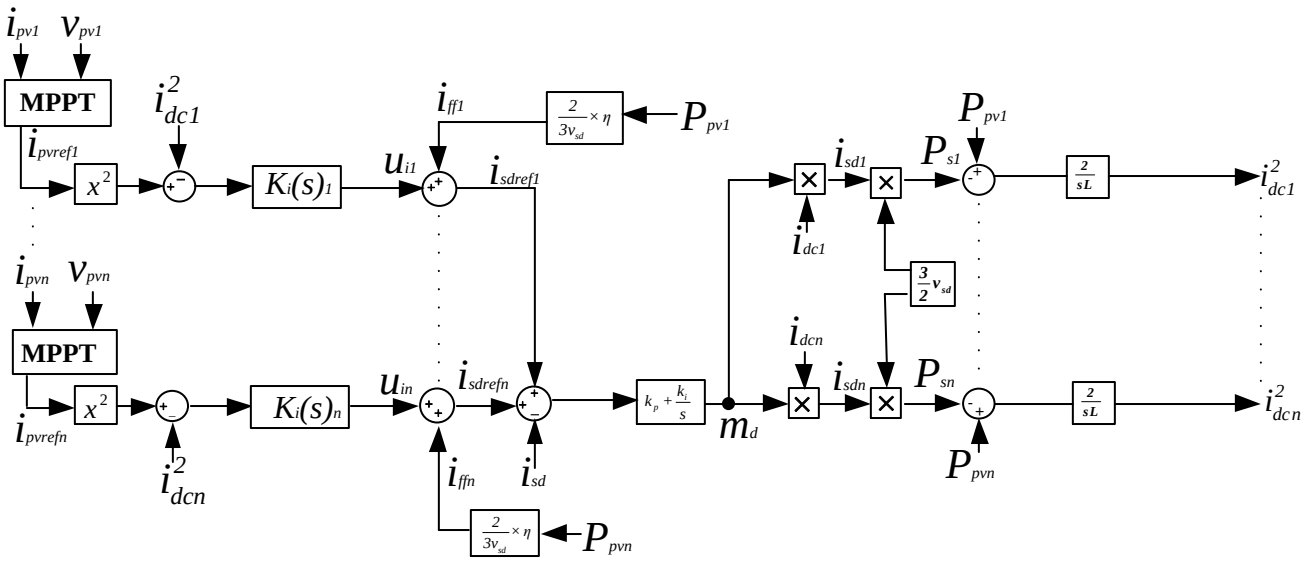

Figure 4.2 Closed loop control structure of the multilevel CSI-based PV System.

in the CSI-based multilevel structure. The objective is to make each PV module operate at its own maximum power point despite the fact that all inverter units are operated by the same modulating signals. The use of the combined controller is preferred to using separate controllers for individual modules since the later adds to the system complexity due to the need for tuning of a number of controllers as well as the possibility of inter-controller interference. In the following, maximum power point operation of the individual PV modules integrated via multilevel CSI inverter structure, under unequal insolation level conditions, is verified.

If a dedicated controller was used to control the ac-side current of each inverter unit based on the reference produced by the maximum power point tracking controller of the corresponding PV module, neglecting the power losses in the inverter modules, one could write:

$$
\begin{aligned}
P_{s1} &= \frac{3}{2} v_{sd} i_{sd1} = \frac{3}{2} v_{sd} i_{sdref1} = P_{dc1,MPP} \approx P_{PV1,MPP} \\
P_{s2} &= \frac{3}{2} v_{sd} i_{sd2} = \frac{3}{2} v_{sd} i_{sdref2} = P_{dc2,MPP} \approx P_{PV2,MPP} \\
&\vdots \\
&\vdots \\
P_{sn} &= \frac{3}{2} v_{sd} i_{sdn} = \frac{3}{2} v_{sd} i_{sdrefn} = P_{dcn,MPP} \approx P_{PVn,MPP}
\end{aligned} \tag{4.3}
$$

Adding both sides of the relations in (4.3), one gets

$$
P_s = \sum_{m=1}^{n} P_{sm} = \frac{3}{2} v_{sd} \sum_{m=1}^{n} i_{sdrefm} = \sum_{m=1}^{n} P_{PVm,MPP} = P_{PV,MPP} \tag{4.4}
$$

The combined controller ensures that

$$
i_{sd} = i_{sdref} = \sum_{m=1}^{n} i_{sdrefm} \tag{4.5}
$$

Therefore,

$$
P_s = \sum_{m=1}^{n} P_{PVm,MPP} = P_{PV,MPP} \tag{4.6}
$$

Since the total active power on the ac-side of the multilevel inverter is equal to the sum of the maximum powers that can be obtained from the individual PV modules, each PV module is forced to operate at its corresponding maximum power point. The proof is as follows:

One can write:

$$
\begin{aligned}
0 &\leq P_{PV1} \leq P_{PV1,MPP} \\
0 &\leq P_{PV2} \leq P_{PV2,MPP} \\
&\vdots \\
0 &\leq P_{PVn} \leq P_{PVn,MPP}
\end{aligned} \tag{4.7}
$$

If

$$P_s = \sum_{m=1}^{n} P_{PVm} = \sum_{m=1}^{n} P_{PVm,MPP} \tag{4.8}$$

then,

$$\begin{aligned} P_{PV1} &= P_{PV1,MPP} \\ P_{PV2} &= P_{PV2,MPP} \\ &\vdots \\ P_{PVn} &= P_{PVn,MPP} \end{aligned}$$

Since, otherwise, if

$$P_{PVm} < P_{PVm,MPP} \tag{4.10}$$

Then,

$$\sum_{m=1}^{n} P_{PVm} < \sum_{m=1}^{n} P_{PVm,MPP} \tag{4.11}$$

In this part, a simulation study is used to support the above analytical results. Table 4.1 illustrates operation of PV modules at the MPP in different scenarios. For this study, three units for multilevel structure are considered. Therefore, there are three study scenarios corresponding to three insolation level conditions. To verify that PV modules in the multilevel structure, under proposed combined control scheme, are operating at the MPP when exposed to unequal insolation levels, data from a CSI-based PV system interfaced to a single PV array is presented in Table 4.1. One can observe from the table that, at a particular insolation level, powers generated by individual modules are very close to each other whether the module is operated as a single unit or a part of the multilevel structure. Furthermore, powers generated by individual modules in the multilevel structure

Table 4.1: Power generated by PV modules in multilevel CSI-based structure at different insolation levels

Power (MW) generated by single unit PV system represented by Figure 3.1			Power (MW) generated by modules in multilevel structure represented by Figure 4.1 Number of modules: $n = 3$ Operating condition: Equal insolation level			Power (MW) generated by modules in multilevel structure represented by Figure 4.1 Number of modules: $n = 3$ Operating condition: Unequal insolation level		
case 1	*case* 2	*case* 3	*case* 1	*case* 2	*case* 3	*case* 1		
S=0.5 kW/m^2	S=0.8 kW/m^2	S=1 kW/m^2	S=0.5 kW/m^2	S=0.8 kW/m^2	S=1 kW/m^2	S=0.5 kW/m^2	S=0.8 kW/m^2	S=1 kW/m^2
P= 0.4355	P= 0.7196	P= 0.9129	$P_1 =$ 0.4359	$P_1 =$ 0.71961	$P_1 =$ 0.9128	$P_1 =$ 0.4354	$P_2 =$ 0.7195	$P_3 =$ 0.91302
			$P_2 =$ 0.43587	$P_2 =$ 0.719551	$P_2 =$ 0.91232			
			$P_3 =$ 0.43588	$P_3 =$ 0.71958	$P_3 =$ 0.91255			

correspond to the maximum power points whether modules are operating under equal or unequal insolation level. For single-unit CSI-based PV system, the system represented by Figure 3.1 is used and for multilevel structure, the system represented by Figure 4.1 is employed. System parameters used for this study are presented in Appendix A.

4.5 Performance Evaluation of Multilevel Inverter

The multilevel structure presented in this chapter is capable of accommodating PV units operating under both equal and unequal insolation level conditions. Therefore, simulation studies under the aforementioned conditions are presented. Before investigating the AC-side characteristics of the system shown in Figure 4.1, the DC-side quantities are examined. Figure 4.3 presents the DC-side characteristics of a single PV system in the multilevel structure. In response to a step change in insolation level shown in Figure 4.3(a), the current delivered by the PV system, i_{pv}, changes as shown in Figure 4.3(b) to realize the new maximum power, while the PV module voltage, v_{pv} remains at a level around 0.6 kV, as shown in Figure 4.3(c). The voltage on the DC-side of the CSI is shown in Figure 4.3(d). The DC-link current controller makes the DC-side current, i_{dc}, assume the value corresponding to the new maximum power point, as shown in Figure 4.3(e).

4.5.1 Operation Under Equal Insolation Levels

The multilevel structure presented in Figure 4.1 produces AC currents of $2n + 1$ levels at the AC terminals for n CSI modules. To illustrate the number of levels in relation to the number of inverter modules, the multilevel structures with even and odd number of inverters are simulated. Figure 4.4 presents the response of the 2-inverter PV system to a step change in the insolation level. The simulation is carried out in PSCAD/EMTDC environment [66]. At $t = 1\ s$, insolation level is changed from 0.4 kW/m^2 to 0.8 kW/m^2,

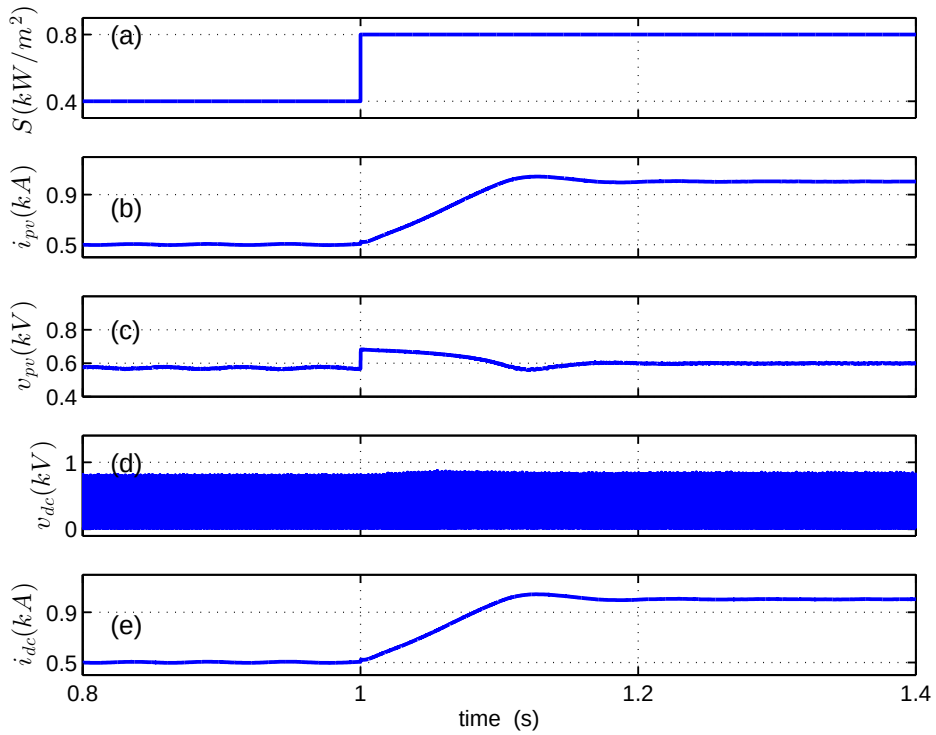

Figure 4.3 DC-side characteristics of the PV system. (a) Insolation level; (b) PV module current; (c) PV module voltage; (d) DC-side voltage of the CSI; and (e) DC-side current of the CSI.

as shown in Figure 4.4(a). Due to the change in insolation level, current references from MPPTs increase, which in turn, increases the multilevel CSI terminal current as illustrated in Figure 4.4(b). Since the number of inverters is 2, the current shown in Figure 4.4(b) has 5 levels. With the change in reference values from MPPTs, the DC-link current controllers cause an increase in the current injected into the grid, as shown in Figure 4.4(c). Currents i_{sdq} represents the d-axis and q-axis components of the current i_{sabc}, i.e., the three-phase sinusoidal current injected into the grid. In order to maintain unity power factor at the Point of Common Coupling (PCC), the q-axis component of the current i_{sq} is regulated to zero by the AC-side current controller, as shown in Figure 4.4(c). Figure 4.4(d) shows

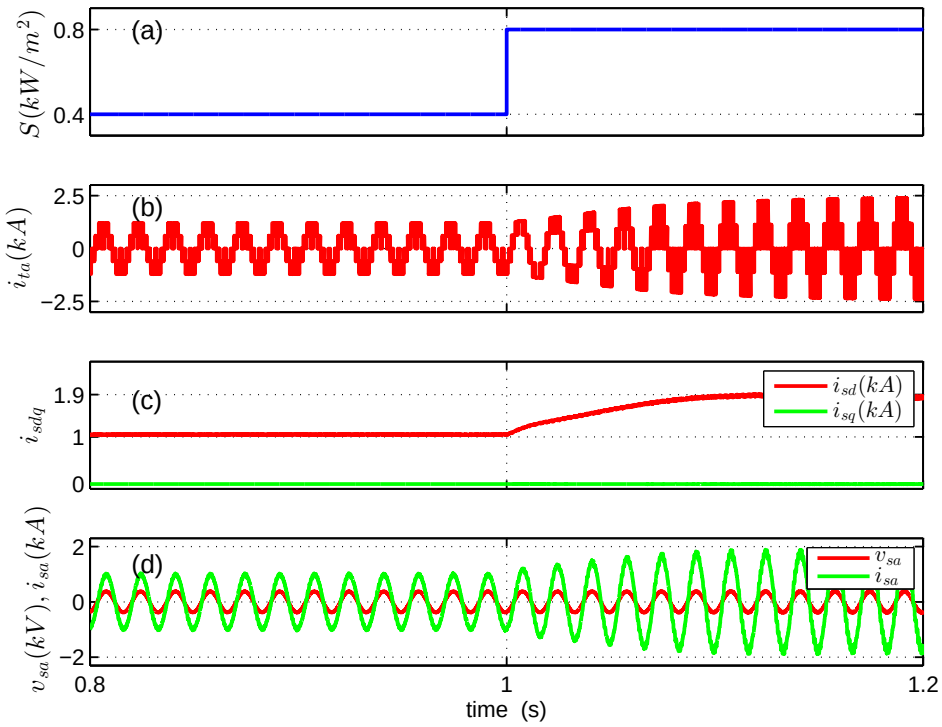

Figure 4.4 Response of the 2-inverter PV system to a step change in insolation level. (a)Insolation level; (b)Multilevel current at the terminal of the multilevel inverter; (c) d- and q- axis currents injected into the grid; (d) Voltage and current at PCC.

that a clean sinusoidal current results from the multilevel CSI-based PV system and unity power factor is maintained at the PCC. In figure 4.5, a 3-inverter PV system is simulated for an insolation level of 0.1 kW/m^2, which results in a 7-level stepped current at the terminal of the multilevel inverter, as shown in Figure 4.5(b).

4.5.2 Operation Under Unequal Insolation Levels

Figure 4.6 illustrates the simulation results for a 2-inverter PV system, where PV arrays are operating under unequal insolation levels. Inverter 1 is under insolation level S_1, whereas inverter 2 is under insolation level S_2. Insolation level S_1 is step-changed from 0.4 kW/m^2

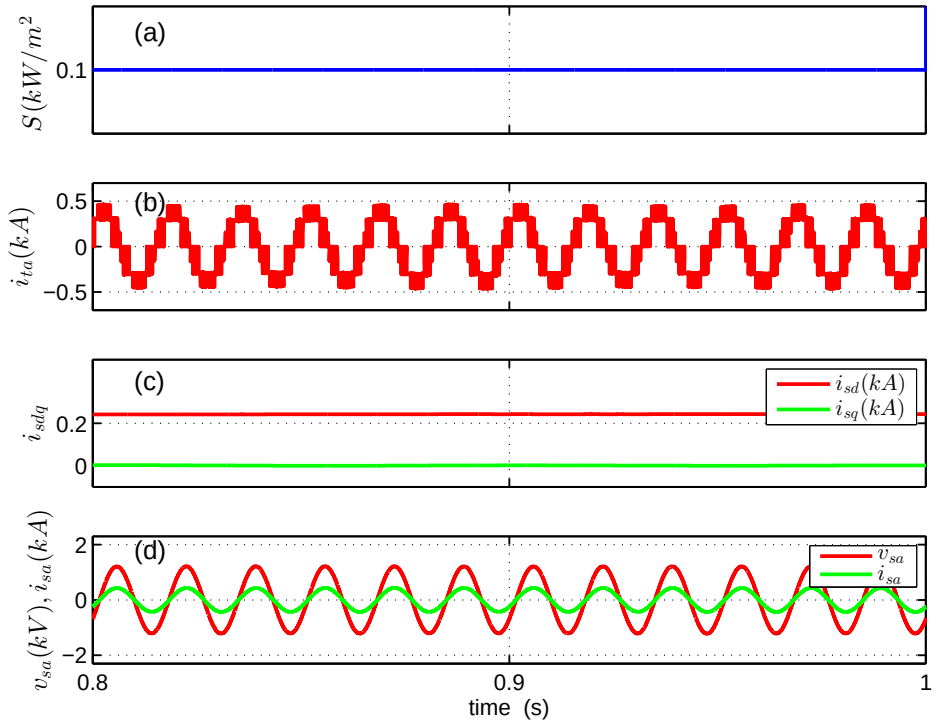

Figure 4.5 Response of the 3-inverter PV system to an insolation level of 0.1 kW/m^2. (a) Insolation level; (b) Multilevel current at the terminal of the multilevel inverter; (c) d- and q- axis currents injected into the grid; (d) Voltage and current at PCC.

to 0.8 kW/m^2 at time $t = 1$ s. At the same instant, insolation level S_2 is step-changed from 0.2 kW/m^2 to 0.5 kW/m^2, as shown in Figure 4.6(a). Due to unequal insolation levels, a non-uniform stepped current waveform is generated at the multilevel inverter terminals, as shown in Figure 4.6(b). The non-uniformity leads to harmonic distortion of the current injected into the grid. To compare the results of operation of multilevel structure under unequal insolation levels to those under equal insolation levels, the harmonic spectrum of simulation results shown in Figure 4.6 are produced in Figure 4.7. Figure 4.7(a) presents the case where the PV systems are operating under equal insolation levels. Operation of the PV systems under unequal insolation levels is illustrated in Figure 4.7(b). The current i_t is the multilevel current at the terminal of the multilevel inverter, and current i_s is the

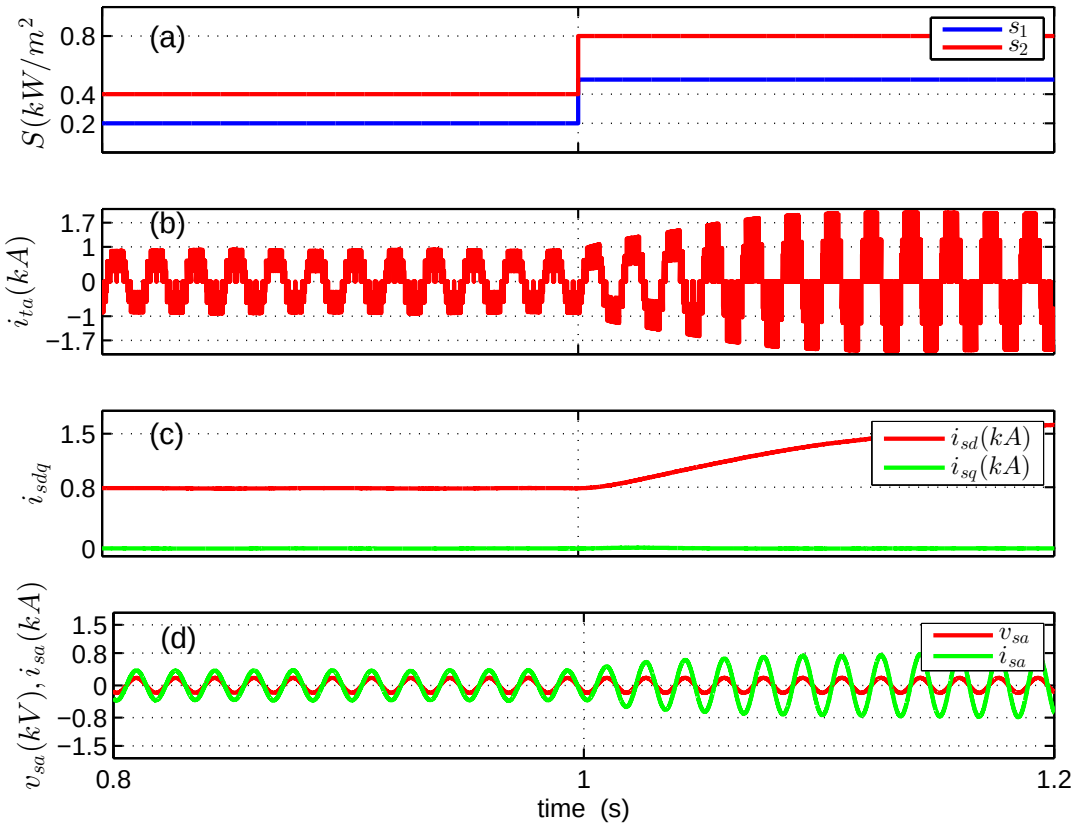

Figure 4.6 Response of the 2-inverter PV system, operating under unequal insolation levels, to step changes in insolation level. (a) Insolation levels; (b) Multilevel current at the terminal of the multilevel inverter; (c) d- and q- axis currents injected into the grid; (d) Voltage and current at PCC.

current injected into the grid. One can observe from Figure 4.7 that the operation of the PV system at a switching frequency of 300 Hz results in a sinusoidal waveform with a Total harmonic Distortion (THD) of 4.9% for the case where the PV units are under equal insolation levels, as shown in Figure 4.7(a). On the contrary, low-order harmonics are generated in the sinusoidal current, i_{sa}, in the case where the PV units are exposed to different insolation levels, as shown in Figure 4.7(b). Low-order harmonics result in a

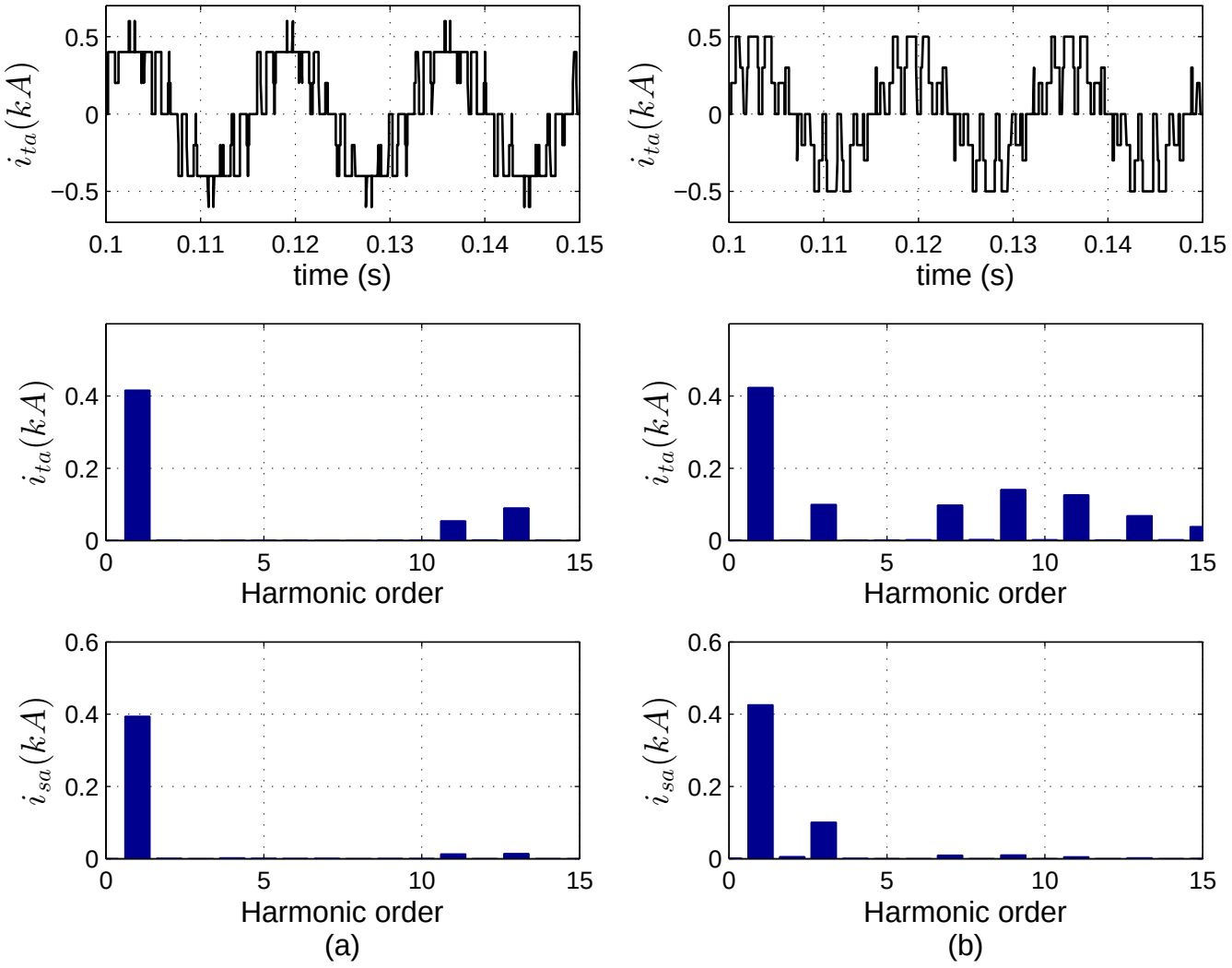

Figure 4.7 Harmonic spectrum of the current injected into the grid by multilevel CSI-based grid-connected PV system operating under (a) equal insolation levels; S_1=S_2=0.4 kW/m^2 (b) unequal insolation levels; $S_1 = 0.5\ kW/m^2$, $S_2 = 0.8\ kW/m^2$.

Total Harmonic Distortion (THD) higher than what is permitted by the IEEE standard 519-1992 [67]. To reduce harmonics in the current that is injected into the grid, the harmonics for multilevel inverter have been investigated in prior research work. A survey on different techniques is presented in the subsequent section. In the later part of Section

4.6, a modified control strategy including harmonic elimination is proposed for the system presented in Figure 4.8 in stationary reference frame.

4.6 Modified Control Strategy to Eliminate Low-order Harmonics when Modules are Under Unequal Insolation Levels

The key criterion in successful implementation of a multilevel inverter is maintaining the Total harmonic Distortion (THD) of the output waveforms within the acceptable limits. Selective Harmonic Elimination (SHE) pulse width modulation has been extensively studied in order to achieve low THD for a multilevel inverter operating under unequal DC-side conditions [68]. Even though SHE is capable of eliminating unwanted harmonics effectively, the main challenge associated with SHE-PWM technique is to obtain an analytical solution for the system of nonlinear equations that contain trigonometric terms; one difficulty is that these types of equations provide multiple sets of solution. The above issues have been reported in the literature. Several algorithms have been proposed concerning the methods of solving the resultant nonlinear transcendental equations, which describe the SHE-PWM problem [69, 70, 71, 72, 73, 74, 75]. Moreover, the inclusion of variable DC-side sources, such as PV panels, adds to the degree of complexity of the problem. This has led to development of different modulation techniques. Reference [75] proposes a new triangular carrier-based phase-shifted suboptimal PWM (PS-SUB-PWM) for cascaded multilevel inverter. In this modulation technique, the modulation waveform is modified by adding the unwanted low-order harmonics such as 3^{rd}, 6^{th}, or 9^{th} harmonics. However, the method proposed is not verified for multilevel inverters employing PV panels as the input source. A real-time selective harmonic minimization technique for a multilevel inverter connected with PV panels is proposed in [76]. In the method proposed in [76], the conventional approach is replaced

by an Artificial Neural Network (ANN), which if well-trained, can produce accurate solutions. Moreover, the method in [76] is verified for unequal DC-inputs. However, the solution obtained in [76] cannot eliminate the harmonics completely; it can reduce them only, and in some cases, the harmonics are not reduced enough to fall within the acceptable limits. Therefore, for successful operation of multilevel inverter, it is important to ensure that the unwanted harmonics are eliminated completely, or reduced to the extent that the standards are complied with. To reduce the complications of SHE, reference [77] proposes a modulation technique based on harmonic elimination. In the method proposed in [77], the triangular carrier is modified, unlike the modulating waveform in [75], to eliminate harmonics. However, the method proposed in [77] is verified only for uniform DC-side sources for multilevel inverter. Besides effective modulation techniques, other approaches such as design of an efficient filter have also been adopted to eliminate harmonics in multilevel inverters. Reference [78] discusses a modified $R-L-C$ filter design to eliminate harmonics, but for particular switching harmonics. In some cases, the usual star-connected capacitive filter can be replaced by a delta-connected filter capacitor to reduce the cut-off frequency; this leads to more effective elimination of low-order harmonics. This option is limited by the operating switching frequency. Therefore, to overcome the widely-discussed issue of eliminating low-order harmonics for a multilevel inverter operating under unequal DC-side conditions, a modified current control strategy is presented in this section. In the modified control strategy, the harmonic components are extracted and regulated to a desired value in dq-control frame. The control strategy adopted in this work ensures that the target harmonic component is attenuated to the desired level or completely eliminated.

Figure 4.8 illustrates the proposed control strategy to eliminate low-order harmonics. The proposed approach is implemented to eliminate the 3^{rd} harmonic in the AC-side current that is generated due to unequal insolation levels received by the PV arrays. The harmonic currents are extracted and transformed into their corresponding dq-frame using the reference angle processed by a dedicated PLL. The d-axis and q-axis components of the

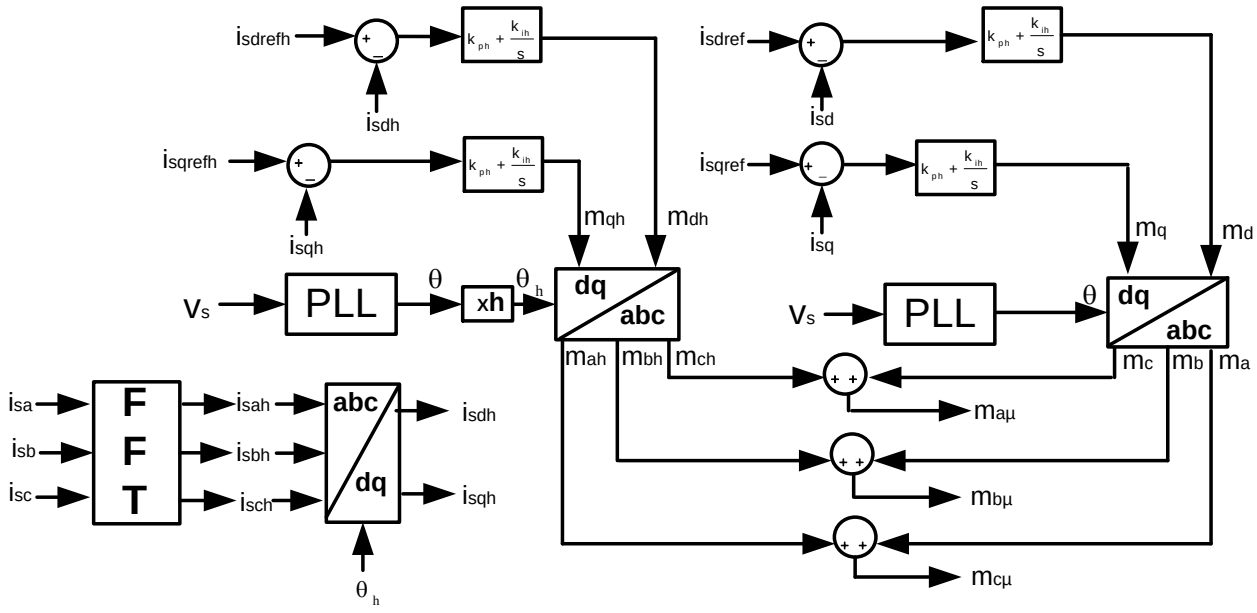

Figure 4.8 Modified control structure to eliminate harmonics.

harmonic current are processed by the controller to generate the corresponding modulating signals. Therefore, the new modulating signal becomes.

$$m_{abc\mu} = m_{abch} + m_{abc} \tag{4.12}$$

where $ma_{abc\mu}$ represents the newly-generated modulating signals, containing the old control signals m_{abc} and the control signal for harmonic elimination ma_{abch}. With the implementation of the proposed control structure, the harmonic results for two the cases are presented in Figure 4.9.

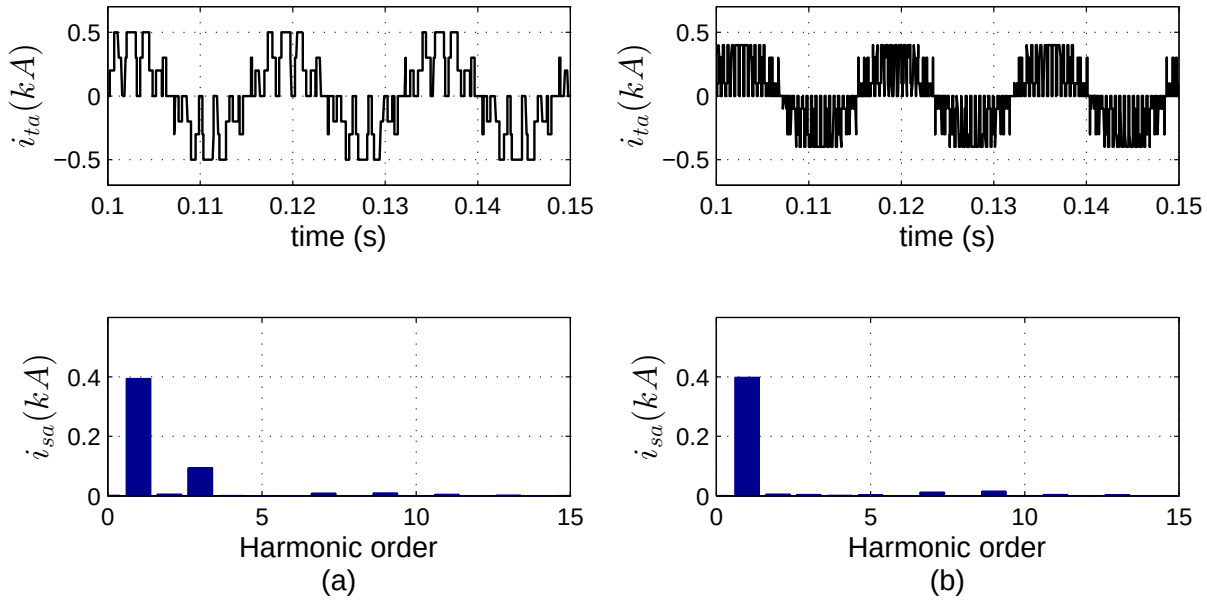

Figure 4.9 Harmonic spectrum of the current injected into the grid by multilevel CSI-based grid-connected PV system operating under (a) without harmonic elimination THD=22.8 % (b) with harmonic elimination, THD=5.008 %.

4.7 Summary

This chapter presented the structure of the power circuit and control system for a CSI-based multilevel inverter system for three-phase, grid-connected PV applications. The proposed structure differs from those proposed earlier by other researchers in terms of the control structure and use of independent DC current sources. Each inverter unit has an independent DC-side current controller governed by the corresponding MPP tracker. Independent operation of PV inverter modules allows for accommodation of PV arrays under different insolation levels that can be located in different locations in a PV field. The DC-link current controller employs a feed-forward control strategy to remove the nonlinearity caused by PV array model. Each DC-link current controller contributes to

Table 4.2: Comparison of Switching Frequency and Filter Size of Single-unit and Multilevel CSI

Parameters	Single unit	Multilevel($n = 3$)
Filter Capacitor, C_f (μF)	300	300
Switching Frequency, f_s (Hz)	> 3000	300

the generation of the reference signal for the AC-side current controller. In this chapter, simulation results for PV systems operating under both equal and unequal insolation levels were presented. On the AC-side of the inverter, a combined current control in dq-frame is implemented. The current controller ensures that the PV system is operating at unity power factor, which is shown by simulation results. Moreover, high quality waveforms are generated at a low switching frequency and with inexpensive capacitive filter common to all modules, when the PV arrays are exposed to equal irradiation level. Table 4.2 summarizes the relative sizes of capacitive filters and switching frequencies for multilevel structure and single-unit CSI. Though operation of multilevel structure is satisfactory under equal insolation level, the quality of current waveform deteriorates when the PV arrays are working under unequal irradiation levels. To eliminate the low order harmonics due to unequal insolation levels, a harmonic compensation control strategy is proposed in this work. With the operation of the harmonic compensation control strategy, the PV system is able to inject clean current into the grid. In addition, the proposed structure avoids use of individual current sensors at the AC outputs of all modules. To verify the viability of the multilevel inverter unit during fault on the grid-side, anti-islanding behavior is examined in the next chapter.

Chapter 5

Anti-Islanding behavior of a multilevel Inverter

5.1 Introduction

For safe operation of Distributed Generation (DG) systems, islanding protection is mandated by the IEEE standards. To ensure that the DG avoids islanding during a fault on the grid-side, various anti-islanding algorithms have been investigated for single-unit grid connected inverter systems in the past. However, research is not rich when it comes to investigation of performance of anti-islanding algorithms for a multi-unit inverter system. This chapter studies the anti-islanding behavior of the system developed in Chapter 4 for different operating conditions. The anti-islanding scheme adopted for this work is the very commonly and widely used OVP/UVP (Over Voltage Protection/Under Voltage Protection) and OFP/UFP (Over frequency Protection/Under Frequency Protection) anti-islanding scheme.

This chapter is organized as follows. A literature survey on anti-islanding behavior of inverters is presented in section 5.2. Anti-islanding testing conditions and behavior of

multilevel inverter are discussed in sections 5.3 and 5.4, respectively. Under the testing conditions described, simulation results for anti-islanding behavior of multilevel inverter are obtained and presented in Section 5.5. Finally a summary is presented in Section 5.6.

5.2 Anti-Islanding Studies

Islanding protection is a vital function for grid-connected inverters in DG application. Islanding occurs when a part of distribution system is electrically isolated from the utility grid, but still continues to be energized by the DG. Such operation is not considered safe, as it may affect the loads and generators connected to the islanded system, as well as the service personnel who are not aware of the fact that line is activated by a DG source, even though the line breaker is open. Therefore, IEEE standard 1547 recommends a maximum delay of 2-5 seconds for detection of an island [79, 80, 81, 82, 83, 84, 85, 86].

Anti-islanding methods can be categorized as passive and active. Passive methods monitor the voltage at the Point of Common Coupling (PCC). The islanding is avoided by the DG if the voltage magnitude and/or frequency and/or impedance and/or harmonic distortion level at the PCC are beyond the specified range [87, 88, 89, 90, 91, 92, 93, 94, 95]. These methods usually don't have any negative impact on the power quality; however, they have a large Non Detection Zone (NDZ). NDZ is the area in active-reactive power mismatch plane, where islanding of the DG can't be detected. Therefore, a large NDZ is not a desirable feature. On the other hand, active methods deliberately introduce a change or disturbance and monitor the corresponding response. Even though active methods have a very small NDZ, they are expensive to implement and the disturbance they cause for islanding detection has an adverse impact on the power quality. Speed and accuracy of islanding detection is very much dependent on the anti-islanding schemes adopted for a particular DG; however, they are not the only factors to be considered. Recent studies show that control

strategy of the inverter unit, rating of the load, inverter rating, and inverter architecture (single-unit or multi-unit) are other factors that can contribute towards changing the size of NDZ and islanding detection time. Previous work has shown that inverter units in multi-inverter systems, connected at the same Point of Common Coupling (PCC), behave differently if they are built by different manufacturers with different islanding detection schemes [90]. In addition, if the size of the impedances between the inverters is significant, an increase in the Run-On Time (ROT: time between loss of utility and disconnection of inverter) is observed. However, if the interconnecting impedances are very small and the inverter units are identical in a multi-unit inverter system, a decrease in ROT is observed. Reference [90] analyzes the ROT for an anti-islanding method based on Classical Linear Instability Method (CLIM). Islanding detection studies have become an interesting subject among researchers due to increase in the number of renewable energy-based grid-connected systems. As the penetration of PV and other renewable energy systems in distribution circuits continues to grow, concerns from the utility community is also on the rise. The concern is primarily focused on high number of inverters connected to the utility at the PCC. In view of this, [91] investigates the high penetration of single-phase residential PV inverters connected to a distribution transformer. Islanding behavior of parallel inverters is investigated in [96], where the author discusses load-sharing control strategy and active droop positioning for islanded parallel inverters in an AC distribution system. To enrich the research in the field of islanding behavior of multi-inverter system, [97] discusses an effective anti-islanding algorithm with very small NDZ for a three-phase scenario. The anti-islanding scheme proposed in [97] is based on negative sequence disturbance, which results in faster islanding detection for a multi-inverter system.

5.3 Anti-islanding Testing Condition

Standards like UL 1741, IEEE 929 and IEEE 1547 [94] recommend the worst conditions for anti-islanding testing of distributed generations. The condition where the active power delivered by a distributed generation system operating at unity power factor matches the power absorbed by the parallel RLC load, is considered the worst case for islanding detection [98]- [99]. Therefore, the standard testing condition is:

- The power generated by DG should match the RLC load power.
- Resonant frequency of the RLC load is equal to the grid line frequency.
- The quality factor Q_f of the RLC load is set to 2.5. The quality factor is defined as the ratio of the reactive power associated with L or C to the active power consumed by R.

$$R = \frac{v_g^2}{P_s} \tag{5.1}$$

$$L = \frac{v_g^2}{\omega_n \times Q_f \times P_s} \tag{5.2}$$

$$C = \frac{Q_f \times P_s}{\omega_n} \tag{5.3}$$

where R is the effective load resistance in ohms, C the effective load capacitance in Farad, L the effective load inductance in Henry, Q_f the quality factor, ω_n the grid frequency in rad/sec, v_g the grid-voltage, and P_s the delivered PV power.

Similarly, the load parameters for a multi-inverter system with n inverter units can be derived as:

$$R = \frac{v_g^2}{n \times P_s} \tag{5.4}$$

$$L = \frac{v_g^2}{\omega_n \times Q_f \times n \times P_s} \tag{5.5}$$

$$C = \frac{Q_f \times n \times P_s}{\omega_n} \tag{5.6}$$

5.4 Anti-islanding Behavior of a Multilevel Inverter

Figure 5.1 represents the multilevel CSI adopted for the purpose of studying anti-islanding behavior. CSI structure and control algorithms have been discussed thoroughly in Chapters 3 and 4. For safety purpose all grid-connected inverters are required to have over/under voltage and over/under frequency protection systems. When the active and reactive powers absorbed by the load are equal to the generated power by the DG, there is no active/reactive power difference between the DG and the load. Active power and reactive powers of the load in Figure 5.1 are given by:

$$P_{load} = P_s + \Delta P \tag{5.7}$$

$$Q_{load} = Q_s + \Delta Q \tag{5.8}$$

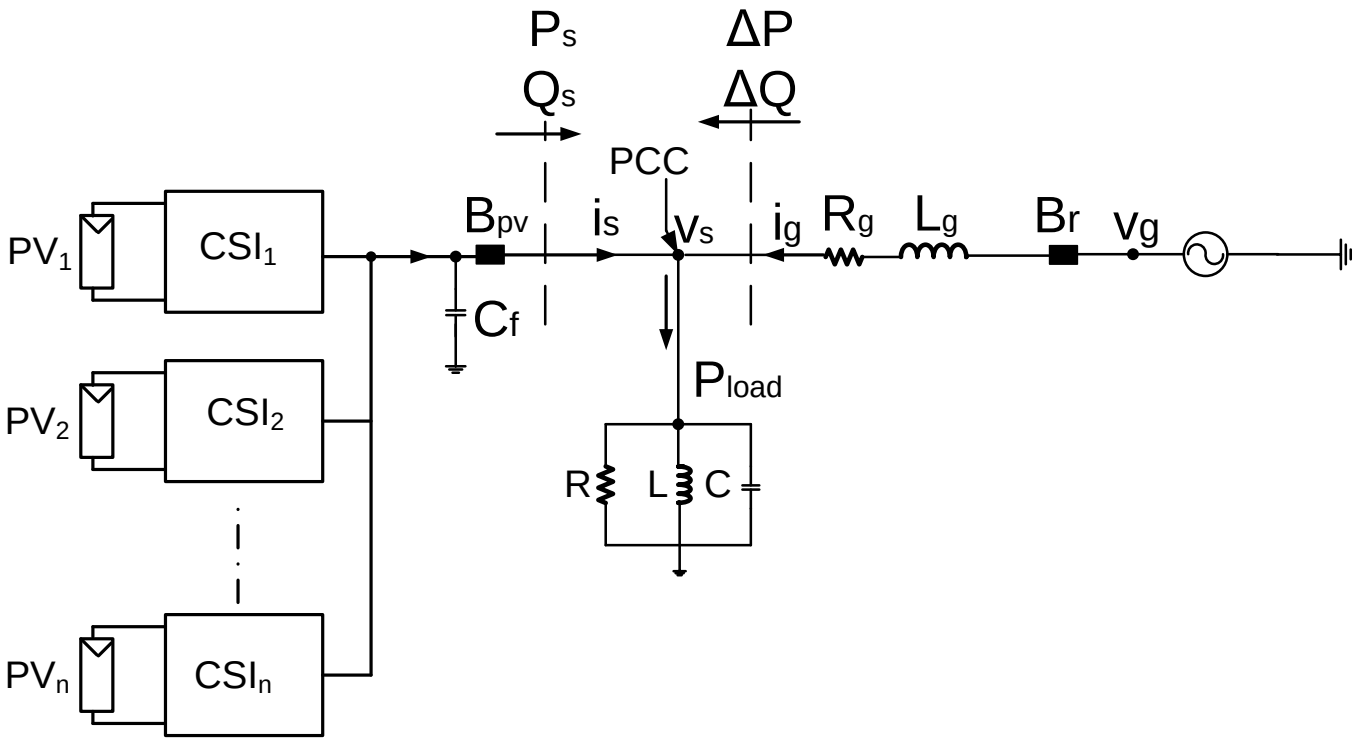

Figure 5.1 Multilevel CSI-based PV system

The behavior of the system after the disconnection from the grid depends on ΔP and ΔQ. If the RLC is chosen such that the resonance frequency of the load is same as the grid frequency, the linear load doesn't absorb any reactive power. Active power is directly proportional to the voltage, v_s in this case. After disconnection, to match the power demand by the load, the voltage v_s changes to a new value, $v_s^{'}$. Relationship between these two parameters is derived below.

The voltage v_s can be expressed as

$$\begin{aligned} v_s &= (RP_{load})^{\frac{1}{2}} \\ &= (R(P_s + \Delta P))^{\frac{1}{2}} \end{aligned} \tag{5.9}$$

After the connection from the grid is lost, voltage v_s changes to $v_s^{'}$ which is equal to

$$v_s^{'} = (RP_s)^{\frac{1}{2}} \tag{5.10}$$

From (5.9) and (5.10), voltages v_s and $v_s^{'}$ can be related as

$$\begin{aligned} \frac{v_s^{'}}{v_s} &= \left(\frac{P_s}{P_s + \Delta P}\right)^{\frac{1}{2}} \\ &= \left(\frac{P_s}{P_{load}}\right)^{\frac{1}{2}} \end{aligned}$$

For a multilevel inverter there are n units, and the load rating is increased by n times. If all the units are rated at Power, P_s, then (5.11) becomes

$$\frac{v_s^{'}}{v_s} = \left(\frac{nP_s}{nP_{load}}\right)^{\frac{1}{2}} = \left(\frac{P_s}{P_{load}}\right)^{\frac{1}{2}} \tag{5.12}$$

From Equations (5.11) and (5.12), one can observe that a multilevel inverter composed of n units operating at the same power level results in the same deviation in the voltage as a single inverter. For the same load, if the units of multi-unit inverter are operating at different power levels, the ratio of the voltages, after the grid is disconnected, $v_s^{'}$, to the voltage before grid disconnection,v_s, is

$$\frac{v_s^{'}}{v_s} = \left(\frac{P_s + P_{s2} + P_{s3} + P_{s4}..... + P_{sn}}{nP_{Load}}\right)^{\frac{1}{2}} \tag{5.13}$$

When P_{s2},P_{s3},$P_{s4}\cdots$>P$_s$, (5.13) can be expressed as

$$\frac{v_s^{'}}{v_s} = \left(\frac{P_s}{nP_{Load}} + \frac{P_s + \Delta P_2}{nP_{Load}} + \frac{P_s + \Delta P_3}{nP_{Load}} + \frac{P_s + \Delta P_4}{nP_{Load}} + ...\frac{P_s + \Delta P_n}{nP_{Load}}\right)^{\frac{1}{2}}$$
$$= \left(\frac{P_s}{P_{Load}} + \frac{\Delta P_2 + \Delta P_3 + ...\Delta P_n}{nP_{Load}}\right)^{\frac{1}{2}} \tag{5.14}$$

By comparing (5.11) and (5.14), one can observe that voltage deviation for the case where the unit are operating at different power levels is more than the case where the units are operating at equal power level. Therefore, one can write,

$$\Delta v_{s(\texttt{unequal unit})} > \Delta v_{s(\texttt{equal unit})} \tag{5.15}$$

When the change in voltage is larger, islanding detection algorithm can work more efficiently and detection can be faster. Such a scenario can be created for the multilevel inverter presented by Figure 4.5 in Chapter 4, where the PV systems are exposed to equal and unequal irradiation level which results in similar and dissimilar power levels for the units in the multilevel structure.

5.5 Simulation results for anti-islanding Behavior of Multilevel Inverter

For the purpose of testing the passive anti-islanding method, the system illustrated in Figure 5.1 is simulated in PSCAD/EMTDC environment. Figure 5.2 shows the islanding behavior of the multi-inverter system based on CSI for PV application. For this case study, two inverter units are considered. The islanding algorithm is implemented in the first inverter. As soon as the breaker B_{pv} is commanded to open when there is any anomaly on the grid-side, a signal is sent to each of the inverter units sharing the same PCC to

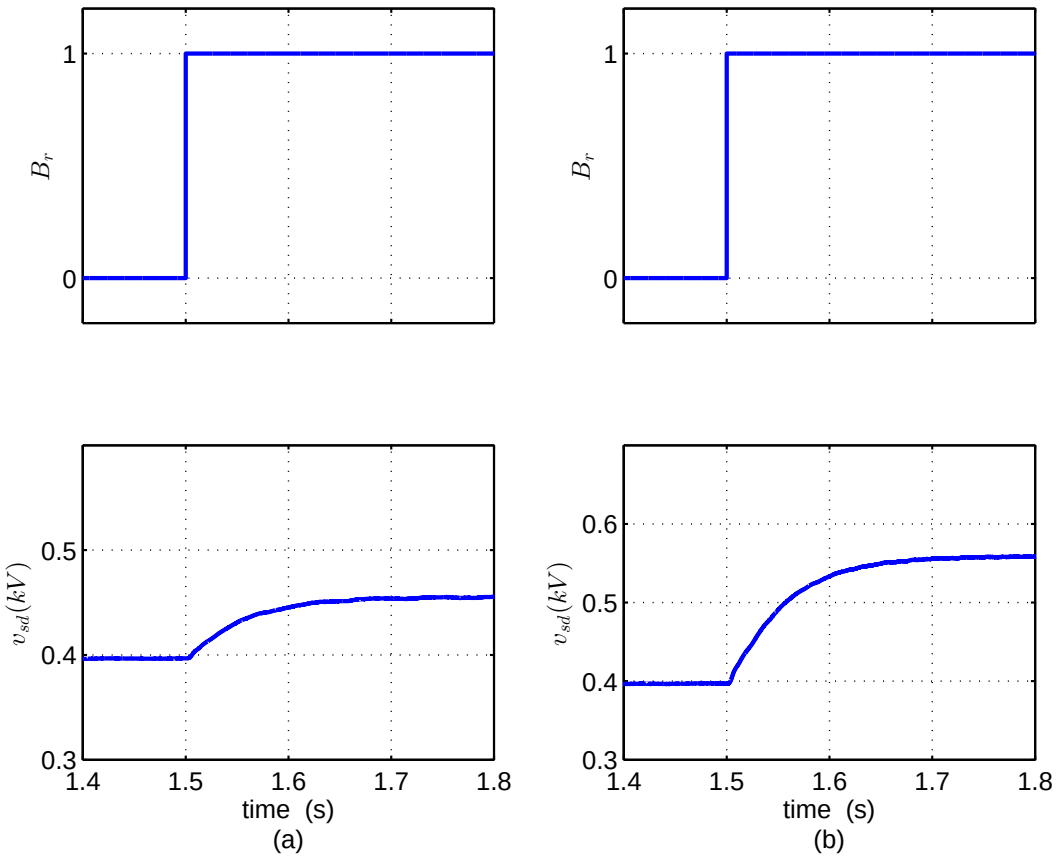

Figure 5.2 Voltage deviations at the load terminals after the grid is disconnected for a 2-module multilevel CSI with modules operating at (a) equal power levels and (b) unequal power levels.

stop their operation. For successful operation of OVP/UVP islanding detection scheme, the voltage at the load terminal, i.e. v_s, should deviate enough from the nominal value ($v_s > 112\%$) for anti-islanding algorithm to operate. To illustrate the impact of weather condition on the detection of islanding as soon as the grid breaker opens, the multilevel system is simulated for two cases. In Figure 5.2(a), two inverter units are exposed to equal irradiation level of 0.2 kW/m^2 and in Figure 5.2(b), inverter 1 is operating at an insolation level of 0.2 kW/m^2 whereas inverter 2 is at 0.5 kW/m^2. From Figure 5.2(b), it is clearly

seen that the multilevel inverter system with PV units operating under unequal insolation levels produces sufficient voltage deviation to trigger the anti-islanding algorithm as soon as the breaker B_r opens, whereas for PV units exposed to equal irradiation levels, the voltage deviation is not sufficient to be detected, as illustrated by Figure 5.2(a). For the purpose of clarity, in place of sinusoidal voltage the d-axis of voltage v_s, i.e., v_{sd} is shown in Figure 5.2. This implies that in the case where the units in a multi inverter system are operating at different power levels, non-detection zone (NDZ) is smaller than when the units are operating under equal power conditions.

5.6 Summary

Passive anti-islanding scheme, composed of OVP/UVP and OFP/UFP protection systems, was tested with a grid-connected CSI-based multi-inverter system. It was shown through analysis and simulation that when the inverter units are operating at equal power levels in the multilevel inverter system, the resulting voltage deviation at the load terminals upon grid disconnection is the same as that for the single-unit system. However, when the inverter units are operating at different power levels, the voltage deviation is larger and islanding detection is faster and the non-detection zone is smaller. Having unequal power levels for the units in a multi inverter PV system is a very common case.

Chapter 6

Eigenvalue analysis of a three-phase grid-connected CSI-based PV system

6.1 Introduction

Simulation results of a three-phase CSI-based grid-connected PV system under different operating conditions were presented and discussed in Chapter 3. Chapter 4 discussed the operation of a CSI multilevel structure in different scenarios. The studies carried out in the previous chapters were mainly simulation-based. Simulation studies provide an idea about dynamic behavior of the system. To learn about the sensitivity of different state variables to different system parameters, a systematic approach is necessary. One such systematic approach is Eigenvalue analysis [100]. For determining eigenmodes, a small signal linear model of the system under study is derived in this Chapter. The small signal model developed in this chapter takes into account the insolation level, grid parameters, and both DC- and AC-side control parameters, as the parameters with respect to which sensitivity of state variables are studied.

6.2 Small Signal Linear Model

The model of the PV system developed in Chapter 3 is nonlinear. While nonlinear models are suitable for simulation studies, it cannot be readily understood from nonlinear equations how each dynamic mode is influenced by different parameters. Therefore, it is necessary to linearize the nonlinearity about a steady-state operating point, to obtain a linear model. The derived linear model will be valid only for small perturbations of the system around the operating point.

The small signal linear model of the system under study can be found by perturbing the state variables around an operating point as expressed by equation (6.1).

$$\bar{x} = X + \tilde{x} \tag{6.1}$$

In 6.1, X and $\tilde{x}$ denote the state variable value at an operating point and the corresponding small perturbation, respectively.

6.2.1 Linearization

The system employed for deriving the linear model is presented in Figure 6.1. Dynamics of the PV system can be categorized as DC-side and AC-side. Linearization of DC-side of the PV system is performed first, followed by that of the AC-side.

Linearization of the DC-side

The rate of change of the energy stored in the DC-link inductor L_{dc} with respect to time can be expressed as:

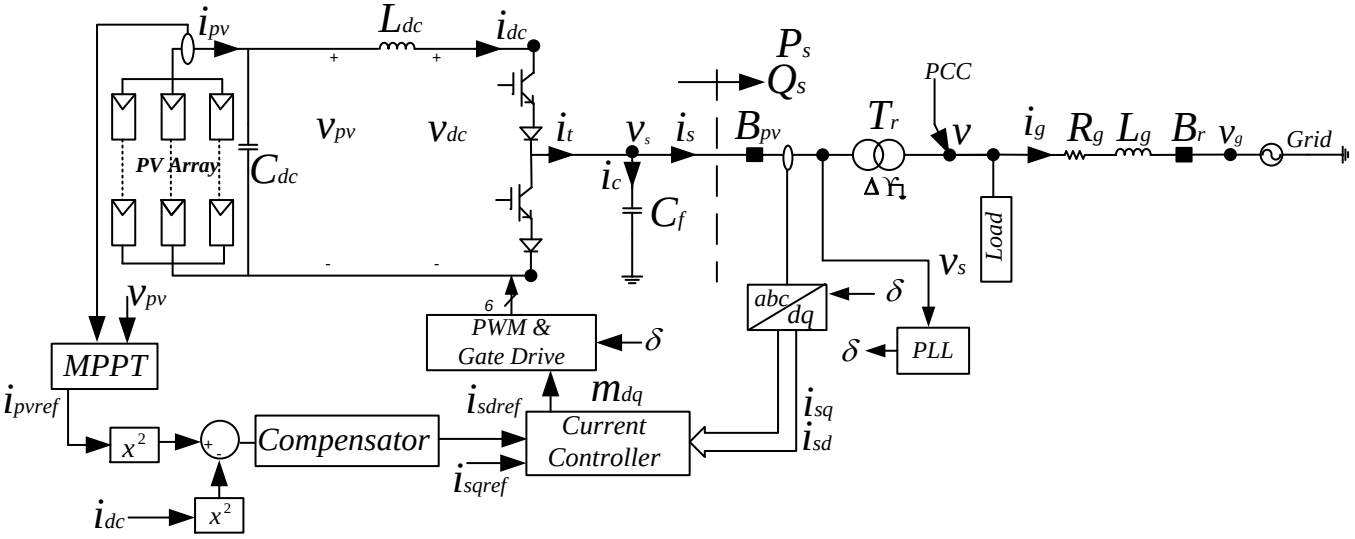

Figure 6.1 Single-line schematic diagram of a three-phase, single-stage, grid-connected PV system based on CSI.

$$\frac{1}{2}L_{dc}\frac{di_{dc}^2}{dt} = \underbrace{i_{pv}v_{pv}}_{P_{pv}} - R_{dc}i_{dc}^2 - \underbrace{\frac{3}{2}\left(v_{sd}i_{sd} + v_{sq}i_{sd}\right)}_{P_s} \tag{6.2}$$

In (6.2), R_{dc} is resistance of the inductance L_{dc}. If a small perturbation around steady-state is assumed, then (6.2) becomes

$$\begin{aligned}\frac{1}{2}L_{dc}\frac{d\left(i_{dc0}+\tilde{i}_{dc}\right)^2}{dt} &= \left(i_{pv0}+\tilde{i}_{pv}\right)\left(v_{pv0}+\tilde{v}_{pv}\right) - R_{dc}\left(i_{dc0}+\tilde{i}_{dc}\right)^2 \\ &-\frac{3}{2}\left[\left(v_{sd0}+\tilde{v}_{sd}\right)\left(i_{sd0}+\tilde{i}_{sd}\right) + \left(v_{sq0}+\tilde{v}_{sq}\right)\left(i_{sq0}+\tilde{i}_{sq}\right)\right]\end{aligned} \tag{6.3}$$

In (6.3), the currents and voltages with a subscript including 0 are steady-state values. After mathematical manipulations, (6.3) can be broken into two equations, one for the system at steady-state and the other one for the perturbed system. Neglecting the terms

that contain multiplication of two perturbed quantities in the perturbed system equation, one obtains

$$\frac{d\left(\tilde{i}_{dc}\right)}{dt} = \frac{1}{i_{dc0}L_{dc}}\left(i_{pv0}\tilde{v}_{pv} + v_{pv0}\tilde{i}_{pv} - 2R_{dc}i_{dc0}\tilde{i}_{dc} - \frac{3}{2}v_{sd0}\tilde{i}_{sd} - \frac{3}{2}i_{sd0}\tilde{v}_{sd} - \frac{3}{2}v_{sq0}\tilde{i}_{sq} - \frac{3}{2}i_{sq0}\tilde{v}_{sq}\right) \tag{6.4}$$

From Figure 6.1, current i_{pv} can be expressed as

$$i_{pv} = C_{dc}\frac{dv_{pv}}{dt} + i_{dc} \tag{6.5}$$

With a small perturbation, (6.5) becomes,

$$i_{pv0} + \tilde{i}_{pv} = C_{dc}\frac{d\left(v_{pv0} + \tilde{v}_{pv}\right)}{dt} + \left(i_{dc0} + \tilde{i}_{dc}\right) \tag{6.6}$$

Again, (6.6) can be broken into steady-state and the perturbed system equations. Considering the equation for the perturbed system only lead to:

$$\tilde{i}_{pv} = C_{dc}\frac{d\tilde{v}_{pv}}{dt} + \tilde{i}_{dc} \tag{6.7}$$

Equation (6.7) can be further simplified as follows:

$$\frac{d\tilde{v}_{pv}}{dt} = -\frac{1}{C_{dc}}\tilde{i}_{dc} + \frac{1}{C_{dc}}\tilde{i}_{pv} \tag{6.8}$$

Current is dependent on insolation level, number of cells in PV array and voltage, as expressed by (6.9).

$$i_{pv} = n_p i_{scr} S - n_p i_{rs} \left(\exp\left(\frac{q}{kTA} \frac{v_{pv}}{n_s} - 1 \right) \right) \tag{6.9}$$

For simplification, let's rename some parameters in (6.9) as follows. $n_p i_{scr} = \mu_0$, $n_p i_{rs} = \mu_1$, $\frac{q}{kTAn_s} = \mu_2$

Substituting μ_0, μ_1, andμ_2 in (6.9) one gets

$$i_{pv} = \mu_0 S - \mu_1 \left(\exp\left(\mu_2 v_{pv} - 1 \right) \right) \tag{6.10}$$

Considering a small perturbation around the steady state on both sides of (6.10) one obtains

$$i_{pv0} + \tilde{i}_{pv} = \mu_0 \left(S_0 + \tilde{S} \right) - \mu_1 \left(\exp\left(\mu_2 \left(v_{pv0} + \tilde{v}_{pv} \right) - 1 \right) \right) \tag{6.11}$$

Considering the equation for the perturbed system only, the following relation results.

$$\begin{aligned} \tilde{\dot{i}}_{pv} &= \mu_0 \tilde{S} - \mu_1 \mu_2 \tilde{v}_{pv} \exp\left(\mu_2 v_{pv0} \right) \\ &= \mu_0 \tilde{S} - \mu_3 \tilde{v}_{pv} \end{aligned} \tag{6.12}$$

where $\mu_3 = \mu_1 \mu_2 exp(\mu_2 v_{pv0})$

Substituting $\tilde{i}_{pv}$ in (6.4) and (6.8) one gets

$$\begin{aligned} \frac{d\tilde{i}_{dc}}{dt} = \frac{1}{i_{dc0} L_{dc}} \Bigg(& - \left(2 R_{dc} i_{dc0} \right) \tilde{i}_{dc} + \left(i_{pv0} - \mu_3 v_{pv0} \right) \tilde{v}_{pv} - \left(\frac{3}{2} i_{sd0} \right) \tilde{v}_{sd} \\ & - \left(\frac{3}{2} i_{sq0} \right) \tilde{v}_{sq} - \left(\frac{3}{2} v_{sd0} \right) \tilde{\dot{i}}_{sd} - \left(\frac{3}{2} v_{sq0} \right) \tilde{\dot{i}}_{sq} + v_{pv0} \mu_0 \tilde{S} \Bigg) \end{aligned} \tag{6.13}$$

$$\frac{d\tilde{v}_{pv}}{dt} = -\frac{1}{C_{dc}} \tilde{\dot{i}}_{dc} - \frac{\mu_3}{C_{dc}} \tilde{v}_{pv} + \frac{\mu_0}{C_{dc}} \tilde{S} \tag{6.14}$$

Linearization of the AC-side

On the AC-side of the inverter, one can write the following equations in dq-frame.

$$C_f \frac{dv_{sd}}{dt} = i_{td} + \omega C_f v_{sq} - i_{sd} \tag{6.15}$$

$$C_f \frac{dv_{sq}}{dt} = i_{tq} - \omega C_f v_{sd} - i_{sq} \tag{6.16}$$

Currents i_{td} and i_{tq} are functions of modulation indices, as expressed by the following equation

$$i_{td} + j i_{tq} = m_d i_{dc} + j m_q i_{dc} \tag{6.17}$$

Substituting values for i_{td} and i_{tq} from (6.17) in (6.15) and (6.16), one can get

$$\frac{dv_{sd}}{dt} = \frac{1}{C_f} \left[m_d i_{dc} + \omega C_f v_{sq} - i_{sd} \right] \tag{6.18}$$

$$\frac{dv_{sq}}{dt} = \frac{1}{C_f} \left[m_q i_{dc} - \omega C_f v_{sd} - i_{sq} \right] \tag{6.19}$$

Applying small perturbations on both sides of (6.18) and (6.19) and considering the equation for the perturbed system only, one obtains

$$\frac{d\tilde{v}_{sd}}{dt} = \frac{1}{C_f} \left(m_{d0} \tilde{i}_{dc} + i_{dc0} \tilde{m}_d \right) + \omega \tilde{v}_{sq} - \frac{1}{C_f} \tilde{i}_{sd} \tag{6.20}$$

$$\frac{d\tilde{v}_{sq}}{dt} = \frac{1}{C_f}\left(m_{q0}\tilde{i}_{dc} + i_{dc0}\tilde{m}_q\right) - \omega\tilde{v}_{sd} - \frac{1}{C_f}\tilde{i}_{sq} \tag{6.21}$$

The controller for the AC-side current, i_{sd} , is designed based on the following equations. Detailed information on the controller design was provided in Chapter 3.

$$(i_{sdref} - i_{sd})\left(k_p + \frac{k_i}{s}\right) = m_d i_{dc} \tag{6.22}$$

$$\frac{i_{sd}}{i_{sdref}} = \frac{1}{\tau_i s + 1} \tag{6.23}$$

From (6.22) and (6.23), the following equation is obtained.

$$\tau_i k_p \frac{di_{sd}}{dt} + \tau_i k_i i_{sd} = m_d i_{dc} \tag{6.24}$$

Applying small perturbations on both sides of (6.24) and considering the equation for the perturbed system only, the following equation results.

$$\tau_i k_p \frac{d\tilde{i}_{sd}}{dt} + \tau_i k_i \tilde{i}_{sd} = m_{d0}\tilde{i}_{dc} + i_{dc0}\tilde{m}_d \tag{6.25}$$

Substituting for $(m_{d0}\tilde{i}_{dc} + i_{dc0}\tilde{m}_d)$ from (6.25) in (6.20), one gets

$$\frac{d\tilde{v}_{sd}}{dt} = \frac{1}{C_f}\left(\tau_i k_p \frac{d\tilde{i}_{sd}}{dt} + \tau_i k_i \tilde{i}_{sd}\right) + \omega\tilde{v}_{sq} - \frac{1}{C_f}\tilde{i}_{sd} \tag{6.26}$$

Similarly, for voltage $\tilde{v}_{sq}$ the following expression can be derived.

$$\frac{d\tilde{v}_{sq}}{dt} = \frac{1}{C_f}\left(\tau_i k_p \frac{d\tilde{i}_{sq}}{dt} + \tau_i k_i \tilde{i}_{sq}\right) - \omega\tilde{v}_{sd} - \frac{1}{C_f}\tilde{i}_{sq} \tag{6.27}$$

One can observe that equations (6.26) and (6.27) contains the terms $\frac{d\tilde{i}_{sd}}{dt}$ and $\frac{d\tilde{i}_{sq}}{dt}$, respectively. Therefore, the next task is to find expressions for these terms. Equation (6.23) can be written as

$$\frac{di_{sd}}{dt} = -\frac{1}{\tau_i} i_{sd} + \frac{1}{\tau_i} i_{sdref} \tag{6.28}$$

Considering a small perturbation, (6.27) can be rewritten as

$$\frac{d\tilde{i}_{sd}}{dt} = -\frac{1}{\tau_i}\tilde{i}_{sd} + \frac{1}{\tau_i}\tilde{i}_{sdref} \tag{6.29}$$

Similarly for current i_{sq}, the expression for the perturbed system is

$$\frac{d\tilde{i}_{sq}}{dt} = -\frac{1}{\tau_i}\tilde{i}_{sq} + \frac{1}{\tau_i}\tilde{i}_{sqref} \tag{6.30}$$

As mentioned in Chapter 3, in order to maintain unity power factor at the PCC, the reference current for i_{sq}, i.e., $_{isqref}$ is set to zero; therefore, (6.30) becomes

$$\frac{d\tilde{i}_{sq}}{dt} = -\frac{1}{\tau_i}\tilde{i}_{sq} \tag{6.31}$$

However, current i_{sdref} is a combination of the feed-forward term and the controller parameter, as expressed by the following equation.

$$i_{sdref} = H_{dc}\left(i_{dcref}^2 - i_{dc}^2\right) + \frac{v_{pv} i_{pv}}{\frac{3}{2} v_{sd}} \tag{6.32}$$

The expression for the perturbed system after considering small perturbations on both sides of (6.32) is

$$\tilde{i}_{sdref} = H_{dc}\left(2i_{dcref}^2 - 2i_{dc0}\tilde{i}_{dc}\right) + \frac{2}{3v_{sd0}}\left(i_{pv0}\tilde{v}_{pv} + v_{pv0}\tilde{i}_{pv}\right)\left(1 - \frac{\tilde{v}_{sd}}{v_{sd0}}\right) \tag{6.33}$$

Equation (6.33) can be is further simplified to

$$\tilde{i}_{sdref} = H_{dc}\left(2i_{dcref}^2 - 2i_{dc0}\tilde{i}_{dc}\right) + \frac{i_{pv0}}{\frac{3}{2}v_{sd0}}\tilde{v}_{pv} + \frac{v_{pv0}}{\frac{3}{2}v_{sd0}}\tilde{i}_{pv} + \frac{i_{pv0}v_{pv0}}{\frac{3}{2}v_{sd0}^2}\tilde{v}_{sd} \tag{6.34}$$

In (6.34), H_{dc} is a second order transfer function expressed by the following equation

$$H_{dc} = \frac{\alpha_1 s + \alpha_2}{s\left(s + \alpha_3\right)} \tag{6.35}$$

Substituting for H_{dc} in (6.35), one can get

$$\tilde{i}_{sdref} = \frac{\alpha_1 s + \alpha_2}{s\left(s + \alpha_3\right)}\left(2i_{dcref}^2 - 2i_{dc0}\tilde{i}_{dc}\right) + \frac{i_{pv0}}{\frac{3}{2}v_{sd0}}\tilde{v}_{pv} + \frac{v_{pv0}}{\frac{3}{2}v_{sd0}}\tilde{i}_{pv} + \frac{i_{pv0}v_{pv0}}{\frac{3}{2}v_{sd0}^2}\tilde{v}_{sd} \tag{6.36}$$

In this way, two new state variables $\tilde{x}_3$ and $\tilde{x}_4$, expressed by (6.37) and (6.38), are introduced.

$$\tilde{x}_3 = \frac{2i_{dcref}^2 - 2i_{dc0}\tilde{i}_{dc}}{s\left(s + \alpha_3\right)} \tag{6.37}$$

$$\tilde{x}_4 = \frac{d\tilde{x}_3}{dt} \tag{6.38}$$

From (6.37) and (6.38), the following equation can be derived.

$$\frac{d\tilde{x}_4}{dt} = -(2i_{dc0})\tilde{i}_{dc} - \alpha_3\tilde{x}_4 + 2i_{dcref}^2 \tag{6.39}$$

Based on (6.37) and (6.38), the expression for given by (6.36) becomes

$$\tilde{i}_{sdref} = \frac{v_{pvo}}{\frac{3}{2}v_{sd0}}\tilde{i}_{pv} + \frac{i_{pvo}}{\frac{3}{2}v_{sd0}}\tilde{v}_{pv} + \frac{v_{pvo}i_{pvo}}{\frac{3}{2}v_{sd0}^2}\tilde{v}_{sd} + \alpha_2\tilde{x}_3 + \alpha_1\tilde{x}_4 \tag{6.40}$$

Substituting for $\tilde{i}_{sdref}$ from (6.40) and $\tilde{i}_{pv}$ from (6.12) in (6.30), the expression for $\frac{d\tilde{i}_{sd}}{dt}$ becomes

$$\frac{d\tilde{i}_{sd}}{dt} = -\frac{1}{\tau_i}\left[\left(\frac{\mu_3 v_{pvo}}{\frac{3}{2}v_{sd0}} + \frac{i_{pvo}}{\frac{3}{2}v_{sd0}}\right)\tilde{v}_{pv} + \frac{v_{pvo}i_{pvo}}{\frac{3}{2}v_{sd0}^2}\tilde{v}_{sd} + \tilde{i}_{sd} + \alpha_2\tilde{x}_3 + \alpha_1\tilde{x}_4 - \frac{\mu_0 v_{pvo}}{\frac{3}{2}v_{sd0}}\tilde{S}\right] \tag{6.41}$$

Substituting for $\frac{d\tilde{i}_{sd}}{dt}$ from (6.41) in (6.26), one gets

$$\begin{aligned}\frac{d\tilde{v}_{sd}}{dt} = \frac{1}{C_f}\left[-k_p\left\{\left(\frac{\mu_3 v_{pvo}}{\frac{3}{2}v_{sd0}} + \frac{i_{pvo}}{\frac{3}{2}v_{sd0}}\right)\tilde{v}_{pv} + \frac{v_{pvo}i_{pvo}}{\frac{3}{2}v_{sd0}^2}\tilde{v}_{sd} + \tilde{i}_{sd} + \alpha_2\tilde{x}_3 + \alpha_1\tilde{x}_4 - \frac{\mu_0 v_{pvo}}{\frac{3}{2}v_{sd0}}\tilde{S}\right\} + \tau_i k_i \tilde{i}_{sd}\right] \\ +\omega\tilde{v}_{sq} - \frac{1}{C_f}\tilde{i}_{sd}\end{aligned} \tag{6.42}$$

Equation (6.42) can be further simplified to

$$\frac{d\tilde{v}_{sd}}{dt} = \frac{k_p v_{pvo}}{\frac{3}{2}C_f v_{sd0}}\tilde{i}_{pv} + \frac{k_p i_{pvo}}{\frac{3}{2}C_f v_{sd0}}\tilde{v}_{pv} + \frac{k_p v_{pvo} i_{pvo}}{\frac{3}{2}C_f v_{sd0}^2}\tilde{v}_{sd} + \omega\tilde{v}_{sq} + \left(\frac{\tau_i k_i}{C_f} - \frac{1}{C_f}\right)\tilde{i}_{sd} + \frac{k_p\alpha_2}{C_f}\tilde{x}_3 + \frac{k_p\alpha_1}{C_f}\tilde{x}_4 \tag{6.43}$$

Substituting for $\frac{d\tilde{i}_{sq}}{dt}$ from (6.30) in (6.27), the expression for $\frac{d\tilde{v}_{sq}}{dt}$ becomes

$$\frac{d\tilde{v}_{sq}}{dt} = -\omega\tilde{v}_{sd} - \left(\frac{\tau_i k_i}{C_f} - \frac{1}{C_f}\right)\tilde{i}_{sq} \tag{6.44}$$

The expressions derived so far are for the quantities on the primary side of the transformer. The dynamics of current that is injected into the grid, i_g can be expressed in dq-frame as:

$$L_g\frac{di_{gd}}{dt} = -R_g i_{gd} + \omega L_g i_{gq} + N v_{sd} - v_g \tag{6.45}$$

$$L_g\frac{di_{gq}}{dt} = -R_g i_{sq} - \omega L_g i_{sd} + N v_{sq} \tag{6.46}$$

where N is turn ratio of transformer T_r and v_g is the grid voltage.

Applying small perturbations on both sides of (6.45) and (6.46), and considering the equations for the perturbed system only, one gets

$$\frac{d\tilde{i}_{gd}}{dt} = -\frac{R_g}{L_g}\tilde{i}_{gd} + \omega\tilde{i}_{gq} + \frac{1}{L_g}N\tilde{v}_{sd} - \frac{1}{L_g}v_g \tag{6.47}$$

$$\frac{d\tilde{i}_{gq}}{dt} = -\omega\tilde{i}_{gd} - \frac{R_g}{L_g}\tilde{i}_{gq} + \frac{1}{L_g}N\tilde{v}_{sq} \tag{6.48}$$

6.3 Linearized Model of CSI-Based PV System

From the mathematical formulations carried out so far, the linearized model for the CSI-based PV system can be expressed as

$$\frac{d\tilde{x}}{dt} = A\tilde{x} + B\tilde{u} \tag{6.49}$$

$$\tilde{x} = \begin{bmatrix} \tilde{i}_{dc} & \tilde{v}_{pv} & \tilde{v}_{sd} & \tilde{v}_{sq} & \tilde{i}_{sd} & \tilde{i}_{sq} & \tilde{x}_3 & \tilde{x}_4 & \tilde{i}_{gd} & \tilde{i}_{gq} \end{bmatrix}^T \tag{6.50}$$

$$\tilde{u} = \begin{bmatrix} \tilde{S} & v_g & \tilde{i}_{dcref} \end{bmatrix}^T \tag{6.51}$$

$$A = \begin{bmatrix} a_{11} & a_{12} & a_{13} & a_{14} & a_{15} & a_{16} & 0 & 0 & 0 & 0 \\ a_{21} & 0 & 0 & 0 & 0 & 0 & 0 & 0 & 0 & \\ 0 & a_{32} & a_{33} & \omega & a_{35} & 0 & a_{37} & a_{38} & 0 & 0 \\ 0 & 0 & -\omega & 0 & 0 & a_{46} & 0 & 0 & 0 & 0 \\ 0 & a_{52} & a_{53} & a_{54} & 0 & 0 & a_{57} & a_{58} & 0 & 0 \\ 0 & 0 & 0 & 0 & 0 & -\frac{1}{\tau_i} & 0 & 0 & 0 & 0 \\ 0 & 0 & 0 & 0 & 0 & 0 & 0 & 1 & 0 & 0 \\ -(2i_{dc0}) & 0 & 0 & 0 & 0 & 0 & 0 & -\alpha_3 & 0 & 0 \\ 0 & 0 & \frac{N}{L_g} & 0 & 0 & 0 & 0 & 0 & -\frac{R_g}{L_g} & \omega \\ 0 & 0 & 0 & \frac{N}{L_g} & 0 & 0 & 0 & 0 & -\omega & -\frac{R_g}{L_g} \end{bmatrix}$$

$$B = \begin{bmatrix} \frac{v_{pv0}\mu_0}{i_{dc0}L_{dc}} & 0 & 0 \\ \frac{\mu_0}{C_{dc}} & 0 & 0 \\ \frac{\mu_0 v_{pvo}k_p}{\frac{3}{2}v_{sd0}C_f} & 0 & 0 \\ 0 & 0 & 0 \\ \frac{\mu_0 v_{pvo}}{\frac{3}{2}v_{sd0}\tau_i} & 0 & 0 \\ 0 & 0 & 0 \\ 0 & 0 & 0 \\ 0 & 0 & \left(2i_{dcref}^2\right) \\ 0 & -\frac{1}{L_g} & 0 \\ 0 & 0 & 0 \end{bmatrix} \tag{6.52}$$

where, $a_{11} = \frac{-(2R_{dc}i_{dc0})}{i_{dc0}L_{dc}}$, $a_{12} = \frac{(i_{pv0}-\mu_3 v_{pv0})}{i_{dc0}L_{dc}}$, $a_{13} = \frac{(i_{pv0}-\mu_3 v_{pv0})}{i_{dc0}L_{dc}}$, $a_{13} = -\frac{\left(\frac{3}{2}i_{sd0}\right)}{i_{dc0}L_{dc}} - \frac{\left(\frac{3}{2}i_{sq0}\right)}{i_{dc0}L_{dc}}$, $a_{14} = -\frac{\left(\frac{3}{2}i_{sq0}\right)}{i_{dc0}L_{dc}}$, $a_{15} = -\frac{\left(\frac{3}{2}v_{sd0}\right)}{i_{dc0}L_{dc}}$, $a_{16} = -\frac{\left(\frac{3}{2}v_{sq0}\right)}{i_{dc0}L_{dc}}$, $a_{21} = -\frac{1}{C_{dc}} - \frac{\mu_3}{C_{dc}}$, $a_{32} = -\frac{k_p}{C_f}\left(\frac{\mu_3 v_{pvo}}{\frac{3}{2}v_{sd0}} + \frac{i_{pvo}}{\frac{3}{2}v_{sd0}}\right)$, $a_{33} = \frac{k_p v_{pvo} i_{pvo}}{\frac{3}{2}C_f v_{sd0}^2}$, $a_{35} = \left(\frac{\tau_i k_i}{C_f} - \frac{1}{C_f}\right)$, $a_{37} = \frac{k_p \alpha_2}{C_f}$, $a_{38} = \frac{k_p \alpha_1}{C_f}$, $a_{46} = \left(\frac{\tau_i k_i}{C_f} - \frac{1}{C_f}\right)$, $a_{52} = -\frac{1}{\tau_i}\left(\frac{\mu_3 v_{pvo}}{\frac{3}{2}v_{sd0}} + \frac{i_{pvo}}{\frac{3}{2}v_{sd0}}\right)$, $a_{53} = -\frac{1}{\tau_i}\frac{v_{pvo}i_{pvo}}{\frac{3}{2}v_{sd0}^2}$, $a_{54} = -\frac{1}{\tau_i}$, $a_{57} = \frac{\alpha_2}{\tau_i}$, $a_{57} = \frac{\alpha_1}{\tau_i}$.

Equations (6.49)-(6.52) represents the linearized model of the system represented by Figure 6.1. The linearized model has 10 state variables. Each eigenvalue of 6.52 corresponds to one of the system's modes. The stability of the system is determined by the eigenvalue of the system as follows [101]:

- If the real parts of all eigenvalues are negative, the system is stable around the equilibrium point;
- If at least one of the eigen values has a positive real part, the system is unstable; and
- If at least one eigenvalue has a zero real part, the system is marginally stable.

Table 6.1: Nominal Values of State Variables

State Variable	Value
v_g	6.6 kV $(L-L\ RMS$
i_{pv0}	1.35 kA at $S = 1\ kW/m^2$
v_{pv0}	0.6 kV
v_{sd0}	0.4 kV
v_{sq0}	0 kV
i_{sd0}	$\frac{P_{pv}}{\frac{3}{2}v_{sd0}}$kA
i_{sq0}	0 kA

To determine the contribution of each variable in a mode and to evaluate the sensitivity of the mode to system parameters, eigenvalue analysis for different modes is carried out in the next section.

6.4 Sensitivity Analysis

To identify the potential interactions between the PV system and the distribution network, to identify the nature of interaction, and to determine the robustness of the PV system controllers against variation of parameters, an eigenvalue analysis is carried out on the linearized model represented by (6.49)-(6.52). The nominal values used for the eigenvalue analysis in MATLAB environment are represented in Table 6.1.

Figure 6.2 illustrates the variation of eigenmodes corresponding to state variable i_{dc} , with insolation level varying from 0.1 to 1 kW/m^2 , with feedforward control enabled and disabled. From the plot, it can be observed that for the case where feedforward control is disabled, the eigenmodes can have a positive real part for low solar irradiation levels

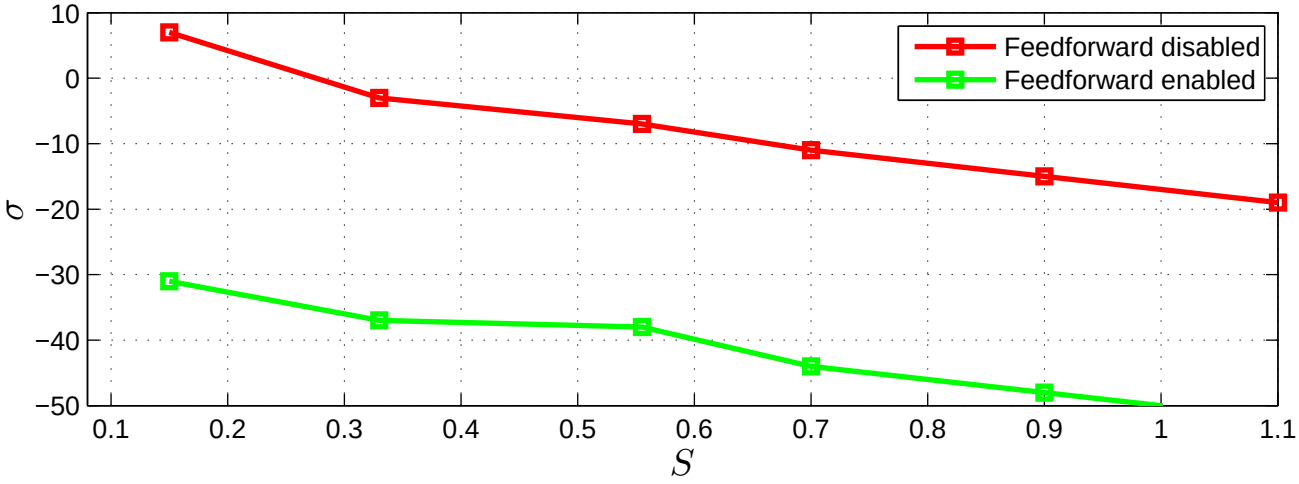

Figure 6.2 Pattern of variation of eigenmodes corresponding to i_{dc} in the presence and absence of feed-forward compensation in the DC-link current controller.

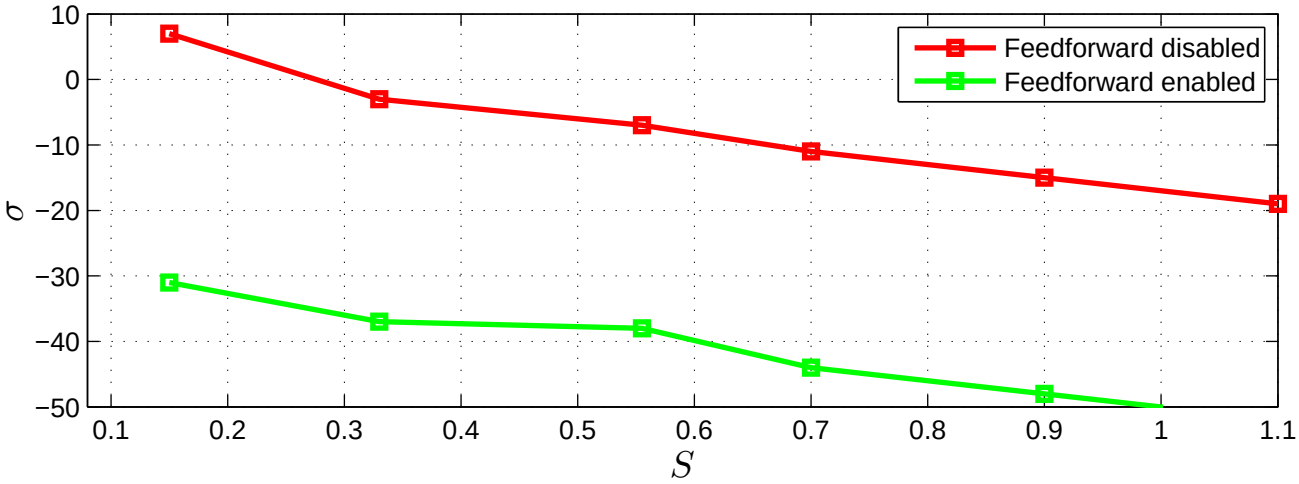

Figure 6.3 Pattern of variation of eigenmodes corresponding to i_{sd} in the presence and absence of feed-forward compensation in the DC-link current controller.

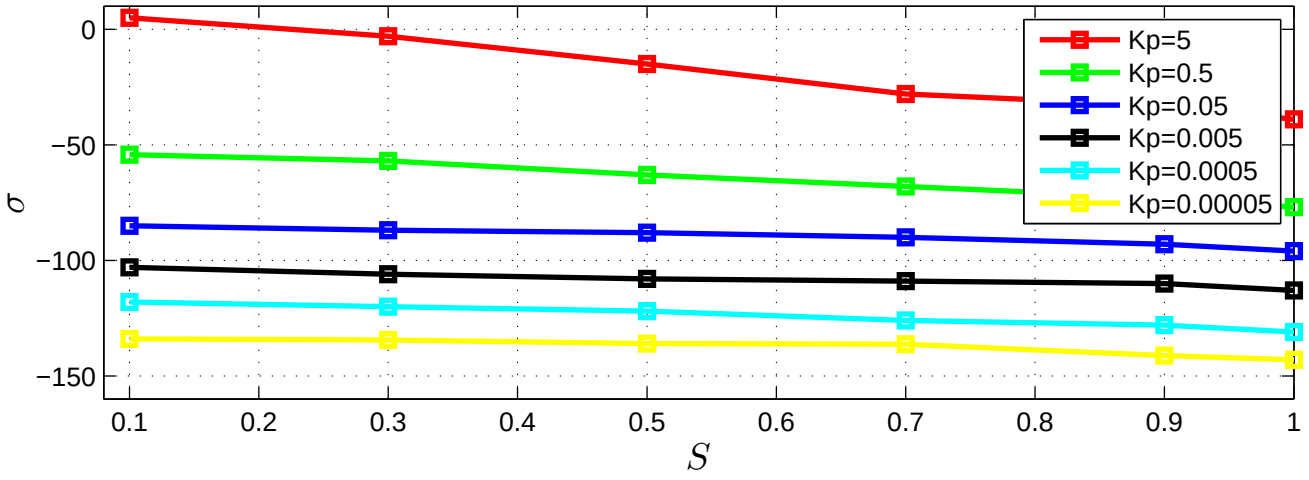

Figure 6.4 Pattern of variation of eigenmodes corresponding to i_{sd} with the variation of proportional gain of inner current controller.

resulting in instability. However, for the case where the feedforward compensation in the DC-link current control loop is enabled, eigenmodes are in the negative half of s-plane for all solar irradiation values, resulting in a stable system. For similar conditions, the eigenmodes corresponding to state variable i_{sd} are plotted in Figure 6.3. Since current i_{sd} is dependent on the current i_{dc}, a pattern similar to that for i_{dc} results.

To demonstrate the impact of inner current controller, eigenmodes of i_{sd} for different insolation levels and controller proportional gains k_p are plotted in Figure 6.4. The system behaves in stable manner when k_p is maintained at low values. However, eignemodes of the current that is injected into the grid move towards positive half of s-plane when k_p is increased at low insolation levels. Therefore, it is safe to tune the inner current control loop at a low k_p. The analytical discussion on choosing low values for k_p given in Chapter 3 is confirmed by the results presented in Figure 6.4.

The results discussed so far illustrate the impact of PV system on the current that is injected into the grid. For safe operation of the system, it is important to study the impact of grid parameter on the eigenmodes of PV system. For this study, the state variable chosen

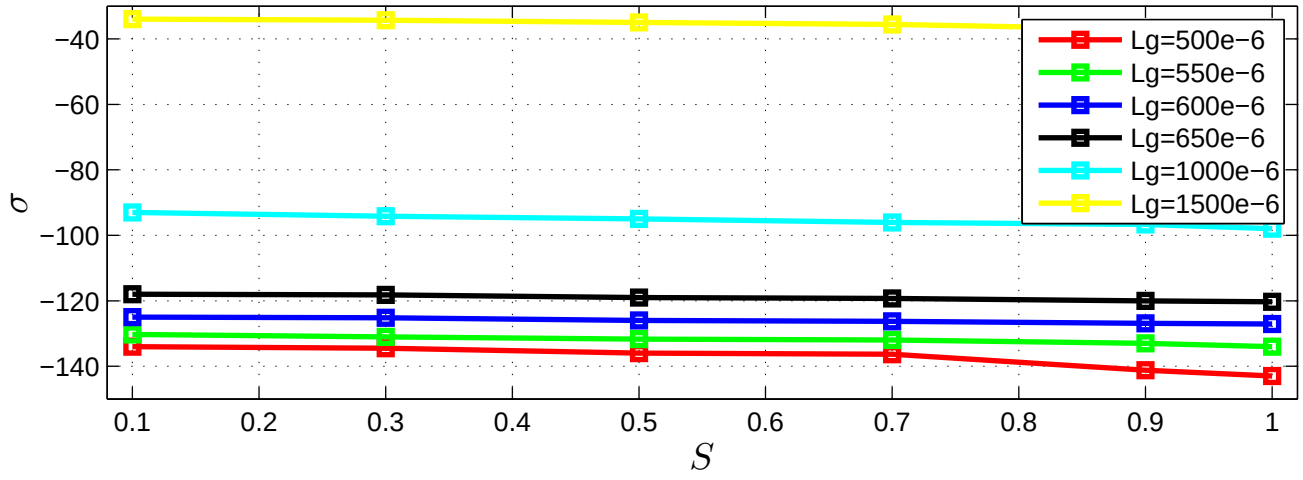

Figure 6.5 Pattern of variation of eigenmodes corresponding to i_{dc} with the variation of grid inductance.

is current i_{dc}. An increase in value of grid inductance also implies increase in distance of PV system for the grid or connecting the PV system to a weaker system. The variation of eigenmodes of i_{dc} with change in grid inductance is plotted in Figure 6.5. From Figure 6.5, it can be observed that when the grid inductance is low, implying a shorter distance between the PV system and the grid or connection to a stronger system, the eigenmodes mostly reside in the negative half of s-plane, resulting in a stable system. However, the eigenmodes approach origin at higher values of grid inductance, implying a longer distance between the PV system and the grid or connection to a weak system.

6.5 Summary

In this chapter, sensitivity of state variables to variations in different system parameters is analyzed by examining the location of corresponding eigenmodes. The parameters considered for the study are DC-side current control loop feedforward enable/disable signal, AC-side inner current control loop's proportional gain, solar irradiation level and grid in-

ductance. For eigenmode analysis, the PV system including the controllers and PV arrays, is linearized by applying a small perturbation around the steady state operating point. From the results, it is observed that the system tends to become unstable when the insolation level is low and feedforward control in DC-side current control loop is disabled. However, system stability is improved with enabling feedforward control in DC-side current controller, decrease in the proportional gain of the AC-side inner current control loop, increase in the solar insolation level and decrease in the grid inductance, i.e., connection to a stronger system. This analysis serves as a useful tool for selecting the parameters in practical implementation.

Chapter 7

Summary, Contributions, and Future Work

7.1 Summary

The main objective of this thesis is to make quality contributions in the field of power electronic interface for grid-connected PV systems. For this purpose, the less-investigated topology for PV system grid interface, i.e., Current Source Inverter was chosen. To make sure about the originality of the work and to avoid repetition of the past work, an extensive literature survey was carried out first. The literature survey covers a range of topologies employed for interfacing PVs. A part of literature survey focusses on grid-connected PV systems that incorporate CSI as their power conditioning units. The survey was a useful way to determine the research gap in the field of CSIs for PV applications. In the initial stage of research, a single-stage CSI-based PV system was designed. The design involved developing a DC-link current controller, which allowed maximum power point tracking, and an AC-side current controller with the mandates of AC-side current waveshaping and reactive power control. The maximum power point tracker (MPPT) is based on the widely-

used Perturb & Observe (P&O) method and can track the maximum power point in the order of milliseconds. To efficiently track the current reference generated by the MPPT, DC-link current controller is equipped with a feed-forward compensation technique. The feed-forward control plays a major role in suppressing the nonlinearity caused by PV arrays. A mathematical proof of this suppression is provided in Chapter 3. The AC-side current controller is designed in a stationary frame of reference. For converting the 3-phase state variables to their corresponding *dq*-frame equivalents, the transformation angle is derived from the Phase-Locked Loop (PLL). The task of the AC-side current controller is to track the reference for the d-axis component of AC-side current, generated by DC-link current controller, and inject a clean sinusoidal current into the grid that is in phase with the voltage at the PCC. The AC-side current controller has the flexibility of adjusting reactive power to a desired value. However, for this work, it is assumed that there is no reactive power demand from the PV system. Therefore, the reactive component is set to zero and there is only active power transfer between the PV system and the distribution system. To verify the performance of the developed CSI-based PV system, a number of simulation studies are carried out in PSCAD/EMTDC environment. In the first case study, the performance of the CSI-based PV system is compared with that of a VSI-based PV system of similar rating for a step change in the insolation level. Through simulation results, it is shown that even though both topologies show similar performances, the quality of the sinusoidal current generated by a CSI-based PV system is superior to that of the current generated by a VSI-based PV system. To illustrate the performance of the CSI-based PV system during transients on the grid side, simulation studies are carried out for four kinds of faults. Results obtained from fault studies are highly in favor of CSI topology and provide illustrative evidence for short-circuit current protection capability of the CSI. On the other hand, the VSI-based PV system performs poorly when subjected to similar grid transients. Comparative evaluation results are provided in Chapter 3.

To extend the research on CSI-based PV system further, a multilevel structure is dis-

cussed in Chapter 4. The multilevel structure is a parallel combination of n units of CSI and capable of producing $2n + 1$ levels of current in the output. Due to increase in the number of levels of current in the output terminals, the multilevel structure can produce clean sinusoidal current at a considerably lower switching frequency. The CSI units in the multilevel structure are equipped with their own MPPTs. However, on the AC-side, a combined current control scheme in stationary frame of reference is proposed. The multilevel structure is interfaced to grid through a single capacitive filter. Thus, the design results in a high power rating with reduced number of filters, sensors and controllers. Upon simulating the system, satisfactory performance is obtained when PV arrays of individual units are exposed to equal insolation levels. However, when the units are exposed to different insolation levels, low-order harmonics are generated in the current that is injected into the grid. These low-order harmonics deteriorate the performance by increasing the Total Harmonic Distortion (THD) of the current. The current with low-order harmonics injected into the distribution line can have adverse impact on the loads connected to the distribution line. The next challenge is to address the concern raised due to introduction of these harmonics. Minimization of these harmonics can be performed by adopting different strategies: (1) new modulation techniques, (2) modifying filter design, (3) implementing new control strategy. The challenge is to come up with a technique that can serve the following purposes: (1) be very fast and involve minimum computation efforts, unlike Selective Harmonic Elimination technique, (2) be able to perform harmonic elimination online, in real time, (3) have no adverse impact on operation of other control logics. After a thorough study of different techniques, a technique was introduced to eliminate harmonics efficiently for the multilevel structure composed of units fed from PV panels under unequal insolation conditions. Suppression of these harmonics is performed by implementing a modified current control strategy in stationary frame that deals with individual harmonics separately and reduces the selected harmonics to the desired levels. For minimizing the harmonics, the harmonic components are converted to their corresponding dq-equivalents and are compared with

their corresponding reference values set by the user. The angle of each transformation corresponds to the specific harmonic that needs to be suppressed. The modified control strategy operates in coordination with the existing DC-side and AC-side current controllers and MPPTs. Therefore, suppression of harmonics can be implemented online, in real time. The promising results obtained are discussed towards the end of Chapter 4. Evaluation of performance of the multilevel structure developed in Chapter 4 during grid transient is performed in Chapter 5.

In Chapter 5, the islanding behavior of the multilevel structure is investigated when individual units are operating under equal and unequal power level conditions. Through mathematical analysis, it is shown that, when units of the multilevel structure are operating under different insolation levels, the extent of change in voltage at the PCC as a result of islanding is different from that in the case when units are operating under equal insolation levels. These results are derived mathematically for an islanding detection scheme equipped with OVP/UVP and OFP/UFP. This analysis provides insight into the effect of location of PV arrays in a PV field on the islanding protection. If majority of PV arrays are under low insolation level conditions, islanding detection logic may not be triggered. The results reported in this chapter coveys an important message that shading of PV arrays not only impacts the maximum power available from the PV arrays in a multilevel structure, but also the protection of the system against islanding.

To go beyond performance analysis of CSI-based PV system based on simulation and have a more in-depth knowledge of the system behavior, it is important to study the response of dominant state variables to variations of different system parameters. To have an idea of sensitivity of dominant state variables to different parameters, numerous techniques have been introduced in the literatures. In this work, eigenvalue analysis is used for this purpose. To determine eigenvalues, a small-signal model for the complete system is derived by assuming a small perturbation around the steady-state operating

point. The small-signal model represents dynamics of PV arrays, DC-side of the inverter, AC-side of the inverter, and distribution system. For this study, the sensitivity of the eigenmode corresponding to the sinusoidal current injected into the grid is studied with respect to variations of current controller parameter, insolation level, and grid-inductance. The study also covers movement of eigenmodes in the presence and absence of feed-forward compensation at different insolation level. Results from eigenvalue analysis confirm that the eigenmode under investigation tends to move to positive half of s-plane in the absence of feed-forward compensation when the PV system is operating at low insolation level. Furthermore, the study suggests that for best performance, the PV system should be located close to the grid or see a strong system at the point of connection to the grid. Installing the PV system far away from the grid or connecting the PV system to a weak system, may result in instability. The study also includes impact of proportional gain constant of the outer control loop on the location of eigenvalue corresponding to the current injected into the grid at different insolation levels.

7.2 Contributions of the Research

- The research presented a comprehensive overview of different topologies used for grid-connected PV systems. Even though Voltage-Source Inverter has proved to be a capable topology for this purpose, concerns about quality of power on the AC-side, overcurrent protection during AC-side faults, and filtering requirements are yet to be resolved. This work proved that Current Source Inverter topology was capable of addressing those concerns and paved the way for practical implementation of CSIs in the field for PV system applications.

- The research has made a major contribution in the design of control structure for three-phase grid-connected PV system based on CSI. The feed-forward compensation

introduced in the outer DC-link current control loop can eliminate the nonlinearity introduced by the PV array. Moreover, this thesis introduced a new way of tuning control parameters for controlling the current that is injected into the grid. Operation of these control structure in combination with the Maximum Power Point Tracker was tested through simulation for different insolation levels.

- Based on the control algorithms developed for CSI-based PV system, a multilevel structure is introduced to the world of multilevel topologies based on CSI. The multilevel structure has the flexibility of accommodating PV units operating under equal and unequal insolation levels with reduced control structure and number of sensors and filter components. The controller design and analysis for multilevel CSI presented in this work has never been addressed before. Operation of multilevel CSI with different DC inputs and incorporating measures in the control structure to eliminate selected harmonics is a major contribution to the field. The multilevel structure for PV application introduced in this thesis can be adopted for large PV farms.

- The thesis has made contribution in the field of islanding behavior of multilevel topologies. A relationship between the extents of change in the voltage level at the PCC due to islanding and power level of each unit is developed. The relationship suggests that when individual units of multilevel topology are operating at different power levels, islanding can be detected faster than when all the units are operating at equal power level. This analysis shows that from the viewpoint of islanding protection speed, spreading the PV modules connected to a multilevel CSI structure in a PV field is more beneficial than installing them very close to one another. This is due to the fact that in this way, it is more probable for the panels to receive unequal solar irradiation levels. This can be more effective for building-integrated PV systems, where PV panels are receiving uneven irradiation levels due their diverse locations that leads to varying partial shading conditions in the course of a day.

- A small-signal model was developed for the CSI-based PV system in this thesis by assuming a small perturbation around the steady-state operating point and linearizing the nonlinear equations. The analysis and results presented in this thesis are helpful for practical implementation purpose. The sensitivity analysis results can be taken advantage of in selecting the proper location of PV systems within a power system, choosing appropriate values for control parameters and positioning of PV arrays in a PV farm.

7.3 Future Direction

The research carried out in the course of PhD study gives a new direction in modeling and design of CSI-based PV systems. Operational characteristics are discussed for single-module and multilevel CSI-based PV systems. The following topics have not been covered and can serve as ideas for future work.

- Investigation of common-mode voltage for multilevel topology. Impact of common-mode voltage on the operation of PV modules connected to the DC-side of the multilevel topology. This concern has been well addressed for VSI-based topologies.
- A more detailed analysis and examination of PV system under fault conditions. The results would be of interest to distribution system planners and utility companies.
- Investigation of other methods and comparison of different methods for elimination of harmonics in multilevel CSI topology operating under unequal power levels on the DC-side.
- Developing efficient anti-islanding algorithms for the multilevel topology to complement the existing anti-islanding measures that mainly focus on single-unit inverter systems.

- Considering different kinds of load in small-signal studies and investigating the impact of nonlinear loads on the performance of the PV system.
- Building a lab prototype of the multilevel CSI-based PV system for experimental studies and validating the analytical models developed and verifying the simulation results obtained.

Bibliography

[1] R. Singh, G. F. Alapatt, and K. F. Poole, "Photovoltaics: Emerging role as a dominant electricity generation technology in the 21^{st} century," in *International Conference on Microelectronics*, 2012, pp. 53–63. 6

[2] "Trends in Photovoltaic application, survey report of selected IEA countries between 1992 and 2002," *International Energy Agency Photovoltaic Power system, IEA, PVPS T1-12:2003*, 2003, www.iea-pvps.org. 8

[3] E. Koutroulis and F. Blaabjerg, "Methods for the optimal design of grid-connected PV inverters," *International Journal of Renewable Energy Research*, vol. 1, no. 2, pp. 54–64, 2011. 8

[4] H. Kim and K. Kim, "Filter design for grid-connected PV inverters," in *International conference on Sustaianble Energy Technologies*, 2008, pp. 1070–1075. 9

[5] "Limits for harmonic current emissions (equipment input current less than 16 A per phase)-first edition," *Electromagnetic Compatibility (EMC)*, 1995. 9

[6] "National electric code," *National Fire Protection Association Inc.*, 2002. 9

[7] B. Verhoeven, "Utility aspects for grid connected Photovoltaic power system," *International Energy Agnecy, Photovoltaic Power System, IEA, PVPS T5-01:1998*, 1998. 9, 10

[8] S. Kjaer, J. K. Pedersen, and Blaabjerg, "A review of single-phase grid-connected inverters for Photovoltaic modules," *IEEE Transaction on Industry Application*, vol. 41, no. 5, pp. 1292–1306, 2005. 9, 10, 13, 15

[9] O. Willumsen, "Connection of solar systems," 2003, Danish Electricity Supply-Research and Development (DEFU), Copenhagen, Denmark, Tech. Rep. 501. 9

[10] S. J. Huang and F. S. Pai, "A new approach to islanding detection of disperesed generators with self-commutated static power converters," *IEEE Transaction on Power Delivery*, vol. 15, no. 2, pp. 668–773, 2000. 9

[11] M. E. Ropp, M. Begovic, Rohatgi, G. A. Kern, R. H. Bonn, and S. Gonzalez, "Determine the relative effectiveness of islanding detection methods using phase criteria and non detection zones," *IEEE Transaction on Energy Conversion*, vol. 15, no. 3, pp. 290–296, 2000. 9

[12] P. O'Kane and B. Fox, "Loss of mains detection for embeded generation by system impedance monitoring," in *International conference on development in power system protection*, 1997, pp. 95–98. 9

[13] P. D. Hopewell and N. Jenkins, "Loss of mains detection for small generations," in *IEEE Proceedings for Electric Power Application*, vol. 143, no. 3, 1996, pp. 225–230. 9

[14] M. Liserre, A. Pigazo, A. Dell'Aquil, and V. M. Moreno, "An anti-islanding method for single-stage inverters based on a grid voltage sensorless control," *IEEE Transaction on Industrial Electronics*, vol. 53, no. 5, pp. 1418–1426, 2006. 9

[15] H. Zeineldine, "A Q-f droop curve for facilitating islanding detection of inverter-based distributed generation," *IEEE Transaction on Power Delivery*, vol. 24, no. 3, pp. 665–673, 2009. 9

[16] M. Ropp and W. Bower, "Evaluation of islanding detection methods for photovoltaic utility interactive power," 2002, international Energy Agency Implementing Agreement on Photovoltaic Power Systems, Tech. Rep. IEA PVPS T5-09. 9

[17] T. Esram and P. L. Chapman, "Comparison of Phorovoltaic array maximum power point tracking techniques," *IEEE Transaction on Energy Conversion*, vol. 22, no. 2, pp. 439–450, 2007. 10

[18] G. Meinhardt and G. Cramer, "Past, present, and future of grid-connected PV and hybrid power system," in *Proceedings IEEE-PES meeting*, vol. 2, 2000, pp. 1283–1288. 12

[19] H. Patel and V. Agarwal, "A single-stage, single-phase, transformer-less doubly grounded grid-connected pv interface," *IEEE Transaction on Energy Conversion*, vol. 24, no. 1, pp. 93–101, 2009. 14, 15

[20] S. B. Kjaer, J. K. Pederson, and F. Blaabjerg, "Power inverter topologies for PV modules-a review," in *Proceedings IEEE-IAS Annual meeting*, vol. 2, 2002, pp. 782–788. 15

[21] W. Hongbin and T. Xiaofeng, "Three-phase photovoltaic grid-connected generation technology with MPPT function and voltage control," in *International Conference on Power Electrronics and Drive System*, 2009, pp. 1295–1300. 15

[22] Z. Xue-Song, L. Fang, M. You-Jie, and S. Dai-Chun, "Research of control technology in grid-connected photovoltaic power system," in *International conference on Computer, Mechatronics, control and Electronic Engineering*, 2011, pp. 2340–2345. 15

[23] N. Hingorani and L. Gyugyi, *Understanding FACTS: concept and technology of Flexible AC transmission system.* Wiley-IEEE, 1999. 15

[24] F. Z. Peng, "Z-source inverter," *IEEE Transaction on Industry Application*, vol. 39, no. 2, pp. 504–510, 2003. 17

[25] Y. Huang, M. Shen, and F. Peng, "Z-source inverter for residential photovoltaic system," *IEEE Transaction on Power Electronics*, vol. 21, no. 6, pp. 1776–1782, 2006. 17

[26] R. Badin, Y. Huang, F. Peng, and H. Kim, "Grid interconnected Z-source PV system," in *Power Electronic Specialist Conference*, 2007, pp. 2328–2333. 17

[27] B. Farhangi and S. Farhangi, "Comparison of Z-source inverter and buck-boost inverter topologies as a single-phase transformer-less photovoltaic grid-connectd power conditioner," in *Power Electronic Specialist Conference*, 2006, pp. 1–6. 17

[28] P. J. Grbovi, F. Gruson, and F. Idir, "Turn-on performance of Reverse Blocking IGBT(RB-IGBT) and optimization using advanced gate driver," *IEEE Transaction on Power Electronics*, vol. 25, no. 4, pp. 970–980, 2010. 18

[29] E. R. Motto, J. F. Donlon, M. Tabata, H. Takahashi, Y. Yu, and G. Majumdar, "Application characteristics of an experimental RB-IGBT (Revesre-Blocking IGBT) module," in *IAS Annual meeting*, vol. 3, 2004, pp. 1540–1544. 18

[30] B. Sahan, S. V. Araujo, C. Noding, and P. Zacharias, "Comparative evaluation of three-phase current source inverters for grid interfacing of distributed and renewable energy systems," *IEEE Transaction on Power Electronics*, vol. 26, no. 8, pp. 2304–2318, 2011. 18

[31] D. Z. Zmood and D. G. Holmes, "Improved voltage regulation for current-source inverter," *IEEE Transaction on Industry Application*, vol. 37, no. 4, pp. 1028–1036, 2001. 18

[32] M. Kazerani and Y. Ye, "Comparative evaluation of three-phase PWM voltage- and current-source converetr topology in FACTS application," in *PES general meeting*, 2002, pp. 473–479. 19

[33] M. H. Bierhoff and F. Fuchs, "Semiconductor losses in voltage source and current source IGBT converter based on analytical derivation," in *PES Conference*, vol. 4. 19

[34] M. Mohr and F. Fuchs, "Comparison of three-phase current source inverters and voltage source inverters linked with dc-dc boost converters for fuel cell generation systems," in *European Conference on power elctronic and application*, 2005, pp. 10 pp. –P.10. 19

[35] B. Sahan and P. Z. N. Vergara, A. Engler, "A single-stage PV module integrated converter based on a low-power current source inverter," *IEEE Transaction on Industry Application*, vol. 55, no. 7, pp. 2602–2609, 2008. 19

[36] C. Klumpner, "A new single-stage current source inverter for PV and fuel cell application using RB-IGBTs," in *Power Electronic Specialist Conference*, 2007, pp. 1683–1689. 20, 21

[37] C. Photong, C. Klumpner, and P. Wheeler, "A current source inverter with series connected AC capacitors for photovoltaic application with grid fault ride through capability," in *Industrial Electronics Conference*, 2007, pp. 907–912. 21

[38] O. Lopez, R. Teodorescu, F. Freijedo, and J. DovalGandoy, "Leakage current evaluation of a singlephase treansformerless PV inverter connected to the grid," in *Applied Power Electronic Conference*, 2007, pp. 907–912. 22

[39] K. Hirachi and Y. Tomokuni, "Improved control strategy to elminate the harmonic current components for single-phase PWM current source inverter," in *International Telecommunication Energy Conference*, 1997, pp. 189–194. 22

[40] J. S. S. Prasad and B. G. Fernandes, "Active commutated thyristor csi for grid-connected PV application," in *International Power Electronics and Motion Control Conference*, vol. 3, 2004, pp. 1767–1771. 22

[41] Y. Sato and T. Kataoka, "A current-type PWM rectifier with active damping function," *IEEE Transaction on Industry Application*, vol. 32, no. 3, pp. 533–541, 1996. 22

[42] Y. Neba, "A simple method for suppression of resonance oscillation in PWM current source converter," *IEEE Transaction on Power Electronics*, vol. 20, no. 1, pp. 132–139, 2005. 22

[43] G. Ertasgin, D. M. Whaley, and N. Ertugrul, "Implementation and performance evaluation of a low-cost current-source grid-connected inverter for PV application," in *International Conference on Sustainable Energy Technologies*, 2008, pp. 939–944. 22, 23

[44] J. Lai and F. Peng, "Multilevel converters-a new brand of power converters," *IEEE Transaction on Industry Application*, vol. 32, no. 3, pp. 509–517, 1996. 24

[45] Z. Bai, Z. Zhang, and Y. Zhang, "A generalized three-phase multilevel current source inverter with carrier-phase-shifted spwm," in *Power Electronic Specialist Conference*, 2007, pp. 2055–2060. 24

[46] Y. Xu, L. Xin, and Z. Zhang, "A new three-phase five level current source inverter," in *Applied Power Electronic Conference*, 2005, pp. 424–427. 24

[47] Z. Zhang and B. T. Ooi, "Multi-modular current source spwm converters for superconducting magnetic energy storage system," *IEEE Transaction on Power Electronics*, vol. 8, no. 3, pp. 250–256, 1993. 24

[48] P. E. Melin, J. R. Espinoza, N. R. Zargari, L. A. Moran, and J. I. Guzman, "A novel multilevel converter based on current source power cell," in *Power Electronic Specialist Conference*, 2008, pp. 2084–2089. 24

[49] N. Vazquez, H. Lopez, C. Hernandez, E. Vazquez, and R. Osorio, "A different multilevel current source inverter," *IEEE Transaction on Industrial Electronics*, vol. 1, no. 99, pp. 1–10, 2009. 24

[50] S. H. Hosseini and M. Kangarlu, "A new topology for multilevel current source inverter with reduced number of switches," in *Electrical and Electronics Engineering Conference*, 2009, pp. 273–277. 24

[51] M. C. Chandorkar, D. M. Divan, and R. H. Lasseter, "Control techniques for multiple current source GTO converters," *IEEE Transaction on Industry Application*, vol. 31, no. 1, pp. 134–140, 1995. 25

[52] S. Daher, R. The, and F. Antunes, "Multilevel current source inverter-the switching and control strategy for high power application," in *Industrial Electronics Conference*, 1996, pp. 1752–1757. 25

[53] J. Espinoza, L. Moran, and N. Zargari, "Multilevel three-phase current source inverter based voltage compensator," in *Power Electronic Specialist Conference*, 2005, pp. 2264–2269. 25

[54] Y. Xiangwu, Z. Bo, G. Xiaobin, Z. Lixia, and L. Heming, "Double closed loop control of three-phase five-level pwm current source inverter," in *Industrial Electronics Conference*, 2007, pp. 2110–2114. 25

[55] N. Femia, G. Petrone, and G. Spagnuolo, "Optimization of perturb and observe maximum power point tracking method," *IEEE Transaction on Power Electronics*, vol. 20, no. 4, pp. 963–973, 2005. 28

[56] Y. Ye, *Advances in modeling and application of three-phase power converters.* PhD thesis, Unievrsity of Waterloo, 2001. 28

[57] N. Mohan, T. Undeland, and W. P. Robbins, *Power Electronics: Converters, Applications, and Design.* John Wiley & sons, Inc, 2002. 28

[58] K. H. Hussein, I. Muta, T. Hoshino, and M. Osakada, "Maximum photovoltaic power tracking: an algorithm for rapidly changing atmospheric conditions," 1996, pp. 1752–1757. 30

[59] K. N. Hasan, M. E. Haque, M. Negnevitsky, and K. M. Muttaqi, "An improved maximum power point tracking technique of the photovoltaic module with current mode control," in *Applied Power Electronic Conference*, 2009, pp. 1–6. 31

[60] Y. Xiong, Y. Zhang, K. Wei, and Z. Zhang, "Carrier phase-shifted SPWM based current source multi-converter," in *Applied Power Electronic Conference*, 2003, pp. 89–93. 32

[61] A. Yazdani and R. Iravani, *Voltage-Sourced Converters in Power Systems.* John Wiley & Sons, Inc, 2010. 33

[62] S. K. Chung, "A phase tracking system for three phase utility interface inverters," *IEEE Transaction on Power Electronics*, vol. 15, no. 3, pp. 431–438, 2000. 36, 37

[63] A. Yazdani and P. P. Dash, "A control methodology and characterization of dynamics for a photovoltaic (PV) system interfaced with a distribution network," *IEEE Transaction on Power Delivery*, vol. 24, no. 3, pp. 1538–1551, 2009. 42

[64] X. Pei and Y. Kang, "Short-circuit fault protection strategy for high-power three-phase three-wire inverter," *IEEE Transaction on Industrial Informatics*, vol. 8, no. 3, pp. 545–553, 2012. 43

[65] P. Dash and M. Kazerani, "Dynamic modeling and performance analysis of a grid-connected current source inverter-based photovoltaic system," *IEEE Transaction on Sustainable Energy*, vol. 2, no. 4, pp. 443–450, 2011. 43

[66] "PSCAD/EMTDC," v. 4.2, Manitoba HVDC Research Centre, Winnipeg, Manitoba, Canada. 58

[67] "IEEE standard 519-1992," *IEEE Recommended Practices and Requirements for harmonics control in Electrical Power Systems*. 63

[68] M. S. Dahidah and V. G. Agelidis, "Selective harmonic elimination for multiconverter control with variant dc sources," in *Industrial Electronics Application*, 2009, pp. 3351–3356. 64

[69] L. M. Tolbert, J. N. Chiasson, Z. Du, and K. J. Mckenzie, "Elimination of harmonics in a multilevel converter with nonequal dc sources," *IEEE Transaction on Industry Application*, vol. 4, no. 1, pp. 75–82, 2005. 64

[70] J. N. Chiasson, L. M. Tolbert, K. J. Mckenzie, and Z. Du, "Control of a multilevel converter using resultant theory," *IEEE transaction on Control Systems Technology*, vol. 11, no. 3, pp. 345–354, 2000. 64

[71] Z. Du, L. M. Tolbert, and J. N. Chiasson, "Harmonic eliminationin multilevel converter with programmed PWM method," in *IEEE Industrial Application Society Annual Meeting*, 2004, pp. 2210–2215. 64

[72] B. Ozpineci, L. M. Tolbert, and J. N. Chiasson, "Harmonic elimination in multilevel converter using genetic algorithm," in *IEEE Industrial Application Society Annual Meeting*, 2005, pp. 92–95. 64

[73] Z. Du, L. M. Tolbert, and J. N. Chiasson, "Active harmonic elimination for multilevel converters," *IEEE Transaction on Power Electronics*, vol. 21, no. 2, pp. 459–469, 2006. 64

[74] V. G. Agelidis, V. Balouktsis, and A. Balouktsis, "On applying a minimization technique to the harmonic elimination PWM control," *IEEE Power Electronics Letters*, vol. 2, no. 2, pp. 41–44, 2004. 64

[75] J. Ning and Y. He, "Phase-shifted suboptimal pulse-width modulation strategy for multilevel inverter," in *IIEEE conference on Industrial Electronics and Applicaiton*, 2006, pp. 1–5. 64, 65

[76] F. Filho, L. M. Tolbert, Y. Cao, and B. Ozpineci, "Real-time selective harmonic minimization for multilevel inverters connected to solar panels using artificial neural network angle generation," *IEEE Transaction on Industry Application*, vol. 47, no. 5, pp. 2117–2124, 2011. 64, 65

[77] J. R. Wells, "Modulation-based harmonic elimination," *IEEE Transaction on Power Electronics*, vol. 22, no. 1, pp. 336–340, 2007. 65

[78] L. Yi, S. Heming, and Z. Ling, "Harmonic analysis and filter design for medium voltage multilevel PWM inverters," in *international Conference on Power Electronics and Drive System*, 2003, pp. 531–5355. 65

[79] H. Willis and W. Scott, *Distributed power generation: planning and evaluation.* Marcel Dekker, New York, 2000. 70

[80] G. Masters, *Renewable and efficient electric power system.* Wiley Interscience, 2005. 70

[81] F. Z. Peng, "Special issue on distributed power generation," *IEEE Transaction on Power Electronics*, vol. 19, no. 5, 2004. 70

[82] J. R. Enslin and P. M. Heskes, "Harmonic interaction between a large number of distributes power inverters and the distribution network," *IEEE Transaction on Power Electronics*, vol. 19, no. 6, pp. 1586–1593, 2004. 70

[83] "IEEE recommended practice for utility interface of photovoltaic (PV) systems," *IEEE Std.*, pp. 929–2000, 2000. 70

[84] "IEEE standard for interconnecting distributed resources with electric power systems," *IEEE Std.*, 2003. 70

[85] "Draft p1589," *IEEE standard for conformance test procedures for equipment interconnecting distributed resources with electric power systems.* 70

[86] "International energy agency implementing agreement on photovoltaic power systems, tech. rep. iea pvps t5-09," *Application guide for IEEE Std. 1547 standard for interconnecting distributed resources with elecric power systems*, 2002. 70

[87] S. J. Huang and F. Pai, "A new approach to islanding detection of disperesed generators with self-commutated static power converters," *IEEE Transaction on Power Electronics*, vol. 15, no. 2, pp. 500–507, 2000. 70

[88] M. E. Ropp, M. Begovic, A.Rohatgi, G. A. Kern, R. H. Bonn, and S. Gonzalez, "Determine the relative effectiveness of islanding detection methos using phase criteria and non detection zones," *IEEE Transaction on Energy Conversion*, vol. 15, no. 3, pp. 290–296, 2000. 70

[89] P. O'Kane and B.Fox, "Loss of mains dtetection for embeded generation by system impedance monitoring," in *International Conference on Development in Power System Protection*, 1997, pp. 95–98. 70

[90] P. D. Hopewell and N. Jenkins, "Loss of mains dtetection for embeded generation by system impedance monitoring," in *IEEE Proc.-Electr. Power Appl*, 1996, pp. 225–230. 70

[91] M. Liserre, A. Pigazo, A. Dell'Aquila, and V. M. Moreno, "An anti-islanding method for single-phase inverters based on a grid voltage sensorless control," *IEEE Transaction on Industrial Electronics*, vol. 53, no. 5, pp. 1418–1426, 2006. 70

[92] H. Zeineldin, "A q-f droop curve for facilitating islanding detection of inverter-based distributed generation," *IEEE Transaction on Power Delivery*, vol. 24, no. 3, pp. 665–673, 2009. 70

[93] L. Lopes and H. Sun, "Performance assessment of active frequency drifting islanding detection methods," *IEEE Transaction on Energy Conversion*, vol. 21, no. 1, pp. 171–180, 2006. 70

[94] H. Zeineldin and J. K. Jr., "Performance of the OVP/UVP and OFP/UFP methods with voltage and frequency dependent loads," *IEEE Transaction on Power Delivery*, vol. 24, no. 2, pp. 772–778, 2009. 70

[95] Z. Ye, A. Kolwalker, Y. Zhang, P. Du, and R. Walling, "Evaluation of anti-islanding scheme based on non detetction zone concept," *IEEE Transaction on Power Electronics*, vol. 19, no. 5, pp. 1171–1176, 2004. 70

[96] H. Zeineldin, E. F. El-Saadany, and M. M. A. Salama, "Impact of DG interface control on islanding detection and nondetection zones," *IEEE Transaction on Power Delivery*, vol. 21, no. 3, pp. 1515–1523, 2006. 71

[97] R. Bhandari, S. Gonzalez, and M. E. Ropp, "Investigation of two anti-islanding methods in the multi-inverter case," in *Power and Energy Society General Meeting*, 2008, pp. 1–5. 71

[98] D. Schutz and M. Ropp, "Simulation and experimental study of multi-inverter islanding," in *Power and Energy Society General Meeting*, 2011, pp. 1–6. 72

[99] S. Gonzalez, M. Ropp, A. Fresquez, M. Montoya, and N. Opell, "Multi-PV inverter utility interconnection evaluations," in *IEEE Photovoltaic Specialist Conference*, 2011, pp. 1–6. 72

[100] E.Figueres, G. Garcera, J. Sandia, F. Gonzalez-Espin, and J. C. Rubio, "Sensitivity study of the dynamics of three-phase photovoltaic inverter with an LCL grid filter," *IEEE Transaction on Industrial Electronics*, vol. 56, no. 3, pp. 706–717, 2009. 79

[101] H. K. Khalil, *Nonlinear Systems.* Prenitce Hall, 2002. 91

Appendix A

System Parameters for CSI-based PV System

The parameters for the CSI-based PV system developed in Chapter 3 are presented in following tables.

Table A.1: System Parameters I

PV System Parameter	Value	Comments
Grid inductance, L_g	1 mH	
Grid Resistance, R_g	1 $m\Omega$	
Grid voltage, v_g	6.6 kV	
T_r nominal power	1.3 MVA	
T_r voltage ratio	6.6/0.48 kV	Delta/Y
T_r leakage inductance	0.1 pu	
T_r ohmic resistance	0.02 pu	
on-state resistance of valves, R	3 $m\Omega$	

Table A.2: System Parameters II

filter capacitance, C_f	300 μF	
switching frequency	3060 Hz	51× 60 Hz
DC-link capacitance, C	1000 μF	
DC-link inductance, L_{dc}	1 mH	
# of PV cells per string, n_s	800	
# of PV strings, n_p	200	
ideality factor, A	1.92	
cell reference temperature, T_{ref}	300 K	
temperature coefficient, k_ϑ	0.0017 A/K	
cell short circuit current, I_{scr}	8.03 A	
reverse saturation current, I_{rs}	1.2×10^{-7} A	

Table A.3: Controller Parameters

k_p (for $\tau_i = 0.5$ ms)	0.0002	
k_i (for $\tau_i = 0.5$ ms)	2 s^{-1}	

Appendix B

VSI-based PV System

A single-line schematic diagram employed for comparative study with CSI-based PV system in Chapter 3 is provided below.

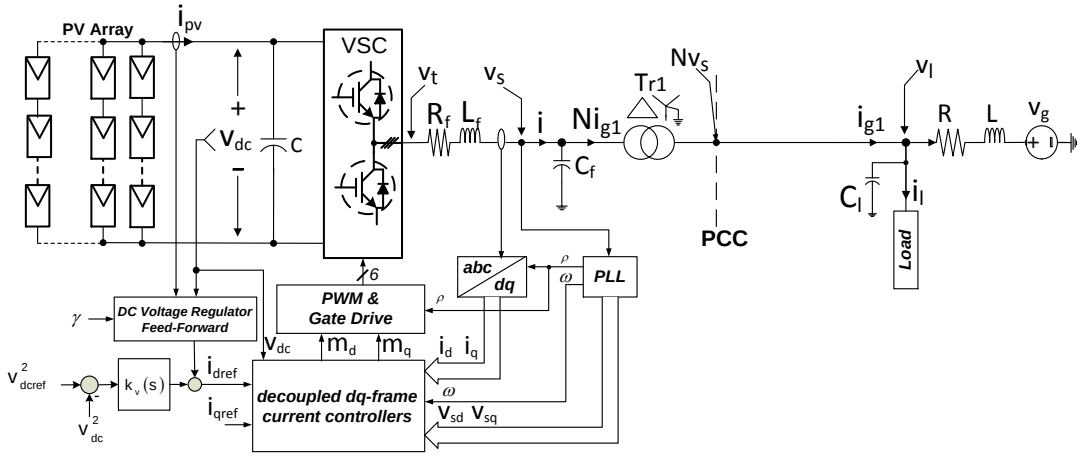

Figure B.1 Single-line schematic diagram of a three-phase, single-stage, grid-connected PV system based on VSI [61].

Appendix C

Dynamics of Multilevel Inverter based on CSI

C.1 AC-side dynamics

Each CSI of Figure 4.1 is a 6-pulse converter employing IGBT switches, operated under Sinusoidal Pulse Width Modulation (SPWM) strategy. The output current of each CSI, $\vec{i}_{tn}$, is related to the corresponding DC-side current i_{dcn} as follows:

$$\vec{i}_{tn} = \vec{m} i_{dcn} \tag{C.1}$$

where $\vec{i}_{tn}$ and $\vec{m}$ are the space phasors corresponding to the CSI terminal currents and the PWM modulating signals. Similarly, the DC-side voltage, v_{dc}, is related to the CSI AC-side voltage space phasor as

$$v_{dcn} = \vec{m} v_s \tag{C.2}$$

Assuming the switching losses of the inverter to be negligible, the DC-side powers of the inverter, P_{dc}, is equal to the power delivered on the AC-side. By power balance principle, one can write:

$$\sum_{m=1}^{n} P_{dcm} \approx P_s = \frac{3}{2}\mathrm{Re}\left\{\vec{v}_s \vec{i}_s^*\right\} \tag{C.3}$$

C.2 DC-side Dynamics

$$L_{dcn}\frac{di_{dcn}}{dt} = v_{pvn} - v_{dcn} \tag{C.4}$$

Multiplying both sides of equation (C.4) by the current i_{dcn} results in the following power relation:

$$L_{dcn} i_{dcn}\frac{di_{dcn}}{dt} = v_{pvn} i_{dcn} - v_{dcn} i_{dcn} \tag{C.5}$$

The two terms on the right hand side of (C.5) represent the power delivered by the n^{th} PV array, P_{pvn}, and the power received by the DC-side of the n^{th} inverter, P_{dcn}, respectively. Thus, one can obtain the power balance equation as:

$$\frac{1}{2}L_{dc}\frac{di_{dcn}^2}{dt} = P_{pvn} - P_{dcn}\left(\approx P_s\right). \tag{C.6}$$

Writing (C.6) for n modules, adding both sides of the resulting equations, assuming DC-side inductances of all modules to be identical and substituting the expression of P_s from (C.5), one gets

$$\frac{1}{2}L_{dc}\sum_{m=1}^{n}\frac{di_{dcm}^2}{dt} = \sum_{m=1}^{n} P_{pvm} - \frac{3}{2}\left(v_{sd} i_{sd} + v_{sq} i_{sq}\right) \tag{C.7}$$